# SEAFLOOR MASSIVE SULFIDE DEPOSITS FROM THE JUAN DE FUCA RIDGE: EVIDENCE FROM MULTIPLE SULFUR ISOTOPES FOR BURIED SEDIMENT AND MICROBIAL ACTIVITY

by © Sarah Moriarty

A Thesis submitted to the School of Graduate Studies in partial fulfillment of the requirements for the degree of

**Master of Science**

**Department of Earth Sciences**

Memorial University of Newfoundland

**October 2020**

St. John's, Newfoundland and Labrador

## Abstract

Submarine hydrothermal vent systems hosted at sedimented mid-ocean ridges are often associated with larger seafloor massive sulfide deposits than typical sediment-free mid-ocean ridge systems. The Juan de Fuca spreading ridge contains both sediment-hosted and sediment-free hydrothermal systems (Middle Valley and Axial Volcano, respectively). The ridge also contains the Endeavour vent field, which occurs at the outer extent of turbiditic sediments, where the seafloor is currently sediment-free and consists of basaltic lava flows, but evidence from hydrothermal vent fluid composition suggests the presence of buried sediment. Multiple sulfur isotope ratios of hydrothermal precipitates from these three sites were analyzed to isotopically fingerprint differences in hydrothermal sulfur cycling associated with sedimented and sediment-free substrates. A three-component mixing model in $\Delta^{33}S$ and $\delta^{34}S$ space was developed that represents the differing contributions of sulfur derived from seawater, magmatic sources, and both sediment and crustal sulfur sources that have been influenced by microbial activity.

## Acknowledgements

This project would not have been possible without the invaluable assistance and suggestions provided by my supervisor, Dr. John Jamieson, and supervisory committee member Dr. Michael Babechuk. I am also grateful for the lab assistance and research-related insights provided by Dr. James Farquhar, Dr. M. K. Tivey, Dr. Alison Leitch, Dr. Dan Rogers, Dr. Jill McDermott, Dr. David Johnston, Sara Jenkins, Dr. Jason Sylvan, and other members of the Jamieson Marine Mineral Resources lab at MUN. I am extremely thankful for the clear, helpful, and informative lab training I received from Dr. Emma Bertran. Thank you to Dr. Jason Sylvan for the opportunity to dive in Alvin on two separate occasions, and to the Alvin operations team for facilitating those dives. I would like to extend a special thank you to Dr. Harald Strauss and Christian Peters for going out of their way to perform replicate analyses on several of the samples, despite having no other prior connection to the project. I also appreciate their patience while they waited for me to share my interpretations with them. Lastly, I would like to acknowledge the scientists and crew members aboard the AT15-36 Atlantis 2008, AT15-47 Atlantis 2009, MBARI Western Flyer 2011, CCGS Tully 2016, and KM1812 Kilo Moana 2018 research cruises for their completion of sampling and preliminary data collection.

## Table of Contents

## List of Tables

## List of Figures

# List of Abbreviations and Symbols

**Abbreviations**

| | |
|---|---|
| AAV | Area of Active Venting |
| Anhy | Anhydrite |
| ASHES | Axial Seamount Hydrothermal Emissions Study |
| AUV | Autonomous underwater vehicle |
| BHMS | Bent Hill Massive Sulfide |
| CASM | Canadian American Seamount Expedition |
| CRS | Chromium reducible sulfur |
| Cov | Covellite |
| CDT | Canyon Diablo Troilite |
| CTD | Conductivity, Temperature, Depth |
| CuPy | Chalcopyrite |
| Endeavour | Endeavour Hydrothermal Vents Marine Protected area |
| EPR | East Pacific Rise |
| HCl | Hydrochloric acid |
| HOV | Human Occupied Vehicle |
| HU | Harvard University |
| IODP | International Ocean Drilling Program |
| JdFR | Juan de Fuca Ridge |
| MAR | Mid-Atlantic Ridge |
| MEF | Main Endeavour Field |
| MgPy | Magnetic Pyrite |
| MOR | Mid-ocean ridge |
| Mrc | Marcasite |
| ODP | Ore Drilling Program |
| Po | Pyrrhotite |
| Py | Pyrite |
| ROV | Remotely operated vehicle |

| | |
|---|---|
| SEPR | Southern East Pacific Rise |
| SMAR | Southern Mid-Atlantic Ridge |
| SMS | Seafloor massive sulfide |
| UMD | University of Maryland, College Park |
| V-CDT | Vienna-Canyon Diablo Troilite |
| Wz | Wurtzite |

**Symbols**

| | |
|---|---|
| Δ | Capital delta |
| δ | Lower case delta |
| ‰ | Per mil |

## List of Appendices

# 1. Introduction

## 1.1 Preface

At mid-ocean ridges, magma bodies beneath the seafloor provide a heat source that causes seawater that has infiltrated the oceanic crust to become thermally buoyant and drive convective fluid circulation beneath the seafloor. The hot, thermally buoyant water (or hydrothermal fluid) rises through fluid pathways (typically faults) in the crust and is discharged at the ocean-seafloor interface (e.g., Jamieson et al., 2016 and references therein). Dissolved chemical constituents in the hydrothermal fluid can be derived from leaching of host rocks, solutes originally dissolved in seawater, magmatic volatiles, and biological processes (McDermott et al., 2015 and sources therein). The chemical constituents present in hydrothermal fluid can precipitate upon the changes in temperature, pH and redox conditions associated with mixing of the hot (up to ~400°C), acidic, reduced hydrothermal fluid with cold (~2°C), alkaline, oxidized ambient seawater at hydrothermal vents, forming mineral accumulations on the seafloor such as chimneys and mounds (Hannington et al., 1995). When the precipitates are composed primarily of sulfide minerals, the aggregates of sulfide, sulfate, and silicate minerals that comprise the vents and mounds are referred to as seafloor massive sulfide (SMS) deposits.

Some known SMS deposits are large enough (e.g., > 1 Mt) to be potentially economically viable as sources for Cu, Zn, Pb, Ag, and Au (Hannington et al., 2011 and sources therein). The formation of large SMS deposits, however, required specific geological criteria to be satisfied. Specifically, large SMS deposit formation requires a long-lived hydrothermal system and a consistently maintained trapping mechanism (e.g.,

sediment), for the precipitation of metal sulfide minerals. Determining the factors affecting fluid cycling and fluid-rock interactions at hydrothermal vent locations can help constrain if geological and biological conditions at a site may be favourable for forming large SMS deposits.

Stable isotopes of elements present in mineral deposits can be used to trace processes associated with fluid cycling in submarine hydrothermal systems (e.g., Ohmoto, 1972; Ono et al., 2007). In this thesis, stable isotopes are applied as a tool to identify and constrain different geologic conditions related to the formation of seafloor massive sulfide deposits. Multiple S isotope studies involve characterizing the relative abundances of four different stable S isotopes ($^{33}S$, $^{34}S$, and $^{36}S$, relative to $^{32}S$) by quantifying the deviation of isotope abundance ratios from a standard reference material. The use of multiple S isotope signatures to constrain fluid/rock interactions in hydrothermal systems is relatively new and thus several outstanding questions remain regarding the application of this approach to modern SMS forming systems (Ono et al., 2007; Jamieson et al., 2013; McDermott et al., 2015).

## 1.2 Objectives

The Juan de Fuca mid-ocean ridge, off the coast of Vancouver Island, B.C. and the Pacific Northwestern United States, hosts several hydrothermal systems in geologically-distinct settings, including Middle Valley, a sediment-infilled ridge segment that contains one of the largest known seafloor massive sulfide deposits on the modern ocean floor; Axial volcano, a sediment-free active submarine hotspot volcano; and the Endeavour Hydrothermal Vents Marine Protected Area, which is hosted on a basaltic substrate that

has been hypothesized to have erupted onto previously deposited sediments (Lilley et al., 1993; You et al., 1994; Kelley et al., 2012; Seyfried et al., 2003). At these sites, the multiple S isotopic compositions of hydrothermal precipitates were determined in order to investigate differences in hydrothermal S cycling within these environments, and link these differences to the presence of subseafloor buried sediments and the potential for formation of large, sediment-hosted SMS deposits. In this thesis, I hypothesized that interactions between hydrothermal fluids and sediments may be identified by isotopic signatures that record kinetic fractionations associated with microbial sulfate reduction. The S isotope signatures were investigated through the comparison of results from known sedimented and sediment-free sites (Middle Valley and Axial Volcano, respectively) and a site of unknown, but hypothesized buried sediment (Endeavour).

Axial Volcano S isotope signatures were hypothesized to be representative of endmember S mixing between seawater sulfate and basalt-derived S. Middle Valley S isotope signatures were hypothesized to be representative of S mixing between basalt-derived S and seawater sulfate with the added influence of biogenic sulfide contribution from sediments. The detection of potential buried sediment was hypothesized to be identifiable at Endeavour by using a S reservoir mixing model to compare Endeavour S isotope signatures with both S isotope signatures from Middle Valley and Axial Volcano as sedimented and sediment-free endmembers.

The main objectives of this thesis were: 1) To characterize the S isotope signatures of seafloor massive sulfide deposits from geologically different environments in order to link S cycling associated with submarine hydrothermal systems to the geology of the

substrate; 2) To investigate multiple S isotope signatures as they relate to fluid/rock and microbial interactions in modern hydrothermal environments; and 3) To substantiate the use of S isotope signatures as a proxy for identification of potentially large seafloor massive sulfide deposits.

### 1.3 Submarine Hydrothermal Systems

Hydrothermal vents occur where seawater infiltrates permeable oceanic crust at geologic settings associated with volcanism, such as subduction related volcanic arcs and back-arcs, intraplate volcanoes, and mid-ocean ridges (Hannington et al., 2004). The relative proximity of the magma chamber to the seafloor causes the infiltrated seawater to become heated, driving chemical exchange with the host rock and convective circulation (Bischoff and Seyfried, 1978; Bischoff and Rosenbauer, 1988; Edmond et al., 1979). Upon progressive heating of seawater, anhydrite, which has retrograde solubility, will begin to precipitate when the fluid reaches 150˚C (Elderfield et al, 1999), followed by precipitation of magnesium-hydroxy-sulfate hydrate at 250˚C (Janecky and Seyfried, 1983). As the temperatures continue to increase as the fluid descends further, the now-modified seawater will leach metals and S from the surrounding host rock (Hannington et al., 1995). At temperatures of ~400˚C, the hot hydrothermal fluid becomes thermally buoyant, ascends to the seafloor along crustal permeability pathways, and discharges at the seafloor, leading to continuous subseafloor hydrothermal circulation and venting (Delaney et al., 1992; Hannington et al., 1995). When the hot hydrothermal fluid mixes with the cold ambient seawater at or near the seafloor, metal sulfides, sulfates, and amorphous silica precipitate,

leading to the formation of chimney structures and seafloor massive sulfide (SMS) deposits on the seafloor, and replacement style mineralization below the seafloor (Spiess et al., 1980, Hannington et al. 2005; Jamieson et al., 2014).

At sediment-free mid-ocean ridge (MOR) hydrothermal systems (e.g., East Pacific Rise [EPR] type), most of the metal sulfides (~95%) become entrained in the resultant hydrothermal plume emanating from the chimney, thereby dispersing over a wide area, either as sediment fallout or by dissolving back into seawater (Baker et al., 1985; Mottl and McConachy, 1990; Feely et al., 1994; Metz and Trefry, 1993). However, at locations proximal to continental shelves, turbidity currents can cause hydrothermal vents to be buried by terrigenous sediments (Davis et al., 1992a; Davis and Fisher, 1994). When the surrounding cold, dense, seawater infiltrates the sediments at hydrothermally active areas, fluid mixing below the seafloor results in the formation of an altered sediment reservoir cap, as well as a thermally insulated, highly permeable basement reservoir that promotes mineral precipitation below the seafloor (Davis et al., 1992a; Davis and Fisher, 1994; Zierenberg et al., 1993). This enhanced subseafloor mixing zone results in metal sulfides that would otherwise be lost in the hydrothermal plume to become trapped, thereby potentially forming larger SMS deposits (Davis et al., 1992a; Zierenberg et al., 1998).

## 1.4 Study Areas

### 1.4.1 The Juan de Fuca Ridge

The Juan de Fuca Ridge (JdFR) is a 490 km long, intermediate rate (full-spreading rate of ~6 cm/year) mid-ocean ridge that lies off the coast of Vancouver Island and the

Pacific Northwestern United States, and separates the Juan de Fuca and Pacific Plates (Barr and Chase, 1974; Vine and Wilson, 1965; Johnson and Embley, 1990; Chadwick et al., 2005). The JdFR is intersected by the Sovanco Transform Fault Zone and Nootka Fault Zone to the north, and the Blanco Transform Fault Zone to the south (Fig. 1.1)(Willoughby and Hyndman, 2005). The JdFR has seven geomorphologically distinct axial segments (listed from north to south): West Valley, Endeavour, Northern Symmetric, Coaxial, Axial, Vance, and Cleft (Fig. 1.1)(Van Ark et al., 2007). West Valley forms part of a distinct series of ridges and rift valleys: East Ridge, East Valley, Middle Ridge, Middle Valley, West Ridge, and West Valley (Barr and Chase, 1974; McManus et al., 1972). Around 10 to 15 thousand years ago, active spreading is thought to have shifted from the sediment infilled Middle Valley, to West Valley, which contains younger basalt flows that lack the alteration or oxide coatings typical of older, weathered basalt flows (Barr and Chase, 1974; Davis and Villinger, 1992). Further south, a mantle plume known as the Cobb hot spot exists beneath the Axial segment (Barr and Chase, 1974; Chadwick et al., 2005). Several of the segments have distinct axial valleys with widths from 1 to 8 km and corresponding axial graben walls that vary in height from ~50 m to ~250 m (Carbotte et al., 2006). The three hydrothermal vent fields on the JdFR that were investigated in this study are Middle Valley (located near the actively spreading West Valley Segment), Endeavour Hydrothermal Vents Marine Protected Area (hereafter referred to simply as 'Endeavour'), and Axial Volcano (Fig. 1.1). Both Endeavour and Middle Valley are currently considered volcanically inactive (Jamieson et al., 2013a; Goldstein et al., 1991; Johnson et al., 2000; Proskurowski et al., 2004; Riddihough, 1984; Volpe and Goldstein, 1993; Barr and Chase,

1974), while volcanic eruptions at the Axial have been recorded as recently as 2015 (Delaney, 2015).

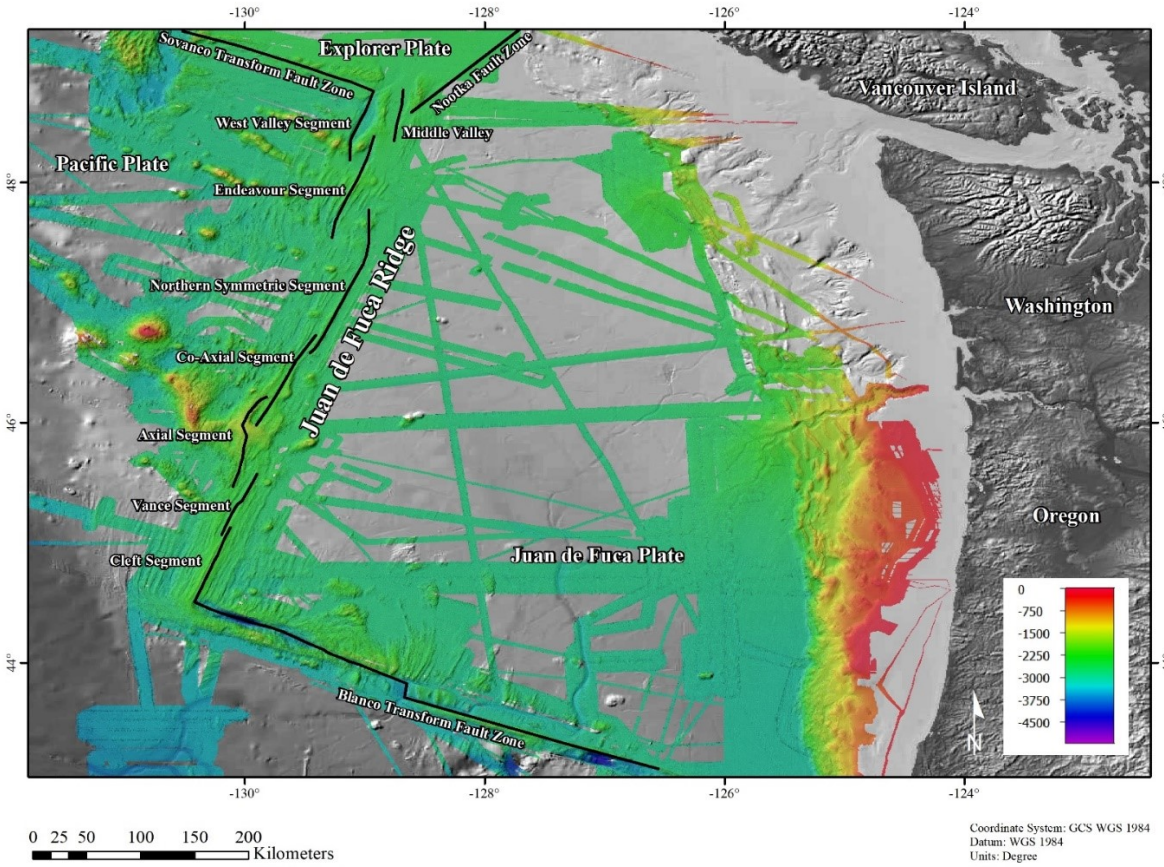


Figure 1.1: The Juan de Fuca Ridge, with corresponding segmentation and major geographic and geological features in the surrounding area. Greyscale bathymetry is satellite-derived gravity model of seafloor topography (Smith and Sandwell, 1997) with a resolution of 1-4 km. Coloured bathymetry (depths displayed in meters) represents ship-based acoustic multibeam sonar data (Merle, 2015) with a resolution of 10 to 200 m. Modified from Van Ark et al. (2007), Cousens et al. (2002) and Golden et al. (2003).

#### 1.4.1.1 Middle Valley

Middle Valley is a ~2460 m deep, ~50 km long, ~15 km wide sediment covered relict oceanic spreading center located on the northeastern most part of the Juan de Fuca Ridge, ~200 km off the coast of Vancouver Island (Cruse et al., 2008; Goodfellow and Franklin, 1993; Ames et al., 1993). Pleistocene turbiditic sediment buildup in the axial valley reaches a maximum thickness of ~2 km in the northern most region of the valley and thins southward to a minimum thickness of a few hundred meters (Davis and Villinger, 1992; Butterfield et al., 1994). Evidence for the shift in active seafloor spreading from Middle Valley, to West Valley (Fig. 1.2) includes magnetic anomaly patterns, and a relative lack of post-Pleistocene subsidence at Middle Valley when compared to West Valley and the Endeavour segment to the south (Davis and Villinger, 1992). The long lived (150,000 – 200,000 year-old) hydrothermal system at Middle Valley is thought to be maintained by an altered sediment cap reducing heat loss in the igneous basement (Golden et al., 2003; Scholten et al., 2000; Davis and Villinger, 1992; Goodfellow and Blaise, 1988). Middle Valley has two known active vent field areas: Dead Dog and Bent Hill (Davis and Villinger, 1992; Butterfield et al., 1994). These sites were the focus of Integrated Ocean Drilling Program (IODP) Expeditions 139 and 341 (Davis et al., 1992).

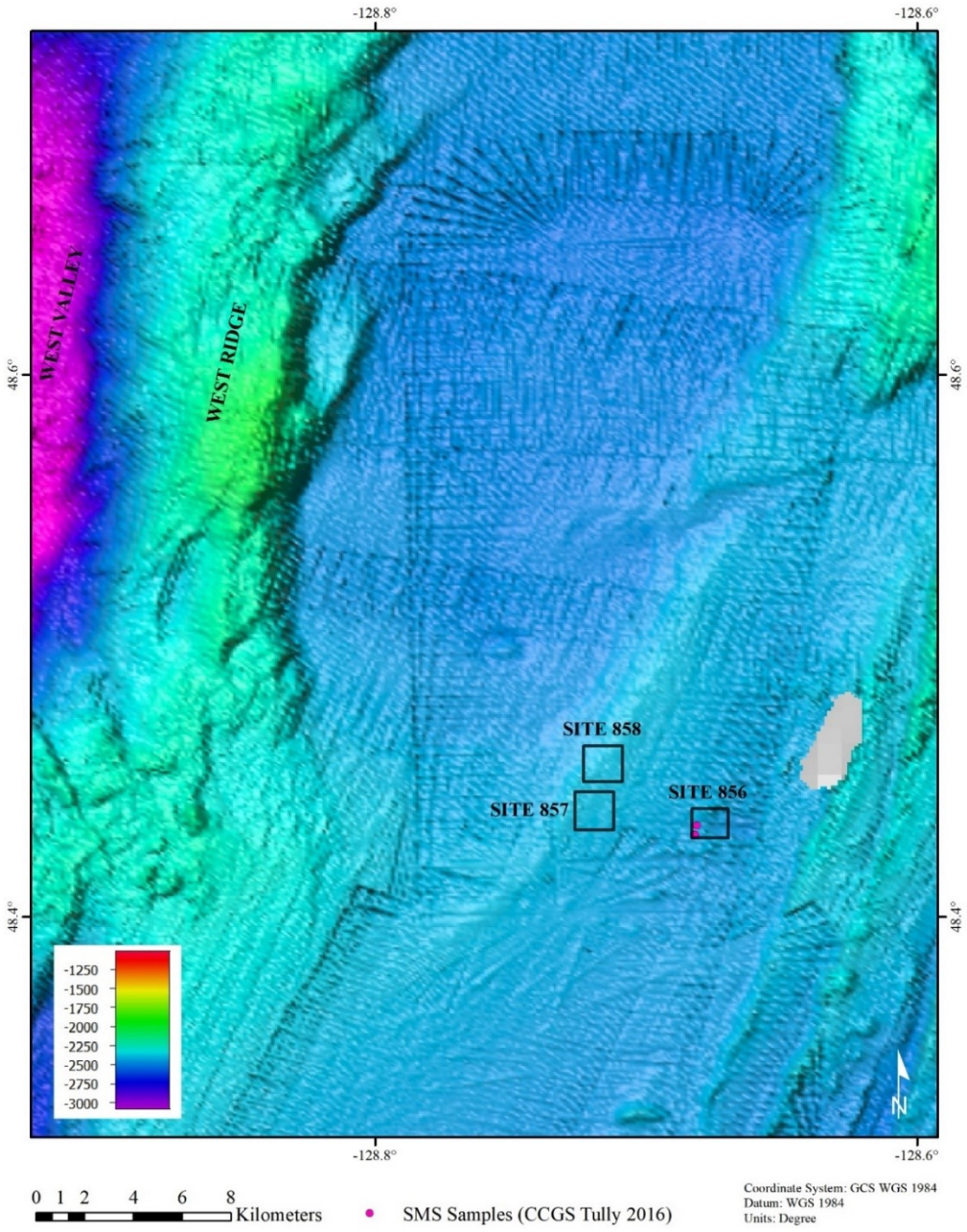


Figure 1.2: Map of Middle Valley, showing corresponding locations of the active vent fields. Coloured bathymetry (depths displayed in meters) represent ship-based acoustic multibeam sonar data (Merle, 2015) with a 100 m grid cell size. Greyscale bathymetry (used to fill in gaps) is satellite-derived gravity model of seafloor topography (Smith and Sandwell, 1997) with a resolution of 1-4 km. Modified from Peter et al. (1994) and Barr and Chase (1972). Samples analyzed from Site 856 in this study, indicated by pink circles on the map, are R1942-Rck10, R1942-Rck16, and R1942-Rck8.

The Dead Dog hydrothermal vent field is a ~700 m by 250 m cluster of hydrothermal vents located within the Area of Active Venting (AAV), also known as IODP Site 858 (Fig. 1.2)(Davis et al., 1992c; Davis and Villinger, 1992; Fisher et al., 1997). Dead Dog contains at least eight main vent sites that are primarily comprised of ≤ 1.2 m tall sulfide-poor, anhydrite-rich chimneys situated atop mounds of up to 15 m in height and 35 m in diameter (Davis et al., 1992c; Ames et al., 1993). Evidence from recovered drill core indicate that the subsurface at Dead Dog is generally comprised of hydrothermally altered hemipelagic and turbiditic sedimentary sequences that contain disseminated pyrite, carbonate nodules, barite, and anhydrite (Davis et al., 1992c). Hydrothermal fluids at Dead Dog reach up to 281°C (Cruse et al., 2008). Fluids collected from boreholes at site 857 (Fig 1.2), a site without active venting located ~1.6 km south of Dead Dog, were similar to those from Dead Dog, with fluid temperatures, alteration mineral assemblages, and fluid chemistry indicating that the two sites likely share a source reservoir (Kurnosov et al., 1994; Davis and Fisher, 1994). Viable S-bearing minerals were not found in the Dead Dog samples available for this study. Therefore, the data and discussion of sediment hosted SMS deposits for this project relies on sulfide samples collected from Bent Hill.

Bent Hill is a ~500 m across, ~60 m high turbiditic sediment mound that was uplifted by late Pleistocene to Holocene intrusions and is located at ODP Site 856 (Fig. 1.2)(Davis et al., 1992b; Davis and Fisher, 1994). The intrusive activity is interpreted to be at least a few thousand years old based on the lack of an associated thermal anomaly at the site (Davis and Villinger, 1992). The Bent Hill Massive Sulfide Deposit (BHMS), which is situated ~100 m south of the southern flank of the mound, is a 35 m high, over

100 m thick sulfide mound containing one of the largest known oceanic sulfide deposits, with an estimated 8.8 x $10^6$ tons of sulfide mineralization (Zierenberg et al., 1998). A second, slightly younger, smaller massive sulfide deposit called ODP mound is situated ~300 m to south of BHMS (Ames et al., 1993; Davis et al., 1992b). The ODP mound hosts one active sulfide-poor anhydrite chimney spire that has a maximum recorded hydrothermal fluid temperature of 264°C (Ames et al., 1993).

Overall, the BHMS deposit consists largely of primary pyrrhotite and pyrite, with secondary pyrite and magnetite occurring as coprecipitated products of primary pyrrhotite oxidation (Duckworth et al., 1994). The BHMS deposit is underlain by a ~110 m thick copper sulfide-rich stockwork zone (Zierenberg et al., 1998). Massive sulfide at ODP Mound is zinc-rich and consists largely of sphalerite, pyrite, pyrrhotite, marcasite and magnetite, and minor copper sulfide minerals. Alternating massive sulfide horizons at ODP Mound are also underlain by individual copper rich sulfide stockwork zones, similar to the BHMS deposit (Fouquet et al., 1998).

#### 1.4.1.2 The Endeavour Hydrothermal Vents Marine Protected Area

The Endeavour Hydrothermal Vents Marine Protected Area is a 2050 m deep, ~100 $km^2$ hydrothermally active rift zone located on the 90 km-long Endeavour Segment, southwest of Middle Valley (Karsten et al., 1986). Though the Endeavour segment is currently considered volcanically inactive (Riddihough, 1984; Goldstein et al., 1991; Volpe and Goldstein, 1993; Johnson et al., 2000; Proskurowski et al., 2004; Jamieson et al., 2013a), there is seismic evidence of an extensive series of axial magma chambers existing 1.9 – 4 km below the seafloor, that are indicative of the possibility of renewed volcanism

at Endeavour (Van Ark et al., 2007; Carbotte et al., 2012). Most of the documented high temperature hydrothermal activity at Endeavour occurs at five main active vent fields (listed from north to south): Sasquatch, Salty Dawg, High Rise, Main Endeavour (MEF), and Mothra (Fig. 1.3)(Kelley et al., 2012).

Active venting at the Sasquatch Hydrothermal Field occurs within a ~25 m by 25 m area and consists of ten ≤ 6 m high sulfide chimneys. Hydrothermal fluid temperatures at Sasquatch reach up to 289°C (Glickson et al., 2006). An area of oxidized sulfide debris and hydrothermal sediments extends 200 m south of the actively venting area and contains several extinct sulfide structures ≤ 10 m tall, indicating periods of more vigorous hydrothermal activity in the past (Glickson et al., 2006). Barite $^{226}$Ra decay measurements indicate that Sasquatch has been hydrothermally active for at least ~1450 years (Jamieson et al., 2013a).

The Salty Dawg Hydrothermal Field is comprised of at least 25 vent structures of up to 25m in height. Venting is generally diffuse; however, temperatures can reach up to 296°C at some of the more active vents (Kelley et al., 2001a). Fisheries and Oceans Canada has classified Salty Dawg as an "observational research site" in order to minimize potentially disruptive visits and intrusive research activities, so it is seldom visited by researchers.

High Rise is a 350 m long by 150 m wide hydrothermal vent field that trends parallel to the ridge axis. Hydrothermal venting at High Rise occurs predominantly at ten large (≤ 45 m high) active sulfide structures. In addition, many small, lower temperature, inactive, and diffuse vents are concentrated along fractures throughout the vent field (Rogibou et al., 1993). Hydrothermal fluid temperatures recorded during the EAGER research cruise in

2009 varied between 306 and 340°C (Holden, 2009). Radium-226 decay measurements indicate that High Rise has been hydrothermally active for a minimum of ~850 years (Jamieson et al., 2013a).

The MEF is a ~350 m by 180 m hydrothermal vent field located on the western edge of the axial valley (Delaney et al., 1992). The vent field hosts 19 actively venting large (≤ 20m) black smoker sulfide edifices with fluid temperatures of up to 402°C (Delaney et al., 1984; Delaney et al., 1992; Kelley et al., 2014). Radium-226 decay measurements of barite samples taken from MEF indicate that the site has been hydrothermally active for at least ~2300 years (Jamieson et al., 2013a).

Mothra is a ~500m long hydrothermal vent field consisting of six steep-sided ≤ 20 m high active sulfide chimney clusters that trend parallel to the ridge and are distributed 40 – 200m apart (Glickson et al., 2007; Kelley et al., 2001b). Clusters at Mothra have multiple active > 5m high sulfide structures located < 20 m apart and are surrounded by 10 – 15 m of sulfide debris (Glickson et al., 2007). Venting at Mothra is generally diffuse, with venting temperatures that range from 30-220°C, with isolated fluids from singular black smokers reaching temperatures of 302°C (Kelley et al., 2001b).

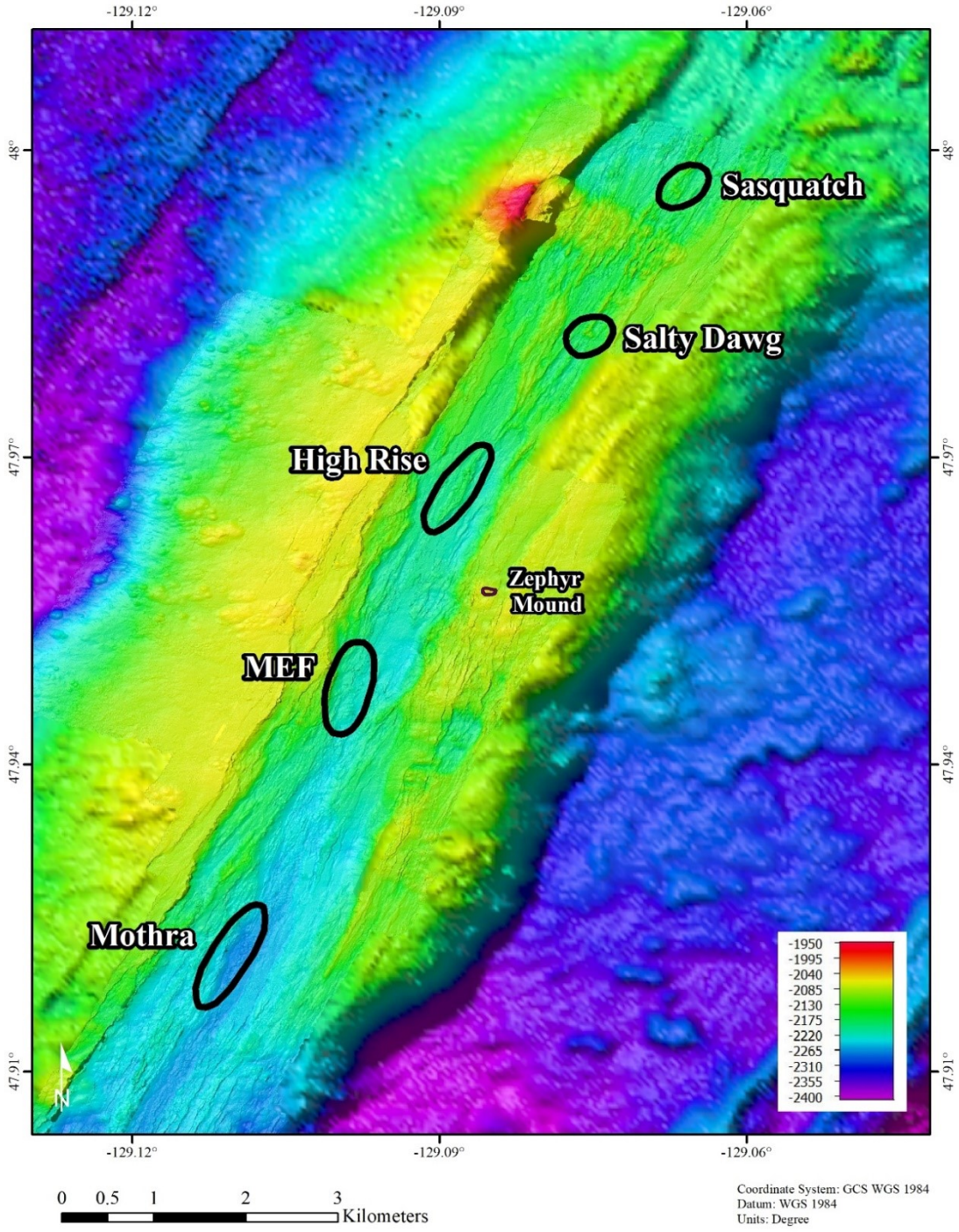


Figure 1.3: The five major hydrothermal vent fields at Endeavour, as well as Zephyr Mound, displayed using high resolution 2 m autonomous underwater vehicle-derived multibeam sonar bathymetry from Clague and Caress (2015) overlaid on top of 30 m ship-based multibeam sonar bathymetry from Kelley et al. (2015).

The Endeavour vent fields (Fig. 1.3) host over 800 individual chimneys, all of which are located within a 15 km span of the axial valley (Delaney et al., 1992; Glickson et al., 2007; Rogibou et al., 1993; Clague et al., 2008; Kelley et al., 2002; Kelley et al., 2012). The steep-sided sulfide edifices that are characteristic of these active vent fields typically have mineral assemblages containing pyrite, wurtzite, sphalerite, pyrrhotite, chalcopyrite, marcasite, amorphous silica, anhydrite, and barite (Delaney et al., 1992; Kristall et al., 2006; Robigou et al., 1993; Tivey and Delaney, 1986; Jamieson et al., 2013a). Radium-226 decay measurements of a barite sample taken from outside the axial valley indicate that regional hydrothermal venting at Endeavour has been active for a minimum of ~6000 years (Jamieson et al., 2013a).

Zephyr Mound is a 90 m diameter by 26 m high sulfide mound with a volume of 52,500 $m^3$ that contains an estimated ~163,000 t hydrothermal sulfide material. Sulfide material from the Zephyr Mound indicates that the mound is at least 1,800 years old (Jamieson et al., 2014).

Elevated Br/Cl, boron, ammonia and methane concentrations, coupled with heavy boron isotope data from vent fluids at Endeavour indicate the possibility of buried sediments beneath the surface basalt flows at Endeavour (Lilley et al., 1993; You et al., 1994; Kelley et al., 2012; Seyfried et al., 2003). The location of the Endeavour segment near the extent of continent derived sediment further supports this hypothesis (Fig. 1.4). Buried sediment at Endeavour could potentially host SMS deposits similar in size and composition to those at Middle Valley.

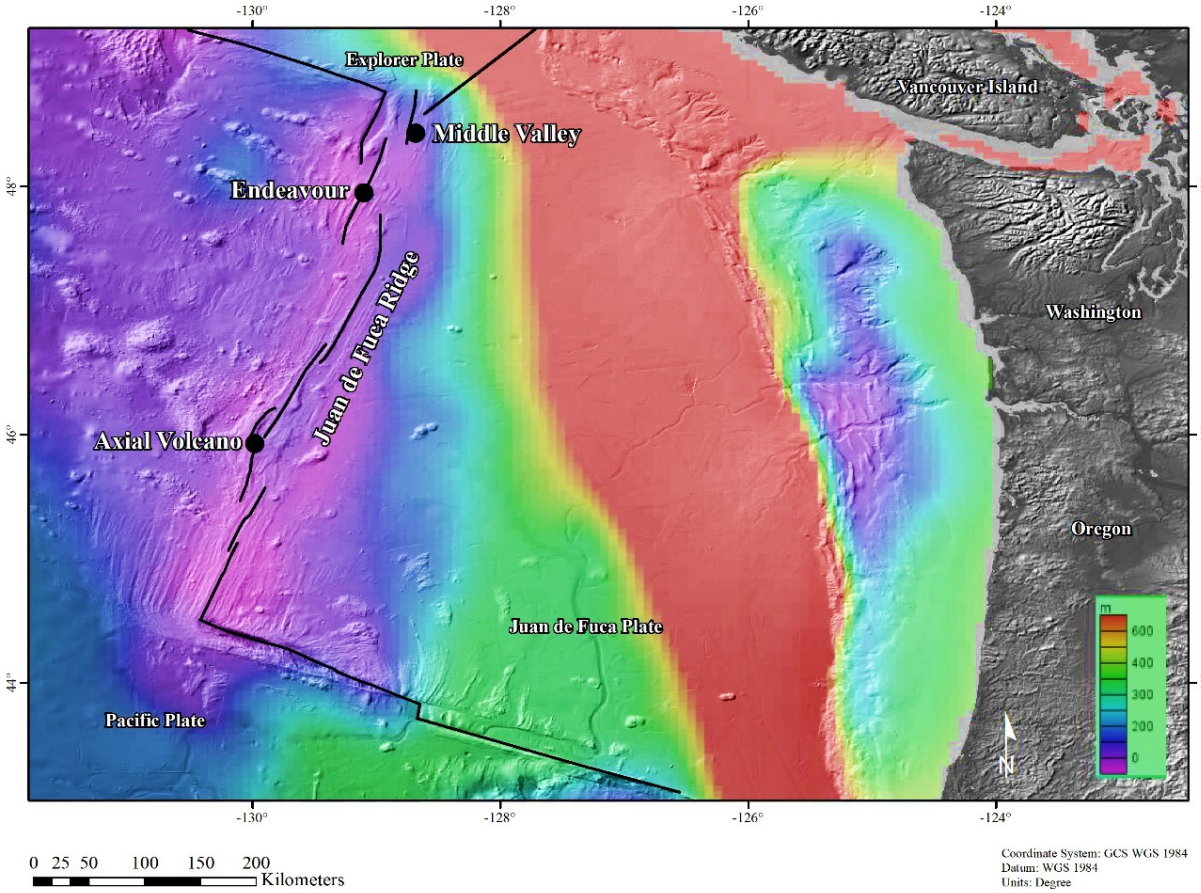


Figure 1.4: Sediment thickness (in meters) of the three vent fields in this study and surrounding area. Sediment thickness data were compiled by Divins (2003) and have a grid spacing of 5 arc-minutes. Sediment thickness is faded and superimposed on greyscale bathymetry, which is a satellite-derived gravity model of seafloor topography (Smith and Sandwell, 1997) that has a resolution of 1-4 km. Map features modified from Van Ark et al. (2007), Cousens et al. (2002) and Golden et al. (2003).

#### 1.4.1.3 Axial Volcano

Axial Volcano is a ~1500 m deep, ~600 $km^3$ active shield volcano generated by a hotspot located at the intersection of the Axial segment on the southern Juan de Fuca Ridge (Hannington et al., 2005; Helo, et al., 2008; Embley et al., 1990) and the Cobb-Eickelberg Seamount Chain (Chadwick et al., 2005). Multiple recent lava flows have been documented at Axial Volcano, including eruptions in 1998 (Embley et al., 1999), 2011 (Chadwick et al., 2011), and 2015 (Delaney, 2015). Recent substrate samples collected from Axial are comprised primarily of basaltic lava flows and volcaniclastic debris (Helo et al., 2008). Extensive, thick (≤ 2 m) deposits of volcanic ash surround the volcano, indicating eruptive explosivity in conjunction with Axial's generally effusive basalt flows, a factor that is attributed to high levels of $CO_2$ in the magma chamber (Helo et al., 2011). High $CO_2$ concentrations, that suggest a direct input of magmatic volatiles into the hydrothermal system, have been documented in boiling hydrothermal fluids from several chimneys at Axial (Butterfield et al., 1990; Butterfield et al., 2004). Of the three sites in this study, Axial Volcano is located at the greatest distance from the continental shelf (~480 km off the coast of Oregon, Fig. 1.4). Axial Volcano's distal location in relation to the continental shelf, recent volcanic activity, and basaltic seafloor substrate are all evidence of a lack of turbiditic sediments in the area (Fig. 1.4).

Low temperature vents, as well as some high temperature black smokers, are found primarily on the walls and floor of the 21 $km^2$ horseshoe-shaped summit caldera (Embley et al., 1990). There are three main hydrothermal vent fields that occupy Axial's caldera:

Axial Seamount Hydrothermal Emissions Study (ASHES), Canadian American Seamount Expedition (CASM), and the International District, in addition to diffuse flow sites (Fig. 1.5)(Hannington and Scott, 1988; Kelley et al., 2014).

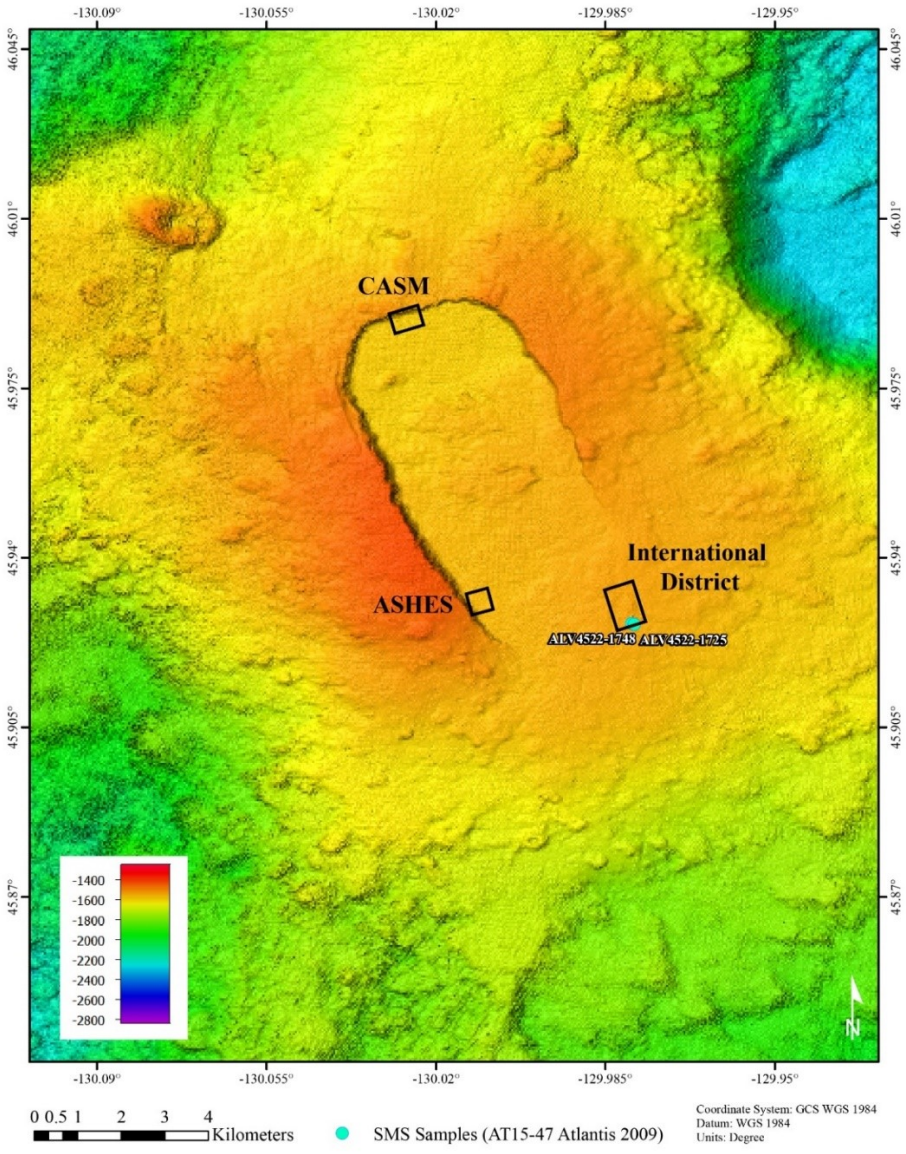


Figure 1.5: The Axial Volcano caldera with recorded locations of samples used in this study, as well as approximate locations of major vent fields (modified from Kelley et al., 2014). Bathymetry (depths shown in meters) is from Chadwick et al., (2015) and has a resolution of 25 m.

The ASHES hydrothermal field (ASHES, 1986), located in a shallow depression on the southwestern side of the caldera, contains less than 10 small (< 4 m) chimneys that occur along a ~60 m stretch of the base of the caldera wall (Kelley et al., 2014). Recent vent fluid temperature measurements at ASHES recorded a maximum temperature of 321°C (Holden et al., 2008). Chimney structures are composed primarily of anhydrite, pyrite, and sphalerite (Kelley et al., 2014).

The CASM hydrothermal field is located at a fissure near the northern extent of the caldera (CASM, 1985). Several large sulfide edifices between 4 - 10 m tall are present ~20 m west of the northernmost point of the fissure, in conjunction with abundant small chimneys within the fissure and throughout the field (Embley et al., 1990; Hannington and Scott, 1988). The highest recorded vent fluid temperature at CASM is 291˚C (Chadwick et al., 2015). A chimney spire analyzed by Hannington and Scott (1988) was found to contain primarily amorphous silica, sphalerite, wurtzite, marcasite, barite, galena, and chalcopyrite, as well as minor pyrite, jordanite, and lead-arsenic-antimony-silver sulphosalts.

The International District hydrothermal field, located on a fissure system on the southeastern part of the caldera, is ~60 m across and ~15 active structures of up to ~16 m tall. Recorded hydrothermal fluid temperatures at the El Guapo vent in the International District reached up to 347˚C in 2010. However, more recent measurements in 2011 showed a marked temperature drop to 211˚C after the 2011 eruption (Kelley et al., 2014). Chimneys in the International District are composed primarily of sulfide and anhydrite (Chadwick et al., 2013). Axial Volcano samples used in this study are all from the International District (EAGER, 2009).

## 1.5 Sulfur Isotopes

Isotopes are elements with the same number of protons, but different number of neutrons, and therefore different atomic masses. Sulfur has four stable isotopes ($^{32}S$,$^{33}S$, $^{34}S$ and $^{36}S$, with abundances of 0.9503957, 0.0074865, 0.0419719, and 0.0001459, respectively [Ding et al., 2001]), and, because S exhibits several different oxidation states in nature, it is an important constituent for many chemical, physical and biological processes, many of which result in isotopic fractionation (i.e., change in isotopic composition) of reactants and products. These qualities make S an extremely useful element for tracking the movement of S in natural environments.

Sulfur isotopes are commonly expressed using delta notation (Equation 1.1), which quantifies a deviation of the S isotopic composition of a material from a standard (Shanks et al., 1995), most often the Vienna Canyon Diablo Troilite (V-CDT) or older Canyon Diablo Troilite (CDT):

Equation 1.1

$$\delta\,^{34}S = \left(\frac{^{34}R_{Sample}}{^{34}R_{Standard}} - 1\right) * 1000\ (‰)$$

where (R) represents the isotopic ratio of a rare isotope (e.g., $^{33}S$, $^{34}S$, $^{36}S$) with respect to the most abundant isotope ($^{32}S$) (i.e.,$^{34}R$ represents $^{34}S/^{32}S$). For S isotopes, delta notation can also be used to express ratios for $^{33}S/^{32}S$ and $^{36}S/^{32}S$. The fractionation factor (α) is used to express the partitioning of S isotopes at equilibrium and is defined as the ratio of a sample ($R_x$) divided by the same ratio of another sample ($R_y$) (i.e., $\alpha_{x\text{-}y} = R_x/R_y$). The

isotope composition, δ, is related to the fractionation factor, α, of a given element such that:

Equation 1.2

$$\alpha_{x-y} = \frac{1000+\delta_x}{1000+\delta_y}$$

Equation 1.3 is a commonly used as a mathematical approximation of Equation 1.2 due to its similarity to delta value differences for fractionation factors close to unity, which applies to typical S isotope ratios in natural systems:

Equation 1.3

$$1000 \ln \alpha_{x-y} \approx \delta_x - \delta_y$$

Equation 1.4 defines Δ, which is used to express differences in δ values, and is therefore approximate equivalent to 1000 ln α, and therefore shows the relation between α and Δ:

Equation 1.4

$$\Delta_{x-y} = \delta_x - \delta_y$$

Positive δ values indicate an isotopically heavy sample relative to the standard, while negative δ values indicate an isotopically light sample relative to the standard. Since different S reservoirs often have different isotopic signatures, the relative abundance of S isotopes allows for isotope ratios to be used as tracers for the sources of S in a given sample, thereby fingerprinting the occurrence and relative contributions of S resulting from different natural processes (Shanks et al., 1995). Kinetic isotope effects, or non-equilibrium fractionations, occur when isotopes are fractionated without the achievement of isotopic equilibrium and can be especially useful to fingerprint nonequilibrium

fractionation processes such as microbial sulfate reduction (MSR) (Shanks et al., 1995). These isotopic differences between various S reservoirs make S isotopes a useful tracer for determining processes affecting fluid mixing and S cycling in hydrothermal systems (e.g., Adshead, 1996; Hannington et al., 2005; Shanks et al., 1995).

### 1.5.1 Sulfur-34

Sulfur isotopes (normally $^{32}S$ and $^{34}S$ because they are the most abundant isotopes) have long been used to determine the sources of S in SMS deposits, which in turn provides insight into subsurface processes controlling hydrothermal circulation (e.g., Adshead, 1996; Hannington et al., 2005; Shanks et al., 1995). Submarine hydrothermal systems from different geologic settings can have different isotopic signatures that correspond to varying degrees of influence from multiple S reservoirs. In general, sulfide $\delta^{34}S$ values from "typical" sediment-free mid-ocean ridges tend to be slightly positive relative to both CDT and V-CDT. For example, 95% of $\delta^{34}S$ values for hydrothermal sulfide samples from East Pacific Rise (hereafter used as a point of comparison for "typical" MOR systems) range from approximately 1‰ to 5‰ (Hannington et al., 2005). Sulfide minerals from sedimented mid-ocean ridges, volcanic arcs, and back-arc basins typically have a greater range in $\delta^{34}S$ values than sulfide minerals from sediment-free MOR systems. For example, $\delta^{34}S$ values range from approximately -34‰ to 14‰ and -14‰ to 11‰ for sedimented and arc settings, respectively (Hannington et al., 2005; Li et al., 2016). The various S reservoirs in MOR hydrothermal systems that contribute to hydrothermal fluid and sulfide deposit S isotope compositions each have distinct $\delta^{34}S$ values. Vent fluid $H_2S$ $\delta^{34}S$ values can span a broad range from slightly negative (~-5‰) to positive (~8‰) (Shanks et al.,

2001 and references therein). Mid-ocean ridge basalts (MORB) and related volatiles generally have $\delta^{34}S$ values of approximately zero (within the range of -1‰ to 1‰) (Sakai et al., 1982; 1984). Seawater sulfate is relatively isotopically heavy with a near-constant $\delta^{34}S$ value of 21‰ in the modern ocean (e.g., Shanks et al., 2001), while $\delta^{34}S$ values of reduced S products from MSR are isotopically light, with an approximate range of -15‰ to -35‰ (e.g., Shanks et al., 1995; Goodfellow and Blaise, 1988).

### 1.5.2 Multiple Sulfur Isotopes

Sulfur isotope fractionation is controlled by isotopic mass differences for thermodynamic and most kinetic physiochemical processes (Urey, 1947), causing near-linear mass-dependent fractionation (MDF) relationships of approximately ½ for $\delta^{33}S$ and 2 for $\delta^{36}S$, relative to $\delta^{34}S$ (Hulston and Thode, 1965a; 1965b). Until recently, most studies involving the measurement of stable S isotopes only focused on the two most abundant S isotopes ($^{32}S$ and $^{34}S$), assuming MDF would cause any analysis of $^{33}S$ and $^{36}S$ to be redundant due to these mass dependent relationships. However, the fractionation laws for some kinetic fractionation processes deviate from traditional MDF relationships, leading to variations which are quantified as $\Delta^{33}S$ and $\Delta^{36}S$ values (e.g., $\Delta^{33}S \cong \delta^{33}S - 0.5 \times \delta^{34}S$; see section 2.3.1 for discussion of the different definitions for $\Delta$ values; Johnston et al., 2005; Farquhar et al., 2003; Young et al., 2002). The resultant systematic isotopic variations can be used to identify distinct geological and biological processes in natural hydrothermal systems, especially processes that may not be distinguishable using traditional $\delta^{34}S$ analyses (e.g., Ono et al., 2006; Ono et al., 2007; McDermott et al., 2015). Non-traditional

deviations from expected equilibrium MDF relationships can be either mass independent or mass dependent. Mass independent fractionation (MIF) is caused by processes not feasibly attributed to established mass fractionation laws, such as photolysis of S-bearing gaseous molecules (Farquhar and Wing, 2003 and sources therein). Mass dependent fractionation can result in systematic variations between fractionation factors for $\delta^{33}S$, $\delta^{34}S$ and $\delta^{36}S$ that differ from expected thermochemical equilibrium (such as microbial sulfate reduction [Farquhar et al., 2003) and result in non-zero $\Delta^{33}S$ and $\Delta^{36}S$ values.

#### 1.5.2.1 Applications in Archean rocks

The potential utility of multiple S isotopes for use in terrestrial geologic systems was first documented by Farquhar et al. (2000), who discovered significant mass independent fractionation-derived deviations in $\delta^{33}S$ and $\delta^{36}S$ from standard MDF relationships in Archean supracrustal rocks. Farquhar and Wing (2003) proposed a three-stage model of the evolution of Earth's early S cycle. Stage I, from 3.8 to 2.45 Ga, is characterized by mass independent fractionation with $\Delta^{33}S$ of between -2 and 4‰ due to photochemical reactions of $SO_2$ and SO driven by deep ultraviolet radiation in an oxygen-poor atmosphere. Stage II, from 2.45 to 2 Ga, produced measurably significant $\Delta^{33}S$ variances indicative of mass independent fractionation, but the variances are considerably smaller than those seen in Stage I, most likely due to the beginning of oxygen stabilization in Earth's early atmosphere coupled with the onset of oxidative weathering. Stage III, from 2 Ga to present, is dominated by MDF consisting primarily of $\Delta^{33}S$ values generally less than 0.2‰ due to an oxygen-rich atmosphere that resulted in a UV blocking ozone layer and oxidizing conditions that destabilized reduced S compounds in the surface

environment (Farquhar and Wing, 2003). Since significant mass independent fractionation was the product of an oxygen-poor atmosphere and generally constrained to the Archean, variations in $\Delta^{33}S$ of <0.2‰ in post-Archean environments can be ascribed to mass-dependent, non-equilibrium S isotopic systematics.

#### 1.5.2.2 Applications in Modern Marine Systems

Analyses of multiple S isotopes from modern natural S-bearing materials have documented isotopic values that record MDF processes that do not all abide by the same MDF laws and therefore differ from that of expected thermochemical equilibrium (Johnston et al., 2005; Farquhar et al., 2003; Young et al., 2002). Consequently, samples from post-Archean geological processes can have $\Delta^{33}S$ and $\Delta^{36}S$ values that show small, but quantifiable systematic variations (Ono et al., 2006; Ono et al., 2007).

Several recent studies (data are summarized in Fig. 1.6 and Fig. 1.7) have attempted to constrain the fractionation processes and associated multiple S isotope values of products of modern seafloor hydrothermal systems. Studies by Johnston et al. (2014) and Tostevin et al. (2014) both constrained the S isotope values of modern seawater. Their reported values indicate that the ocean is a well-mixed reservoir with an average seawater sulfate $\delta^{34}S$ value of 21.15‰ and a $\Delta^{33}S$ value of 0.048‰. Labidi et al. (2014) reported near zero $\delta^{34}S$ and $\Delta^{33}S$ values for Pacific-Antarctic Ridge basalts, with minor positive enrichments of approximately 1‰ attributed to sulfide assimilation (i.e., incorporation of hydrothermally-derived sulfide mineral precipitation into basalt flows during eruptive events). Near zero multiple S isotope values were also reported for unaltered basalts by Ono et al. (2012) and Peters et al. (2010). These studies helped define endmember multiple

S isotope values for the different sulfur reservoirs affecting modern submarine hydrothermal systems.

Ono et al. (2007) was the first study to apply multiple sulfur isotope analyses to active modern hydrothermal submarine systems. The authors utilized the S isotope signatures of sulfide minerals and vent fluid $H_2S$ from active hydrothermal vent systems at two sites on the East Pacific Rise, and two sites on the Mid-Atlantic Ridge, to determine the source of S in each system. The combined values indicate that most of the sulfur contained in sulfide minerals from these systems was derived from host rock leaching, with evidence of minor incorporation of reduced seawater sulfate. Low $\Delta^{33}S$ values are indicative of negligible biogenic sulfide input at all four sites.

Ono et al. (2012) compared multiple S isotope signatures of sulfide minerals in altered peridotites from the Iberian Margin and Hess Deep to signatures of sulfides in altered basalts from the Juan de Fuca Ridge in order to constrain biogenic influence on secondary sulfide precipitates. All three locations had similar $\delta^{34}S$ values. Variations in $\Delta^{33}S$ values were attributed to closed system sulfate reduction occurring at the peridotite hosted sites and open system sulfate reduction occurring at the basalt hosted site.

McDermott et al. (2015) conducted multiple S isotope analyses on chalcopyrite, elemental S, and fluid $H_2S$ from a sedimented and a sediment-free mid-ocean ridge hydrothermal system (Guaymas and the Southern East Pacific Rise, respectively), as well as two back arc systems (Eastern Manus Basin and Lau Basin), in an attempt to further constrain MDF processes in modern marine hydrothermal systems. All $\Delta^{33}S$ values were near zero, indicating the primary sources of hydrothermal S were abiotic seawater sulfate

reduction, host rock leaching, and S disproportionation. Specifically, positive $\delta^{34}S$ values from Lau Bain and southern East Pacific rise (SEPR) were attributed to seawater sulfate reduction and host rock leaching, while negative values from Manus Basin were due to a greater influence of magmatic S disproportionation (i.e., the speciation of magmatic $SO_2$ into reduced and oxidized S products). Negative values from Guaymas Basin samples were attributed to the influence of minor biogenic pyrite that was not significant enough to increase $\Delta^{33}S$ values. Other studies by McDermott (2015) and McDermott et al. (2018) reported $\delta^{34}S$ and $\Delta^{33}S$ values for hydrothermal fluids from Von Damm Vent Field and the Piccard Vent Field located on the Mid-Cayman Rise in order to constrain the hydrothermal fluid sources at the respective sites.

Eickmann et al. (2014) used the multiple S isotope signatures from a barite chimney, in conjunction with strontium and oxygen isotope ratios, to identify low temperature microbial sulfate reduction in the hydrothermal system at Loki's Castle on the Arctic Mid-Ocean Ridge. The study found isotopic signatures in the barite that recorded evidence of microbial sulfate reduction associated with the mixing of hydrothermal fluids and infiltrated seawater. Subsurface mass-dependant microbial sulfate reduction has caused the hydrothermal fluid to become enriched in heavier S isotopes, thereby precipitating barite chimneys with $\delta^{34}S$ and $\Delta^{33}S$ values significantly higher than that of mean seawater. A related study by Jaeschke et al. (2014) studied the multiple S isotope signatures of an extinct barite chimney at Loki's Castle. Sulfur isotope values were similar to that of known seawater samples (Fig. 1.6). This correlation was attributed to the barite having precipitated directly from seawater (Jaeshcke et al., 2014).

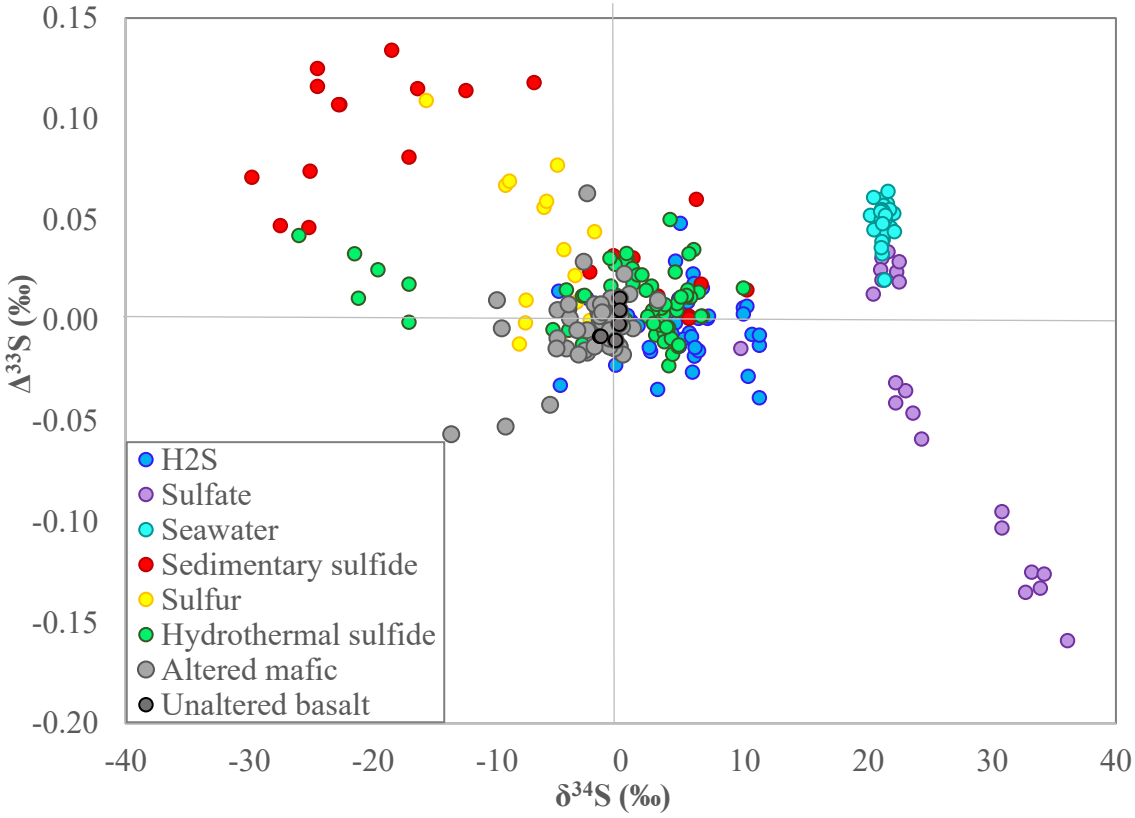


Figure 1.6: Compilation of $\Delta^{33}S$ and $\delta^{34}S$ values from previous multiple S isotope studies of modern mid ocean ridges, including measurements of ambient seawater (data extracted from: Peters et al., 2010; Peters et al., 2011; Eickmann et al., 2014; Jaeschke et al., 2014; Ono et al., 2007; Ono et al., 2012; McDermott, 2015; McDermott et al., 2015; McDermott et al., 2018; Tostevin et al., 2014; Johnston et al., 2014*). All data are expressed using the exponential definition of $\Delta^{33}S$ (defined in Section 2.3), with respect to V-CDT. Data are listed in Appendix A. (*)Johnston et al., (2014) seawater value is an average: uncertainties for averaged data are ±0.15‰ and ±0.006‰ for $\delta^{34}S$ and $\Delta^{33}S$, respectively).

Peters et al. (2010) determined that, due to the $\delta^{34}S$ and $\Delta^{33}S$ range of hydrothermal fluid and sulfide minerals from the southern Mid-Atlantic Ridge (SMAR), increased seawater sulfate reduction was occurring at the SMAR (relative to the East Pacific Rise). Sediment and igneous sulfide mineral bearing samples from Logatchev hydrothermal vent field, which is also located on the Mid-Atlantic Ridge, were analyzed as well. The study recorded elevated $\Delta^{33}S$ values, while $\delta^{34}S$ values varied significantly. Relatively high $\Delta^{33}S$

values were attributed to biogenic sulfate reduction (Peters et al., 2010). Peters et al. (2011) measured the multiple S isotope values of sediments, elemental S, and sulfides from the Palinuro Volcanic Complex, and Panarea hydrothermal field, located in the Tyrrhenian Sea. Multiple S isotope signatures based on $\delta^{34}S$ and $\Delta^{33}S$ were attributed to a biogenic S source.

These previous studies have allowed for interpretation of local processes affecting the multiple S isotope signatures of specific hydrothermal systems, as well as a broader understanding of S mixing and fractionation that is potentially applicable to modern marine hydrothermal systems in general. Results from these previous multiple S isotope studies of seawater, as well as modern seafloor hydrothermal systems, are summarized in Figure 1.6 and Figure 1.7. While these studies provide significant insight into the variety of uses for multiple S isotopes in modern systems as well as a generalized understanding of S isotope reservoirs in most parts of the hydrothermal system (Fig. 1.8), the use of S isotope signatures to constrain fluid/rock and sediment interaction in hydrothermal systems has not yet been fully investigated.

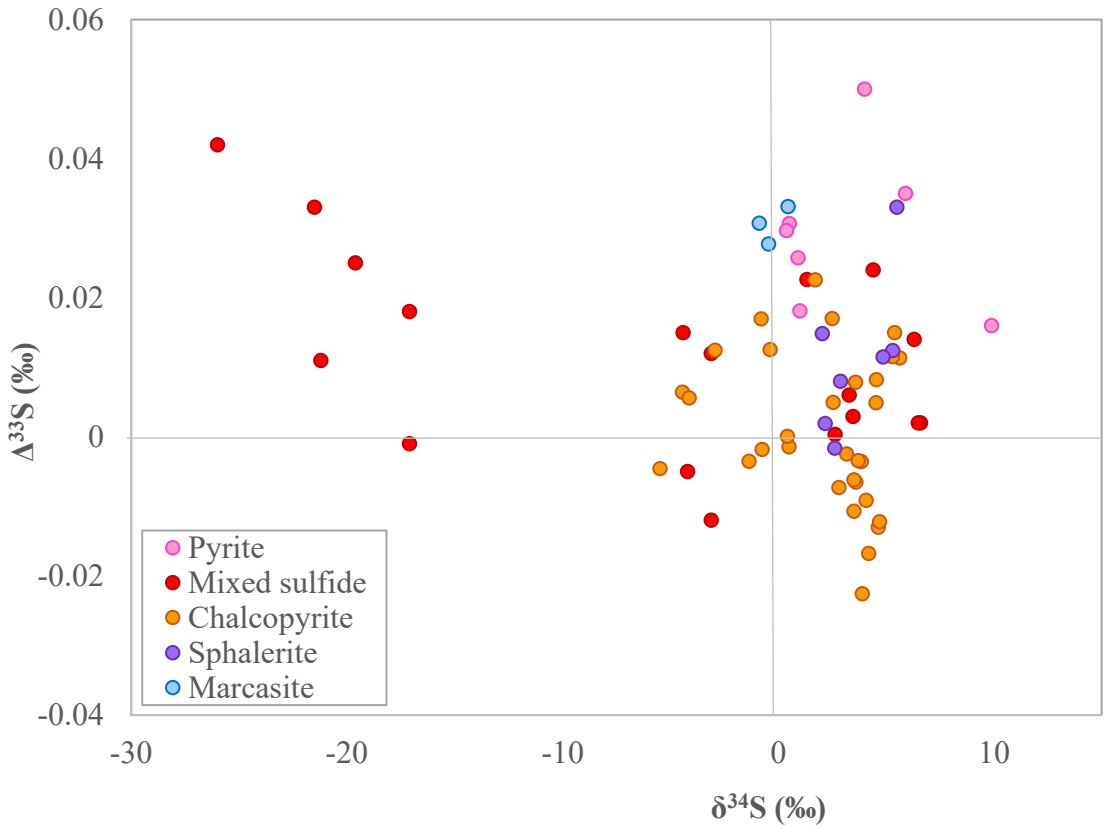


Figure 1.7: Mineralogy of seafloor hydrothermal sulfide samples from previous multiple S isotope studies (Ono et al., 2007; McDermott et al., 2015; Peters et al., 2010; Peters et al., 2011; Eickmann et al., 2014). All data are expressed using the exponential definition of $\Delta^{33}S$ (defined in section 2.3).

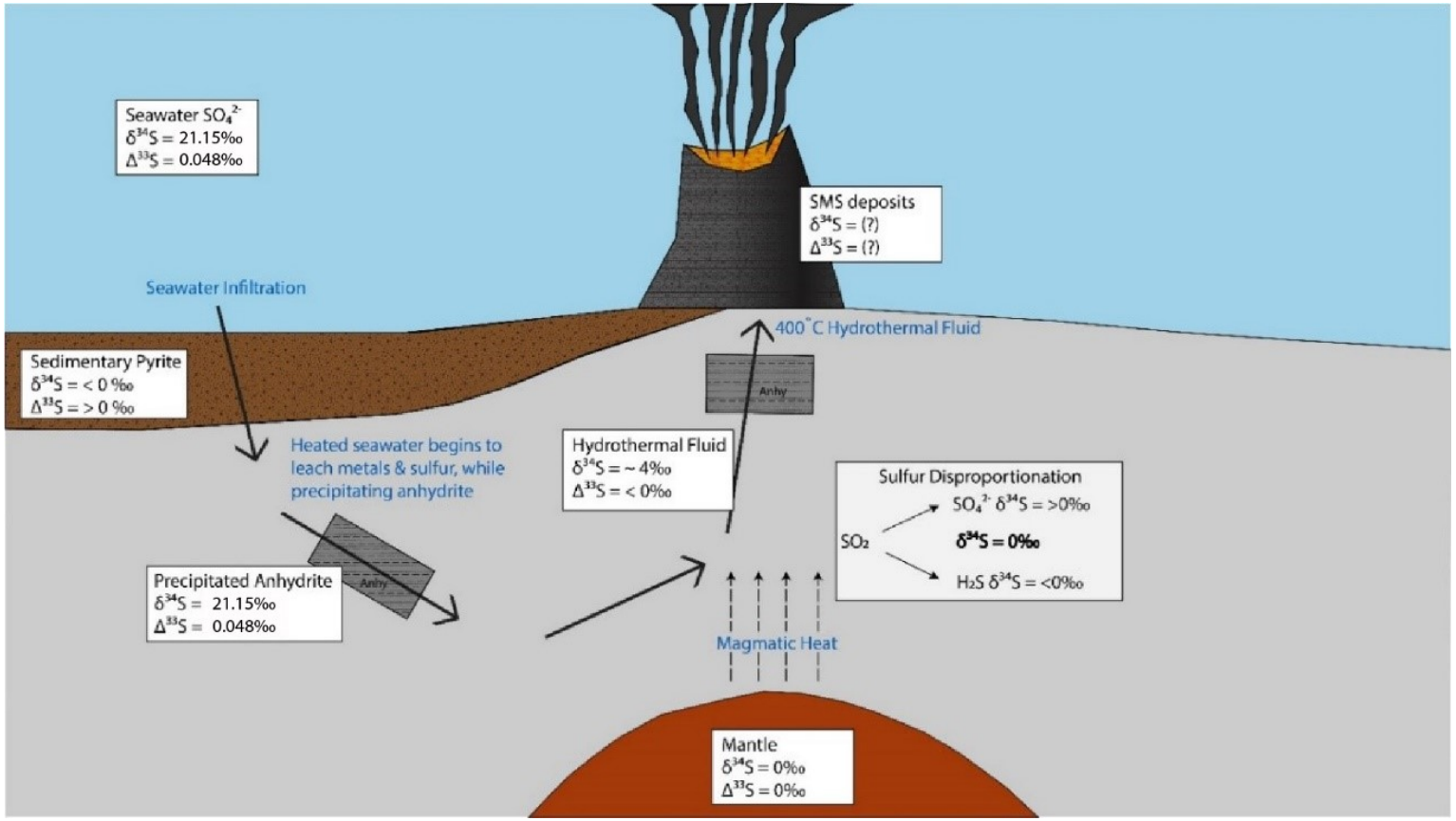


Figure 1.8: A diagram of a typical MOR-hosted hydrothermal vent system showing the processes behind hydrothermal circulation and the averages of S isotope signatures for each part of the system (Modified from Jamieson, 2005; including known parameters from Peters et al., 2010; Peters et al., 2011; Eickmann et al., 2014; Jaeschke et al., 2014; Ono et al., 2007; Ono et al., 2012; McDermott, 2015; McDermott et al., 2015; McDermott et al., 2018; Johnston et al., 2014). All data are expressed using the exponential definition of $\Delta^{33}S$ (defined in section 2.3) in per mil, with respect to V-CDT. Data are listed in Appendix A.

### 1.5.3 Endmember Sulfur Reservoirs and Mixing Components

Hydrothermal circulation at typical MOR-hosted hydrothermal vent systems (Fig. 1.8) involves the infiltration of seawater containing sulfate (oxidized S) through permeable media in the seafloor. If present, microbial sulfate reducers in the subsurface can fractionate infiltrated seawater sulfate thereby producing hydrogen sulfide (reduced S), which can react with iron in the subsurface to form biogenic pyrite. As the fluid continues to infiltrate deeper into the substrate it becomes progressively heated and interacts with wall-rock S. At higher temperatures anhydrite precipitation (~150℃; Elderfield et al., 1999) and thermochemical sulfate reduction (>100℃; Machel et al., 1995) reduce and remove any remaining sulfate in the fluid. When the fluid temperature exceeds ~400°C, the fluid becomes thermally buoyant and is discharged onto the seafloor forming sulfide (reduced S) and sulfate (oxidized s) rich mineral accumulations on the seafloor (SMS deposits).

Disproportionation of $SO_2$ is well-documented at arc and back-arc related environments where the degassing of more silicic (relative to typical MOR basalt), volatile-rich magma bodies upon hydration and cooling to temperatures 400℃ results in speciation of magmatically derived $SO_2$ into isotopically heavy $HSO_4$ and isotopically light $H_2S$ (or $S^0$) relative to the source (Equation 1.5; Equation 1.6) (Holland, 1965; Gamo et al., 1997; Kusakabe et al., 2000; Reeves et al., 2011).

Equation 1.5

$$3SO_2 + 2H_2O = 2HSO_4^- + S^0 + 2H^+$$

Equation 1.6

$$4SO_2 + 4H_2O = 3HSO_4^- + H_2S + 3H^+$$

These various subseafloor fluid/rock interactions that occur during hydrothermal fluid circulation can impact the resultant S isotope signatures of SMS deposits based on the proportion of S that was sourced from each S reservoir that interacts with the hydrothermal system. There are three primary S reservoirs in hydrothermal systems that affect the isotopic values of circulating hydrothermal fluid and associated SMS deposits: igneous basement rocks, biogenic S products (normally associated with sediments), and seawater sulfate. Igneous basement rocks (predominantly basalt and gabbro) have S isotopic values that are inherited from mantle-derived S and thus similar in S composition to meteoritic S (Labidi et al., 2012). Consequently, any S sourced from mafic igneous basement rocks should have near-zero values for both $\delta^{34}S$ and $\Delta^{33}S$, similar to the meteoritic S of the troilite used for data normalization with the CDT scale (Beaudoin et al., 1994). Labidi et al. (2014) reported near zero $\delta^{34}S$ and $\Delta^{33}S$ values for Pacific-Antarctic Ridge basalts, with minor positive $\delta^{34}S$ enrichments of approximately 1‰ that were attributed to relatively isotopically heavy SMS assimilation in later basalt flows. Near zero $\delta^{34}S$ and $\Delta^{33}S$ values from unaltered basalt samples have also been reported by Ono et al. (2012) and Peters et al. (2010).

Lighter isotopes are preferentially metabolised during biogenic processes because bonds fractionated by lighter atomic masses have higher vibrational energy (as opposed to transitional energy), resulting in lower energy requirements to break these bonds (Canfield,

2001). This leads to biogenic S products that are depleted in heavier isotopes ($^{34}S$, $^{36}S$) and enriched in lighter isotopes ($^{32}S$, $^{33}S$) (e.g., Shanks et al., 1995).

Equilibrium MDF results in relationships of ~½ for $\delta^{33}S$ because of the approximately 1 amu difference between $^{32}S$ and $^{33}S$, resulting in a $^{33}\lambda$ value that equals ~0.515 at equilibrium. However, $^{33}\lambda$ can fluctuate (range of ~0.512 to 0.515; Farquhar et al., 2003) for certain processes (e.g., biological processes [Farquhar et al., 2007] and temperature [Johnston, 2011]) leading to non-equilibrium $\Delta^{33}S$ values. For biological processes, such as microbial sulfate reduction, these variations can arise because of different biological pathways for intermediate sulfur species in multi-step metabolic processes (i.e., differences in the material flow network structure, sulfur transfer, and fractionations associated with each step; Farquhar et al., 2003; Johnston et al., 2005; Ono et al., 2006). These processes typically result in less fractionation of $^{33}S$ relative to $^{32}S$ than would be expected for equilibrium fractionation processes, resulting in products with positive $\Delta^{33}S$ that coincide with lower $\delta^{34}S$ values typical for biological fractionations.

A common microbial process that affects S cycling in the ocean environment is microbial sulfate reduction (MSR). Microbial sulfate reduction typically occurs in sediments (e.g., Peters et al., 2010; Peters et al., 2011) where infiltrated seawater sulfate is reduced to biogenic sulfide. Dissimilatory microbial sulfate reduction occurs as follows in Equation 4.3 and Equation 4.4 (Canfield, 2001):

Equation 1.7

$$SO_4^{2-} + 2\,CH_2O \rightarrow H_2S + 2\,HCO_3^-$$

Equation 1.8

$$2H^+ + SO_4^{2-} + 4H_2 \rightarrow H_2S + 4H_2O$$

As a result, seawater sulfate has a well constrained S isotopic value of $\delta^{34}S$=21‰, and a $\Delta^{33}S$=~0.05‰ (Tostevin et al., 2014; Johnston et al., 2014; Jaeshke et al., 2014; Eickmann et al., 2014; Ono et al., 2012). Seawater is a well mixed reservoir for sulfate because of its relatively long residence times in marine environment when compared to overall ocean mixing (Johnston et al., 2014).

# 2. Methodology

## 2.1 Sample and Data Collection

Active hydrothermal vent sites are most commonly discovered through the detection of thermochemical anomalies in the water column caused by hydrothermal plumes. The hot hydrothermal fluid emanating from the hydrothermal vents is thermally buoyant compared to the cold ambient seawater and generates a plume as it rises in the water column and disperses. Conductivity, Temperature, Depth (CTD) sensors (Fig. 2.1), which are oceanographic instruments used to measure conductivity and temperature at depth, are deployed into the water column and used to detect chemical (e.g., $CH_4$, Eh, salinity), temperature and physical (e.g., turbidity) anomalies indicative of hydrothermal plumes (Lonsdale, 1977; Charlou et al., 1993). Once a deposit is located, collection of deposit rock samples typically involves the use of either a remotely operated vehicle (ROV) (Fig. 2.2), or a human operated vehicle (HOV) (Fig. 2.3).

Figure 2.1: A CTD aboard the R/V Kilo Moana, taken during cruise KM-18-12, August 2018 (Photo: Sarah Moriarty).

Figure 2.2: The ROV Jason being recovered after a dive at Endeavour on the Juan de Fuca Ridge during R/V Kilo Moana cruise KM-18-12, August 2018 (Photo: Sarah Moriarty).

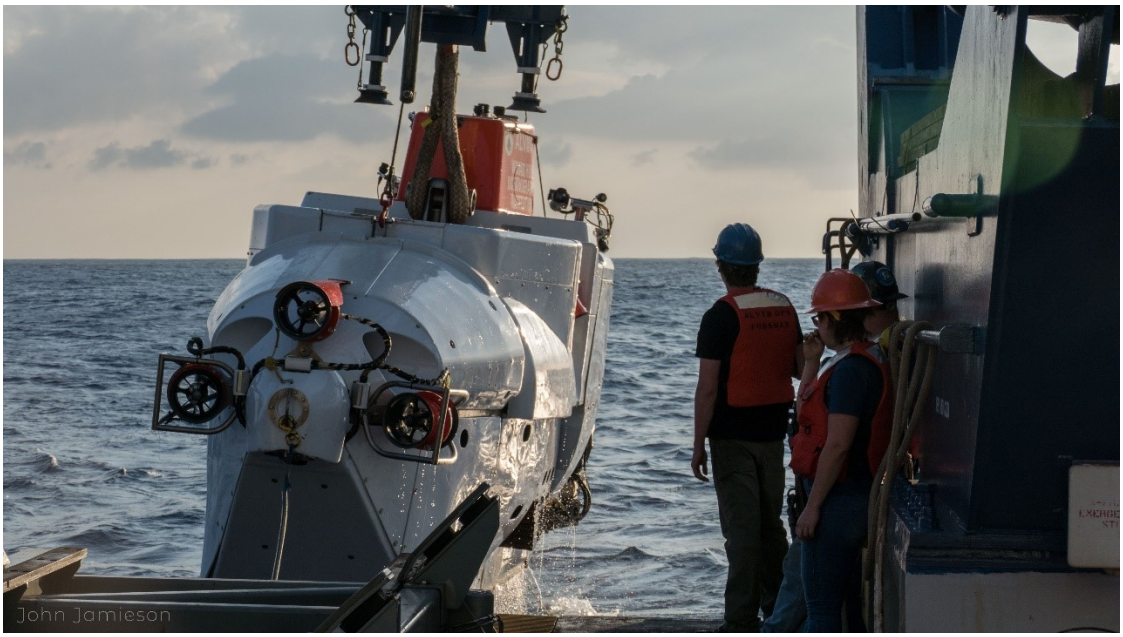


Figure 2.3: The HOV Alvin being recovered after a dive at 9N on the East Pacific Rise during R/V Atlantis cruise AT42-09, April 2019 (Photo: John Jamieson).

These instruments were employed for sample collection during research cruises to the Juan de Fuca Ridge from 2008 – 2018: AT15-36 Atlantis (2008), AT15-47 Atlantis (2009), MBARI Western Flyer (2011), CCGS Tully (2016), and KM1812 Kilo Moana (2018). Samples collected during these research cruises were selected for analysis for this thesis based on both mineralogy (discussed in further detail in section 2.2) and to maximize spatial distribution (Fig. 2.5). Bathymetric data for detailed maps of the study areas were collected using a combination of low-resolution (1-4 km) satellite altimetry, ship-based multibeam sonar (50-100 m resolution), and high resolution autonomous underwater vehicle (AUV) multibeam sonar (1-2 m resolution; Fig. 2.4).


Figure 2.4: Autonomous underwater vehicle (AUV) Sentry on the AT42-21 research cruise to the East Pacific Rise in December, 2019 (Photo: Lauren Dykman).

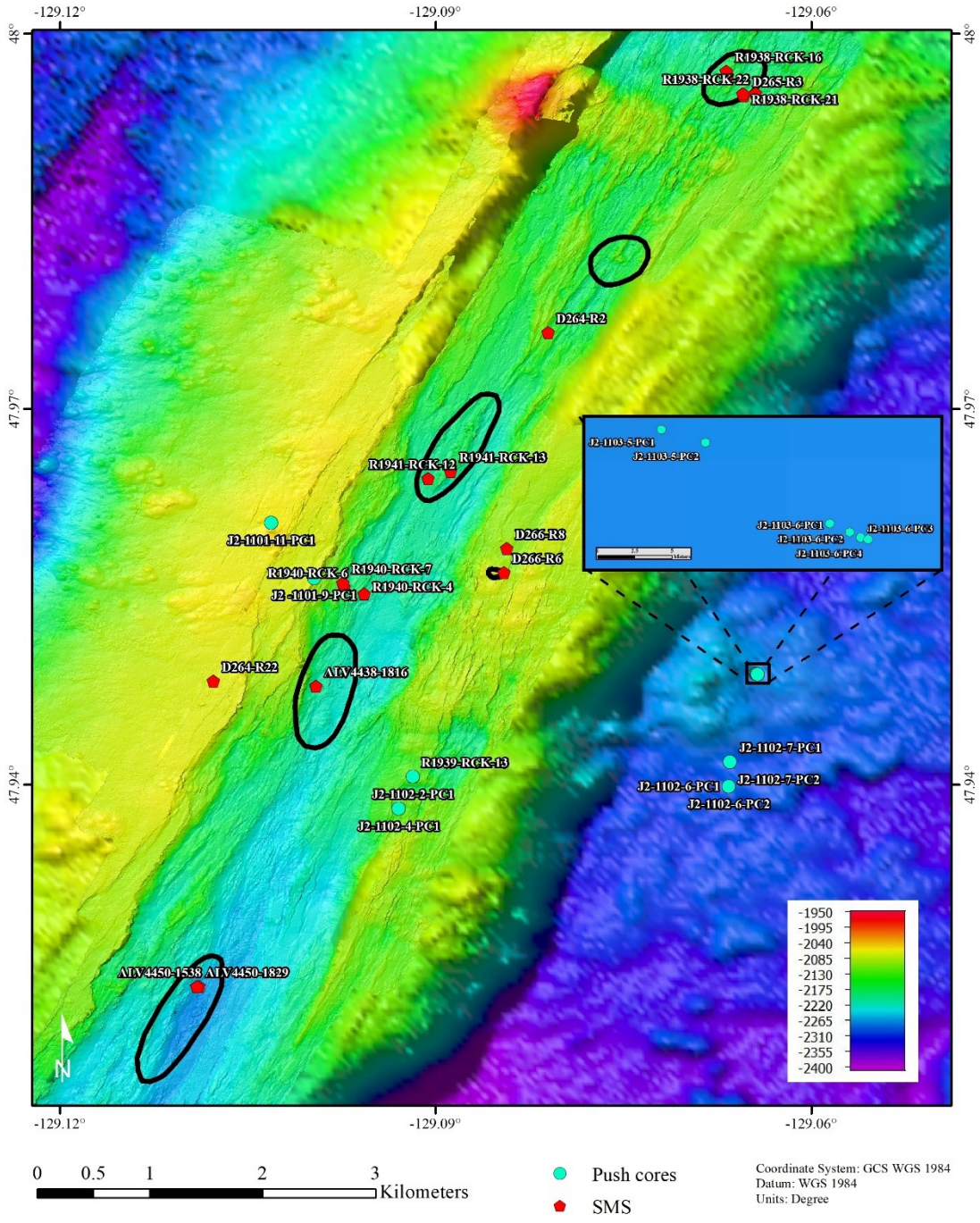


Figure 2.5: Push core and SMS sample locations at Endeavour used for this study. Bathymetry is combination of 2 m autonomous underwater vehicle-derived multibeam sonar bathymetry from Clague and Caress (2015) overlaid on 30 m ship-based multibeam sonar bathymetry from Kelley et al. (2015). Modified from Jamieson et al. (2014).

Fourteen sediment cores were collected during the KM-18-12 research cruise to the Endeavour Segment of the Juan de Fuca Ridge using the ROV Jason in August, 2018 (Fig. 2.6; Table 2.1). Four sediment cores were collected within 1 km of the ridge axis, while the other ten were collected approximately 2 km off axis in order to minimize plume fallout contamination. The cores were immediately placed into a 4˚C refrigerator for temporary storage (< 4 hours) before being measured, photographed, and sectioned. Core dimensions were all 2.5 inches in diameter and varied in length from 4.5 - 11.5 inches. The cores were photographed and measured while still in the core tube. However, due to condensation on the cold cores in the Pacific Northwest climate, core photo quality was very low and limited stratigraphic information can be inferred from them. No method was available on board the research vessel to preserve the stratigraphy of the cores. However, in general, it was attempted to segment the cores in order to separate the upper, oxidized layer; the middle layer containing a redox boundary; and the lower, non-oxidized layer. The segmented core samples were then placed in freezer bags and placed in a -80˚C freezer for the remainder of the cruise, in order to minimize further oxidation. The sediment samples were transported to Memorial University of Newfoundland in a cooler filled with 5 lbs of dry ice. After arrival, the cores were placed into a -18˚C freezer. The push core sub-sections selected for isotopic analysis are listed in Table. 2.1. Further sub-samples were extracted from each selected core sub-section, dried at 50 ˚C for 24 - 48 hours, and then ground into a fine powder using a mortar and pestle. In general, the bottom sections of the cores were selected for analysis as diagenetic pyrite in the sediments, which constitutes the target S-bearing mineral phase for isotopic analyses, would be best preserved below the oxidation boundary.

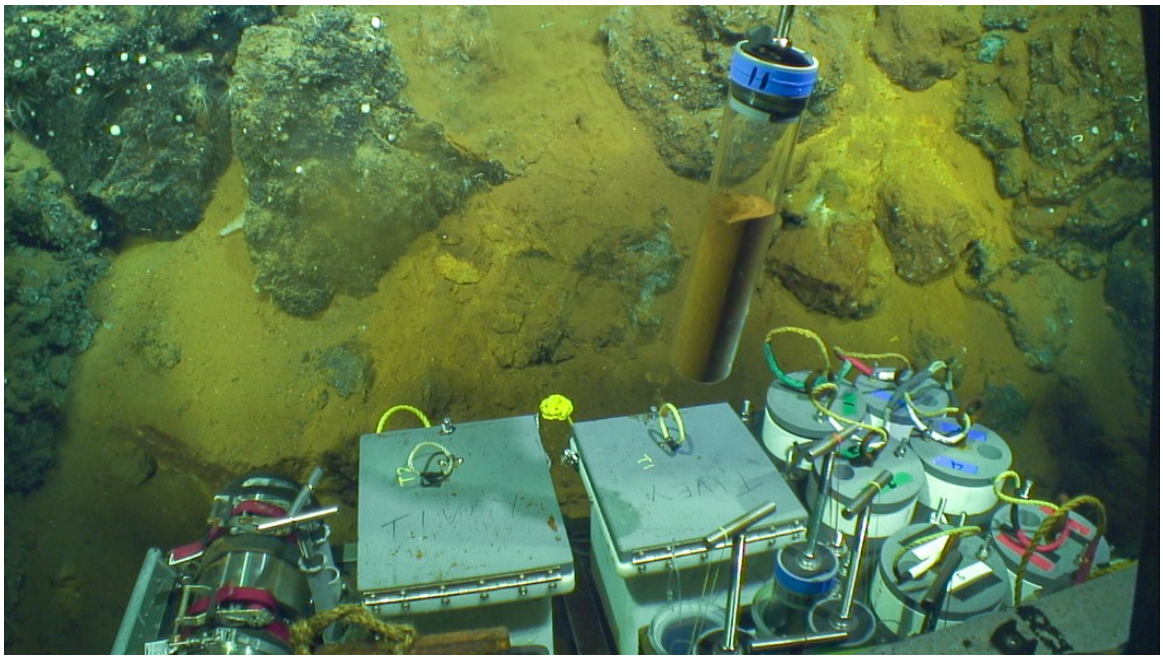

Figure 2.6: The ROV Jason collecting a sediment core at Endeavour on the Juan de Fuca Ridge during R/V Kilo Moana cruise KM-18-12 in August, 2018.

Table 2.1: Core sub-sections selected for isotopic analysis at Harvard University.

| *Push Core* | *Section* | *Depth (cmbsf)* | *Primary Composition* |
|---|---|---|---|
| **J2 -1101-9-PC1** | Bottom | 17-22 | Turbiditic sediments with sand grain sized basalt pyroclasts |
| **J2-1102-2-PC1** | Whole core | 0-15 | Turbiditic sediments and plume fallout |
| **J2-1102-4-PC1** | Top | 0-7 | Turbiditic sediments and plume fallout |
| **J2-1102-4-PC1** | Bottom | 11-16 | Turbiditic sediment and minor oxidized plume fallout |
| **J2-1102-7-PC1** | Bottom | 13-21.5 | Turbiditic sediments |
| **J2-1103-6-PC1** | Bottom | 6-11.5 | Turbiditic sediments |
| **J2-1103-6-PC3** | Bottom | 13-28 | Turbiditic sediments |

## 2.2 Sample Preparation

Different S bearing minerals may have different S isotopic values due to equilibrium fractionation between minerals (Ohmoto, 1972). Therefore, analyzing

monomineralic separates is preferable to bulk rock S isotope analyses, as bulk rock analysis may distort the S isotope signature of a sample because of different relative abundances of S-bearing mineral phases, rather than effects from location-specific hydrothermal fluid cycling. For this study, monomineralic sub-samples included pyrite, pyrrhotite, chalcopyrite, wurtzite, marcasite, barite, and anhydrite. These minerals were physically separated from the whole rock samples under a stereomicroscope using curved fine point forceps. Elemental abundances from previous geochemical analyses completed on the samples were used to confirm visual mineral identifications. For example, barite and anhydrite rarely occur together but are difficult to distinguish in hand samples. The relative abundance of Ba and Ca, as determined from bulk geochemical analyses, helped guide the identification of different mineral phases. Minerals were selected to minimize the abundance of impurities such as minor amounts of silicate, sulfate, mixed sulfide, and iron oxide material in the mineral separates.

While sulfide oxidation at low temperatures typically results in oxidation products with the same $\delta^{34}S$ values as the original sulfide material (Shanks et al., 1995), the effects of post-sampling oxidation on $\delta^{33}S$ values have not yet been investigated. Therefore, samples were placed into baths of a 6.0 M hydrochloric acid (HCl) solution in order to remove the products from post-sampling sulfide oxidation. The minerals were left in the HCl solution for 2 - 24 hours, depending on the level of oxidation, rinsed twice with ethanol, and allowed to dry under ambient room conditions in a fume hood. As a control, a sample showing significant oxidation and a sample showing minimal oxidation were separately placed in the HCl solution for 1 week. After the extended acid bath, both samples showed negligible sulfide decomposition and any previously noted oxidation had

been removed. Final estimated monomineralic sample purities ranged from 80 - 99% based on visual estimates (see appendix for details).

### 2.3 Equations and Definitions

Sulfur isotope ratios are measured relative to the Vienna-Canyon Diablo Troilite (V-CDT) reference scale. This scale utilizes the definition of artificial silver sulfide material IAEA S-1, which has a defined $\delta^{34}S$ value of -0.3‰ (Coplen and Krouse, 1998; Ono et al., 2007). The IAEA S-1 reference does not have a defined $\delta^{33}S$ value and reported $\delta^{33}S$ values vary between labs (for a more detailed explanation of $\delta^{33}S$ values for IAEA S-1, the reader is referred to section 4.1.2.1).

Mass dependent fractionation is defined in Equation 2.1 (Young et al., 2002; Farquhar et al., 2003). Capital delta ($\Delta^{33}S$) notation is expressed using Equation 2.2 (Farquhar et al., 2003; Farquhar and Wing, 2003), and is defined as the deviation of $\delta^{33}S$ (or $\delta^{36}S$) from a standard MDF line (Gao and Thiemens, 1991).

Equation 2.1

$$^{33}\lambda = \ln\left(1 + \frac{\delta^{33}S}{1000}\right) / \ln\left(1 + \frac{\delta^{34}S}{1000}\right)$$

Where $^{33}\lambda$ represents the fractionation relationship between $\delta^{33}S$ and $\delta^{34}S$.

Equation 2.2

$$\Delta^{33}S = \delta^{33}S - \left[\left(\frac{\delta^{34}S}{1000} + 1\right)^{0.515} - 1\right] * 1000\ (‰)$$

Equation 2.2 represents the exponential definition for $\Delta^{33}S$. Here, 0.515 represents $^{33}\lambda$ for equilibrium fractionation processes. Using this fractionation-oriented definition,

the products of equilibrium fractionation processes for which the starting material had a $\Delta^{33}S$ value of 0‰ will have also have a $\Delta^{33}S$ value of 0‰. While the exponential definition is used in this thesis, it is important to note that there are two other definitions for $\Delta^{33}S$ (c.f. Ono et al., 2007; 2012; McDermott et al., 2015). A linear definition for $\Delta^{33}S$ (Equation 2.3) is mass-balance oriented and allows for the linear expression of values during isotope mixing (Ono et al., 2007).

Equation 2.3

$$* \Delta^{33}S = \delta^{33}S - 0.515 \times \delta^{34}S \text{ (‰)}$$

The logarithmic definition (Equation 2.4) allows for the linear expression of values during mass dependent isotope fractionation (Ono et al., 2003; Ono et al. 2006; Ono et al. 2007; Rouxel, 2008).

Equation 2.4

$$' \Delta^{33}S = \left[\ln\left(\frac{\delta^{33}S}{1000} + 1\right) - 0.515 \times \ln\left(\frac{\delta^{34}S}{1000} + 1\right)\right] \times 1000 \text{ (‰)}$$

Both the linear and logarithmic definitions produce nearly indistinguishable values, except where $\delta^{34}S$ values are either highly positive or highly negative (i.e. well beyond natural values recorded from submarine hydrothermal systems; Ono et al., 2003; Ono et al., 2006; Miller, 2002). All non-zero isotopic values in this thesis, including those extracted from scientific papers that report $\Delta^{33}S$ values using either the linear or logarithmic definitions, are presented here using the exponential definition of $\Delta^{33}S$ for simple comparison to previous work by the Johnston and Farquhar labs.

## 2.4 Sulfur Isotope Analysis

Multiple S isotope analysis requires higher instrument precision than traditional S isotope analyses (i.e., combustion and conversion to $SO_2$), due to the relatively low natural abundance of $^{33}S$ and the inherent significance placed on very small differences in isotopic ratios. To achieve this level of precision, gas source mass spectrometry using a ThermoFinnigan MAT 253 mass spectrometer is required (Ono et al., 2006). Gas entering the mass spectrometer is ionized via electron bombardment, causing acceleration of an ion beam along a trajectory, which is then curved by a magnet leading to a mass dependent ion dispersion into Faraday cups allowing for concurrent isotope measurements (Shanks et al., 1995; Ono et al., 2006).

For this project, analyses were performed at two laboratories: The Gas Source Mass Spectrometry I Laboratory at the University of Maryland, College Park (UMD), and the Johnston Laboratory at Harvard University, in Cambridge, MA. Two different laboratories were used because of limited availability at both laboratories, and to investigate procedural and data quality issues associated with early results. Duplicate measurements from both laboratories also allowed for the investigation of inter-laboratory accuracy and challenges associated with defining values for $\Delta^{33}S$ due to the lack of defined value for $\delta^{33}S$ for IAEA S-1. The results presented in this thesis include data from both laboratories.

### 2.4.1 Isotopic analyses at University of Maryland, College Park

Thirty-two mineral separate samples (see Appendix B) were analyzed at UMD in

April – May of 2018. Reduced S content of the monomineralic sulfide samples (pyrite, pyrrhotite, chalcopyrite, wurtzite, and marcasite) was extracted and converted to silver sulfide ($Ag_2S$) using the chromium reduction method described in Canfield et al. (1986), which is specific to chromium reducible S (CRS) and is not affected by sulfate content (Fig. 2.7).

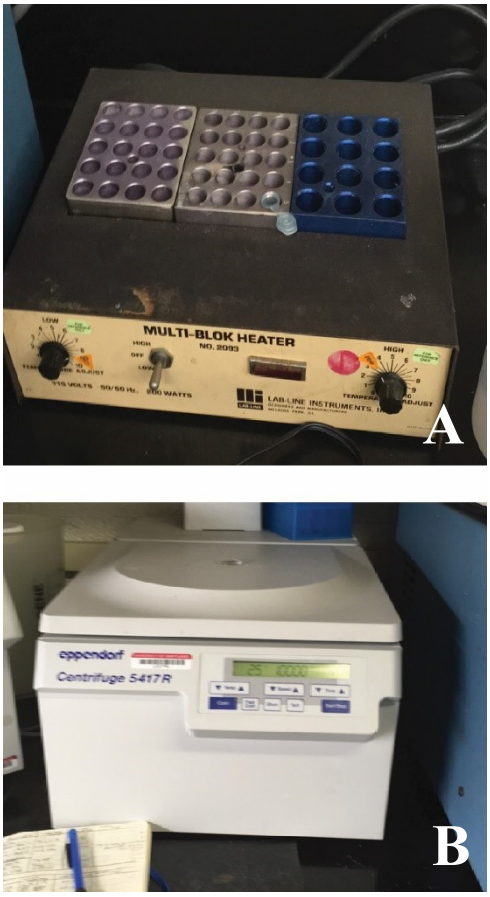


Figure 2.7: Post-CRS reduction filtration and cleaning process at the University of Maryland, College Park: **(A)** Multi-Blok heater used to dry silver sulfide samples overnight. **(B)** Centrifuge machine used to consolidate samples after rinsing with Milli – Q.

The five sulfate (anhydrite and barite) samples were converted using the Thode solution procedure described in Thode et al. (1961) and Forrest and Newman (1977). The

resulting $Ag_2S$ was separated from liquid products using a micropipette, washed six times with Milli-Q while intermittently re-condensing solid material using a centrifuge, and dried overnight in a Multi-Blok heater (Fig. 2.7). The cleaned and dried $Ag_2S$ was then transferred to a fluorination chamber and filled with elemental fluorine gas ($F_2$, Fig. 2.8) and left overnight at 250˚C, resulting in the reaction described in Equation 2.5, and the generation of $SF_6$ gas (Fig. 2.8B).

Equation 2.5

$$Ag_2S + 4F_2 \xrightarrow{yields} 2AgF + SF_6$$

Gas chromatography was used to purify the $SF_6$ by eliminating residual contaminants produced in the fluorination process. The resulting gas was then introduced into a ThermoFinnigan MAT 253 gas source mass spectrometer on duel inlet mode in order to measure the concurrent ionic beams of $^{32}SF_5^+$, $^{33}SF_5^+$, $^{34}SF_5^+$, and $^{36}SF_5^+$, and the corresponding masses: 127, 128, 129, and 131 g/mol, respectively. The isotopic ratios for $^{32}S$, $^{33}S$, $^{34}S$, and $^{36}S$ are initially reported relative to the Canyon Diablo Troilite (CDT) standard, using δ notation. However, all values have been subsequently converted to the V-CDT scale (see section 4.1 for details). Analytical uncertainties are based on repeat analyses of IAEA S-1. Intra-laboratory reproducibility (1σ) is reported as ±0.15‰ and ± 0.008‰ for $\delta^{34}S$ and $\Delta^{33}S$, respectively (Wu et al., 2018).


Figure 2.8: **(A)** The CRS reduction line and **(B)** the fluorination set up at the University of Maryland, College Park.

### 2.4.2 Isotopic analyses at Harvard University

In general, and barring minor procedural differences, S isotope analytical procedures at the Johnston Laboratory were consistent with those at the UMD laboratory. Nineteen samples (see Appendix B) were analyzed at Harvard University in February 2019. Samples analyzed at Harvard that had been previously analyzed at UMD were splits from the same picked material. The CRS reduction method (Fig. 2.9) described in Canfield et al. (1986) and the Thode solution procedure Fig. 2.11A) described in Thode et al. (1961) and Forrest and Newman (1977) were used to convert the samples to zinc sulfide. The first

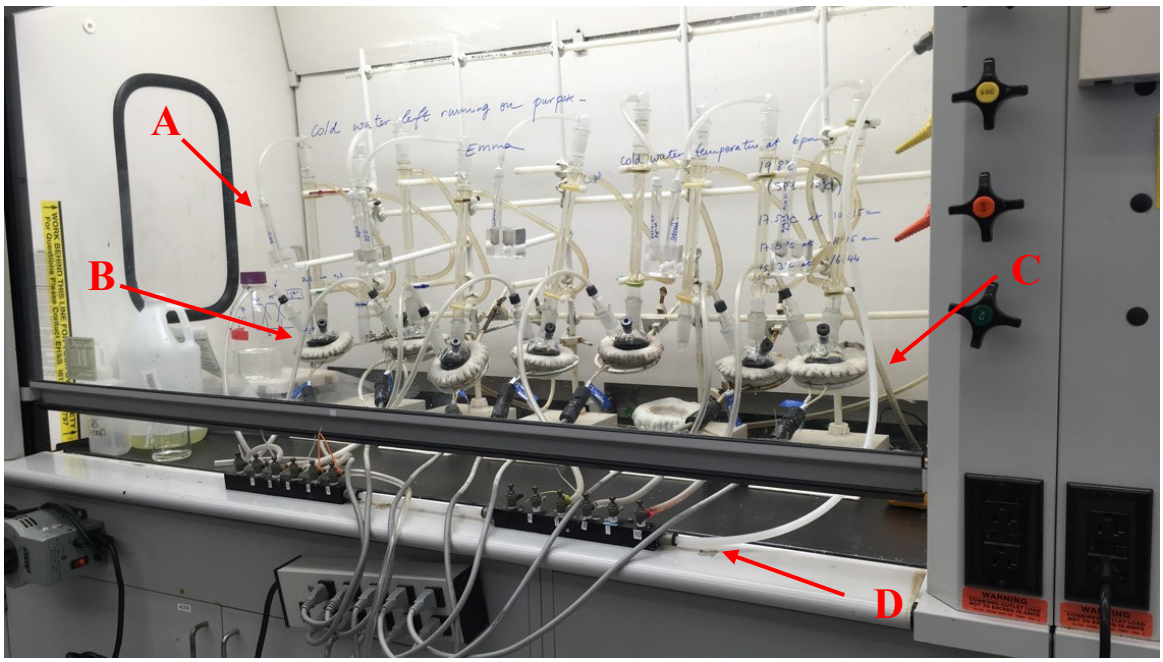


Figure 2.9: The CRS reduction line at Harvard University. **(A)** 15mL zinc acetate solution, **(B)** Round bottom flask placed on a heater set at about 45 ℃. The ground up sample was placed in the round bottom flask, along with 20 mL each of 6 N HCL and CRS solution. **(C)** The cold water line, and **(D)** the $N_2$ line.

round of CRS reductions resulted in extreme reactions that caused the zinc acetate solution to bubble over during zinc sulfide precipitation. During following rounds of CRS reductions, 1 - 2 drops of anti-foaming agent was placed in the zinc acetate solution to prevent material loss. A 0.45 M $AgNO_3$ solution was added to the zinc acetate solution and

precipitate CRS material in order to precipitate silver sulfide.

The filtration technique (Fig. 2.10) at Harvard University varied from the decanting method used at UMD. After the CRS reduction, the zinc acetate solution and resulting precipitate material was run through a filtration column with 0.2 µ x 25 mm nitrate membrane filters. The precipitate material was cleaned by rinsing the column three times with $NH_4O_4$ solution, and intermittently with Milli Q. The cleaned and filtered silver sulfide precipitate material was then dried in a 50℃ oven for four hours and weighed.

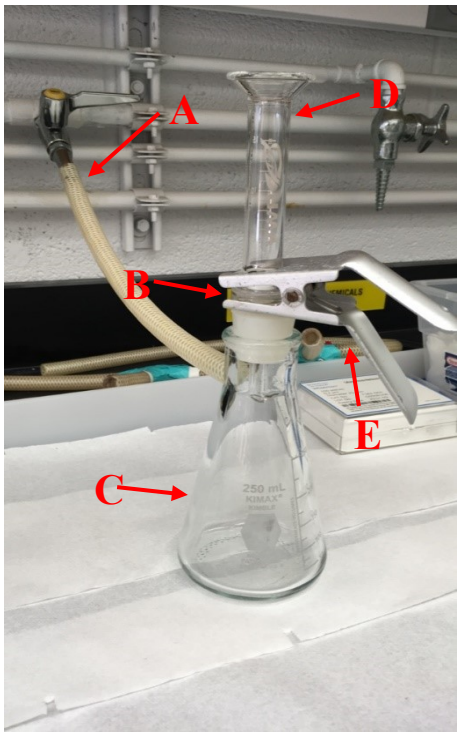


Figure 2.10: The filtration column set up used at Harvard University: **(A)** Vacuum line to encourage faster filtration, **(B)** membrane filter, placed in between filtration flask (with stopper) and filtration column, **(C)** filtration flask, **(D)** filtration column, and **(E)** curved clip holding the set up together.

The silver sulfide material was again converted to $SF_6$. Gas chromatography was again used to purify the $SF_6$ by eliminating residual contaminants used in the fluorination

process. The resulting gas was then introduced into a ThermoFinnigan MAT 253 mass spectrometer (Fig. 2.11B) running on duel inlet mode in order to measure the concurrent ionic beams of $^{32}SF_5^+$, $^{33}SF_5^+$, $^{34}SF_5^+$, and $^{36}SF_5^+$, and the corresponding masses: 127, 128, 129, and 131 g/mol, respectively. The isotopic ratios for $^{32}S$, $^{33}S$, $^{34}S$, and $^{36}S$ are presented with respect to the V-CDT scale, using standard δ notation, in per mil. Calculated analytical uncertainties were determined by repeat analyses of standards IAEA S-1, IAEA S-2, and IAEA S-3 versus the internal reference gas. Intra-laboratory reproducibility (1σ) is reported as ±0.2‰, and ±0.006‰ for $\delta^{34}S$ and $\Delta^{33}S$, respectively (Masterson, 2016).

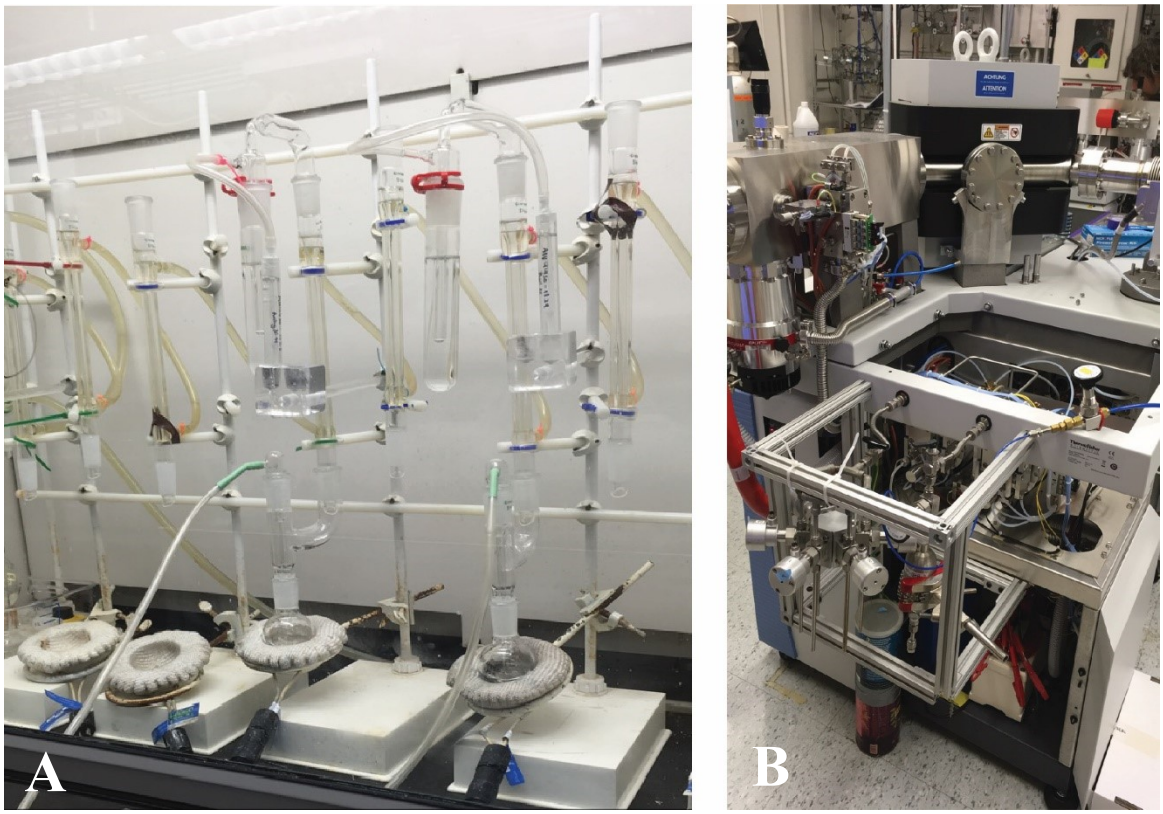


Figure 2.11: **(A)** Thode reduction set up at Harvard University. The heaters placed underneath the round bottom flasks were set at (~ 75 °C) for the Thode reductions **(B)** the Thermofinnigan MAT 253 mass spectrometer used at Harvard University.

# 3. Results

Two independent laboratories were used to collect S isotope data, partly because first analyses from UMD resulted in higher than expected uncertainties. The reduction procedures at UMD resulted in low silver sulfide yields (<50%) for several samples (see appendix B), necessitating repeat CRS reductions. For reference, McDermott et al. (2015) reported CRS and Thode reduction yields above 90% for all samples. Unexpected sample behavior was also reported during fluorination at UMD, potentially related to the low silver sulfide yields. The analytical issues at UMD may have contributed to higher uncertainties in the S isotope ratios (largely the $\delta^{33}S$ values) that were ultimately measured.

Due to laboratory availability, the sediment cores that were collected after the UMD analyses were analysed at Harvard University. In order to ensure interlaboratory reproducibility, several samples (Tables 3.1 and 3.2) that had been analysed at UMD were also brought to Harvard for analysis. All CRS reduction yields at Harvard were relatively high (average of 82%), except for the first round of reductions (see Appendix B). No issues were encountered during the fluorination procedure at Harvard. Accordingly, data are presented from both laboratories separately and then potential analytical sources of the high uncertainty for the UMD samples are considered. The resultant $\Delta^{33}S$ values indicate some interlaboratory bias, with the UMD data set trending more positively and the Harvard data set trending more negatively (Fig 4.1). Offsets in interlaboratory $\Delta^{33}S$ values are inconsistent between corresponding samples analyzed at both laboratories (Fig. 4.2), and therefore cannot be attributed solely to normalization procedures associated with the lack

of defined value for $\delta^{33}S$ for IAEA S-1 reference material.

### 3.1 University of Maryland, College Park

The S isotope values of sulfide samples from Axial Volcano were relatively consistent, ranging from 3.4‰ to 3.9‰ for $\delta^{34}S_{V\text{-}CDT}$ and 0.006‰ to 0.022‰ for $\Delta^{33}S_{V\text{-}CDT}$ (Table 3.1). Sulfide samples from Middle Valley were more isotopically heavy than those from the other two sample locations, with $\delta^{34}S_{V\text{-}CDT}$ values ranging from 6.5‰ to 7.0‰, while $\Delta^{33}S_{V\text{-}CDT}$ values ranged from -0.004‰ to 0.016‰. Endeavour sulfide samples showed more variation than either of the two first described locations, with $\delta^{34}S_{V\text{-}CDT}$ values ranging from 0.1‰ to 4.3‰ and $\Delta^{33}S_{V\text{-}CDT}$ values ranging from -0.020‰ to 0.064‰ (Table 3.1; Fig. 3.1). Despite these variations, Endeavour sulfide samples do not show systematic differences between vent areas (Fig. 3.1). The two High Rise samples, however, had distinctively similar values for both $\delta^{34}S_{V\text{-}CDT}$ (3.8‰ to 4.3‰) and $\Delta^{33}S_{V\text{-}CDT}$ (0.005‰ to 0.014‰).

Table 3.1: Results of multiple S isotope analyses conducted on JdFR S bearing minerals separates in April-May 2018 at UMD.

| *Sample* | *Mineral* | *JdFR Segment* | *Vent Area* | $\delta^{34}S$ (‰) CDT | $\Delta^{33}S$ (‰) CDT | $\delta^{34}S$ (‰) V-CDT | $\Delta^{33}S$ (‰) V-CDT |
|---|---|---|---|---|---|---|---|
| **R1940-RCK8** | Py | Endeavour | MEF | 3.3 | 0.029 | 3.4 | 0.006 |
| **R1940-RCK6** | Py | Endeavour | MEF | 3.4 | 0.034 | 3.5 | 0.012 |
| **R1940-RCK 4** | Py | Endeavour | MEF | 2.2 | 0.015 | 2.3 | -0.007 |
| **R1940-RCK7** | Py | Endeavour | MEF | 4.0 | 0.010 | 4.1 | -0.013 |
| **R1941 RCK12** | Py | Endeavour | High Rise | 4.2 | 0.036 | 4.3 | 0.014 |
| **D264-R2** | Py | Endeavour | Salty Dawg | 3.0 | 0.023 | 3.1 | 0.000 |
| **D266-R8** | Py | Endeavour | Zephyr Mound | 4.2 | 0.002 | 4.3 | -0.020 |
| **D266-R6** | Py | Endeavour | Zephyr Mound | 3.6 | 0.087 | 3.7 | 0.064 |
| **R1938-RCK21** | Py | Endeavour | Sasquatch | 3.5 | 0.041 | 3.6 | 0.019 |
| **R1938-RCK16** | Py | Endeavour | Sasquatch | 2.4 | 0.019 | 2.5 | -0.003 |
| **R1939-RCK13** | Mrc | Endeavour | MEF | 0.0 | 0.055 | 0.1 | 0.033 |
| **R1939-RCK 14** | CuPy | Endeavour | MEF | 3.8 | 0.022 | 1.9 | -0.001 |
| **ALV4438-1816** | CuPy | Endeavour | MEF | 2.0 | 0.023 | 3.9 | 0.003 |
| **D266-R6** | CuPy | Endeavour | Zephyr Mound | 2.7 | 0.014 | 2.8 | -0.008 |
| **R1941-RCK12** | CuPy | Endeavour | High Rise | 3.7 | 0.028 | 3.8 | 0.005 |
| **D264-R22** | Barite | Endeavour | MEF | 21.3 | 0.053 | 21.4 | 0.031 |
| **ALV4450-1829** | Barite | Endeavour | Mothra | 20.9 | 0.068 | 21.0 | 0.045 |
| **ALV4450-1538** | Anhy | Endeavour | Mothra | 20.9 | 0.053 | 21.0 | 0.031 |
| **ALV4451-1725** | Anhy | Endeavour | Sasquatch | 18.7 | 0.068 | 18.8 | 0.045 |
| **ALV4451-1725** | Wz | Endeavour | Sasquatch | 2.0 | 0.031 | 2.1 | 0.008 |
| **R1938-RCK22** | Po | Endeavour | Sasquatch | 2.8 | 0.004 | 2.9 | -0.018 |
| **D264-R2** | Po | Endeavour | Salty Dawg | 2.4 | 0.016 | 2.5 | -0.007 |
| **D265-R3** | MgPy | Endeavour | Sasquatch | 3.4 | 0.053 | 3.5 | 0.030 |
| **ALV4449-1938** | Po | Endeavour | MEF | 1.4 | 0.044 | 1.5 | 0.021 |
| **R1942-RCK10** | Po | Middle Valley | Bent Hill | 6.4 | 0.018 | 6.5 | -0.004 |

Table 3.1 continued..

| *Sample* | *Mineral* | *JdFR Segment* | *Vent Area* | $\delta^{34}S$ (‰) **CDT** | $\Delta^{33}S$ (‰) **CDT** | $\delta^{34}S$ (‰) **V-CDT** | $\Delta^{33}S$ (‰) **V-CDT** |
|---|---|---|---|---|---|---|---|
| **R1942-RCK8** | Po | Middle Valley | Bent Hill | 6.7 | 0.039 | 6.8 | 0.016 |
| **R1942-RCK16** | Po | Middle Valley | Bent Hill | 6.9 | 0.025 | 7.0 | 0.002 |
| **ALV4522-1748** | Po | Axial Volcano | International District | 3.8 | 0.045 | 3.9 | 0.022 |
| **ALV4522-1748** | Anhy | Axial Volcano | International District | 20.2 | 0.064 | 20.3 | 0.041 |
| **ALV4522-1748** | CuPy | Axial Volcano | International District | 3.3 | 0.028 | 3.4 | 0.006 |

The single marcasite sample from Endeavour has a near zero $\delta^{34}S_{V\text{-}CDT}$ value (Fig. 3.1), which is consistent with marcasite values reported in Ono et al. (2007; Fig. 1.7). The pyrrhotite S isotope signatures vary significantly, with $\delta^{34}S_{V\text{-}CDT}$ values ranging from 1.5‰ to 7.0‰ and $\Delta^{33}S_{V\text{-}CDT}$ ranging from -0.018‰ to 0.022‰. The pyrite S isotope signatures show little variance in $\delta^{34}S_{V\text{-}CDT}$, with values ranging from 2.3‰ to 4.3‰. However, for $\Delta^{33}S_{V\text{-}CDT}$, the pyrite samples are similar in variation to pyrrhotite, with values ranging from -0.013‰ to 0.064‰. The chalcopyrite $\delta^{34}S_{V\text{-}CDT}$ values show little variance, ranging from 1.9‰ to 3.9‰, while $\Delta^{33}S_{V\text{-}CDT}$ range from -0.008‰ to 0.005‰. The S isotope ratios of the sulfate samples (both anhydrite and barite) have relatively consistent $\delta^{34}S_{V\text{-}CDT}$ values ranging from 18.8‰ to 21.4‰. The $\Delta^{33}S_{V\text{-}CDT}$ values for the sulfate samples ranged from 0.031‰ to 0.045‰. Overall, the S isotope results for the sulfide and sulfate minerals determined at UMD are generally consistent with results for these phases reported in previous studies of modern marine hydrothermal systems (Fig. 1.6).

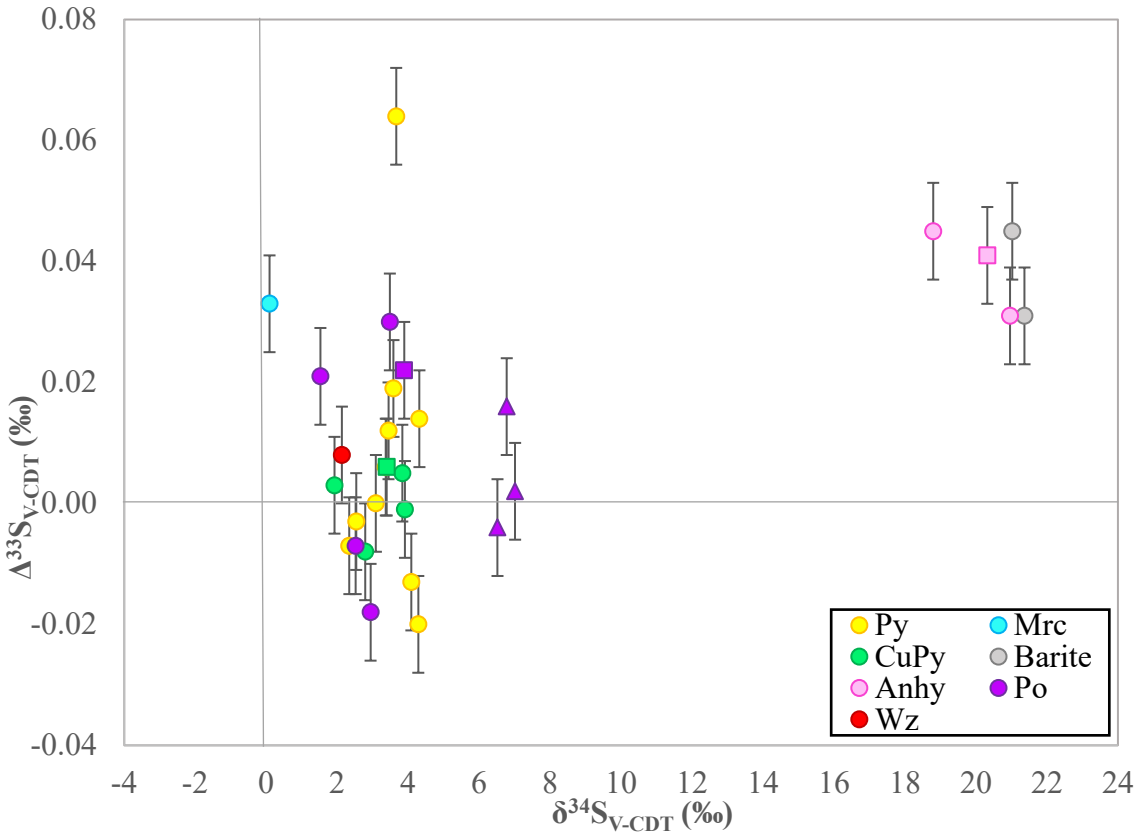


Figure 3.1: University of Maryland S isotope values shown by mineralogy. Middle Valley samples are denoted by triangles, Axial samples by squares, and Endeavour samples by circles. All data are expressed using the exponential definition of $\Delta^{33}S$. Error bars are 1σ. For $\delta^{34}S$, error bars are smaller than the symbols used.

### 3.2 Harvard University

Sulfur isotope values (all reported with respect to V-CDT) of sulfide samples from Axial Volcano ranged from 3.2‰ to 4.6‰ for $\delta^{34}S$, and -0.015‰ to -0.058‰ for $\Delta^{33}S$ (Table 3.2). Middle Valley sulfide samples were more isotopically heavy with respect to $\delta^{34}S$ and negative with respect to $\Delta^{33}S$ than those from the other two sample locations, ranging from 6.5‰ to 7.2‰ for $\delta^{34}S$, and -0.034‰ to -0.139‰ for $\Delta^{33}S$. Endeavour sulfide samples varied significantly, ranging from 0.4‰ to 5.4‰ for $\delta^{34}S$, and -0.003‰ to -

0.054‰ for $\Delta^{33}S$. The two Zephyr Mound samples were more negative with respect to $\Delta^{33}S$ than the rest of the sulfide samples from Endeavour, which ranged from -0.051‰ to -0.054‰ (Fig. 3.2). Three samples from the MEF area (ALV4438-1816, R1940-RCK4, and R1940-RCK6) had consistent values for both $\delta^{34}S$ and $\Delta^{33}S$, likely indicative of the same subseafloor hydrothermal fluid source ($\delta^{34}S$ average: 3.7‰, standard deviation: 0.4‰; $\Delta^{33}S$ average: -0.034‰, standard deviation: 0.001‰).

Pyrite values ranged from 3.2‰ to 6.2‰ for $\delta^{34}S$ and -0.005‰ to -0.054‰ for $\Delta^{33}S$ (Fig. 3.2). The pyrrhotite values ranged from 4.7‰ to 7.5‰ for $\delta^{34}S$, more isotopically heavy than the pyrite. The pyrrhotite $\Delta^{33}S$ values showed higher variability compared to other mineral types, from -0.014‰ to -0.139‰. The marcasite sample (Fig. 3.2) had near zero values for both $\delta^{34}S$ (0.4‰) and $\Delta^{33}S$ (-0.003‰), consistent with values from Ono et al. (2007; Fig. 1.7). The chalcopyrite samples ranged from 3.1‰ to 4.6‰ for $\delta^{34}S$, and from -0.032‰ to -0.058‰ for $\Delta^{33}S$.

Of the seven sediment core samples taken to Harvard University for S isotope analysis (Table 2.1), only two yielded enough silver sulfide during the CRS procedure to produce reliable multiple S isotope data: J2-1102-2-PC1-WC and J2-1101-9-PC1-B (Table 3.2). Of these two sediment samples from Endeavour, the sample containing hydrothermal plume fallout yielded a similar isotopic signature (i.e., $\delta^{34}S$ and $\Delta^{33}S$ values) to the other hydrothermal sulfide samples ($\delta^{34}S$: 3.6‰; $\Delta^{33}S$: -0.011‰) (Fig. 3.2), while a sample containing significant pyroclastic material yielded a negative $\delta^{34}S$ value. The sulfate sample from Endeavour was enriched in $^{34}S$ ($\delta^{34}S$: 22.2‰) and had a positive $\Delta^{33}S$ value ($\Delta^{33}S$: 0.016‰), similar to that of seawater (Johnston et al., 2014; Tostevin et al., 2014).

All sample values were within the range of values reported for modern seafloor hydrothermal systems (Fig. 1.6).

Table 3.2: Results of multiple S isotope analyses conducted on JdFR sulfides and sediments in February-March 2019 at Harvard University. All results are reported using the V-CDT scale.

| *Sample* | *Mineral / Type* | *JdFR Segment* | *Vent Area* | $\delta^{34}S$ (‰) $_{V\text{-}CDT}$ | $\Delta^{33}S$ (‰) $_{V\text{-}CDT}$ |
|---|---|---|---|---|---|
| **R1942-RCK8** | Po | Middle Valley | Bent Hill | 7.5 | -0.139 |
| **R1938-RCK22** | Po | Endeavour | Sasquatch | 4.7 | -0.014 |
| **D264-R2** | Py | Endeavour | Salty Dawg | 4.2 | -0.005 |
| **R1941-RCK13** | Py | Endeavour | High Rise | 4.9 | -0.008 |
| **D266-R8** | Py | Endeavour | Zephyr Mound | 5.4 | -0.051 |
| **R1942-RCK10** | Py | Middle Valley | Bent Hill | 6.2 | -0.054 |
| **R1941-RCK12** | Py | Endeavour | High Rise | 4.4 | -0.037 |
| **ALV4451-1725** | Wz | Endeavour | Sasquatch | 2.8 | -0.015 |
| **ALV4438-1816** | CuPy | Endeavour | MEF | 4.1 | -0.032 |
| **R1940-RCK7** | Py | Endeavour | MEF | 5.2 | -0.005 |
| **R1940-RCK4** | Py | Endeavour | MEF | 3.2 | -0.035 |
| **ALV4522-1748** | CuPy | Axial Volcano | International District | 4.6 | -0.058 |
| **R1939-RCK13** | Mrc | Endeavour | MEF | 0.4 | -0.003 |
| **R1940-RCK6** | Py | Endeavour | MEF | 3.8 | -0.035 |
| **D266-R6** | CuPy+Cov | Endeavour | Zephyr Mound | 3.1 | -0.054 |
| **J2-1102-2-PC1-WC** | Sediment | Endeavour | near ridge | 3.6 | -0.011 |
| **J2-1101-9-PC1-B** | Sediment | Endeavour | near ridge | -2.1 | 0.020 |
| **R1942-RCK16** | Po | Middle Valley | Bent Hill | 7.5 | -0.034 |
| **D265-R3** | MgPy | Endeavour | Sasquatch | 4.8 | -0.043 |
| **ALV4522-1725** | Py | Axial Volcano | International District | 3.2 | -0.017 |
| **ALV4450-1538** | Anhy | Endeavour | Mothra | 22.2 | 0.016 |

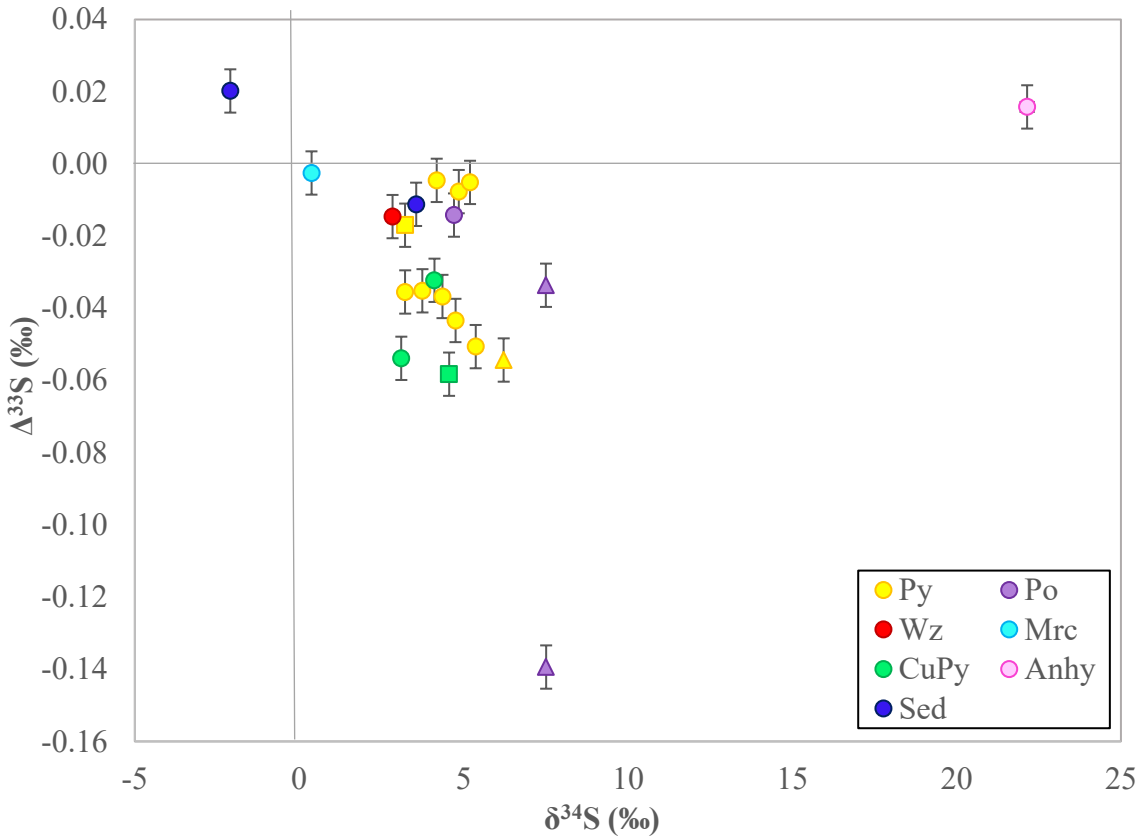


Figure 3.2: Harvard University S isotope values shown by mineralogy. Middle Valley samples are denoted by triangles, Axial samples by squares, and Endeavour samples by circles. All data are expressed using the exponential definition of $\Delta^{33}S$. 1σ error bars are used for both $\delta^{34}S$ and $\Delta^{33}S$. For $\delta^{34}S$, error bars are smaller than the symbols used. All values reported using the V-CDT scale.

# 4. Discussion

## 4.1 Inter-laboratory Comparison

All data from UMD were initially reported using the CDT as opposed to the V-CDT scale. A discrepancy in the data normalized to each scale for $\Delta^{33}S$ that fell outside analytical uncertainties was found for the same samples measured at both laboratories. This inter-laboratory discrepancy necessitated a review of the reference materials used in

S isotope normalization, and the influences of the different normalization scales on the data.

### 4.1.1 V-CDT vs. CDT

The Canyon Diablo Troilite (CDT) scale, a S isotope reference scale based on the S isotope value of troilite (FeS) from the Canyon Diablo meteorite, was formerly the accepted standard used for referencing S isotopes. However, the CDT was found to be isotopically heterogeneous, with a measured range of $\delta^{34}S$ values of 0.4‰ that were well outside the analytical uncertainty of 0.05‰ using $SF_6$ (Beaudoin et al., 1994; Krouse and Coplen, 1998). For $\Delta^{33}S$ values for CDT, Ono et al. (2006), and references therein, reported averaged inter-laboratory measurements that ranged from -0.10 to -0.13‰. At UMD, a value of -0.091‰ is used (Wu et al., 2018). The need to establish a new, internationally accepted, reference scale in favour of the CDT scale was recognized by the International Atomic Energy Agency (IAEA) and the International Union of Pure and Applied Chemistry (IUPAC). Both organizations supported the establishment of the Vienna-Canyon Diablo Troilite (V-CDT) scale, to improve inter-laboratory precision. The V-CDT scale is based upon a synthetic silver sulfide reference material (IAEA S-1) with a defined $\delta^{34}S$ value of -0.3‰ for easy conversion between CDT and V-CDT (Coplen and Krouse, 1998).

As of 1998, it was recommended that, for all S isotope analyses, researchers should cease utilizing the CDT scale in favour of the more homogenous V-CDT scale (Coplen and Krouse, 1998). However, unlike the older CDT, the V-CDT does not have a defined value for $\delta^{33}S$. Since $\Delta^{33}S$ values are essentially the deviation from a standard mass

dependent fractionation line between $\delta^{34}S$ and $\delta^{33}S$, differences in measured $\delta^{34}S$ and $\delta^{33}S$ values between laboratories could contribute to the offsets in resultant $\Delta^{33}S$ values. As a result of the lack of a defined value for $\delta^{33}S$, thus also $\Delta^{33}S$, for IAEA S-1, the capacity for inter-laboratory normalization and comparison is much more challenging.

The two different laboratories utilized in this thesis report results using two different S isotope scales: the Harvard lab uses V-CDT while UMD reports S isotope values with respect to CDT. To standardize samples, while the UMD lab uses the internationally accepted standard IAEA S-1 alongside unknown samples to assure precision, and then reports the unknown values with respect to the long-term average of the inhouse sample of CDT ($\delta^{34}S$ value of about -0.4‰; $\Delta^{33}S$ value of -0.091‰ [Antonelli et al., 2014; Wu et al., 2018]). The use of multiple standards increases internal reproducibility of samples measured at UMD (Wu et al., 2018), which is advantageous for intralaboratory analyses. However, different labs utilizing CDT will produce different results due to the samples heterogeneity, which reduces external reproducibility of S isotope ratios measured at UMD (Antonelli et al., 2014). Very limited data are available on the homogeneity of $^{33}S/^{32}S$ in the CDT and all previous analyses of $\Delta^{33}S$ and $\Delta^{36}S$ in modern samples have generally utilized the V-CDT scale (with the exception of Labidi, et al. [2012] and Labidi et al. [2014]). Due to the known heterogeneity of CDT and most S isotope studies of modern hydrothermal systems using the V-CDT scale, the latter is preferred for this thesis. Thus, a means of converting the UMD data from the CDT to V-CDT scale is needed to facilitate inter-laboratory data comparison and full interpretation of all samples together.

### 4.1.2 Data Normalization

To facilitate inter-laboratory comparisons between the Harvard and UMD data, the UMD data set was converted from the CDT scale (where $\delta^{33}S$ and $\delta^{34}S$ are defined by UMD as -0.09‰ and -0.40‰, respectively [Wu et al., 2018; Antonelli et al., 2014]) to the V-CDT scale as defined in Wing and Farquhar (2015), where $\delta^{33}S$ and $\delta^{34}S$ are equal to -0.061‰ and -0.30‰, respectively (Table 4.1).

Table 4.1: Current values of IAEA S-1 reported for each laboratory in this thesis (Masterson et al., 2016; Masterson, 2016; Wing and Farquhar, 2015; Antonelli et al., 2014; Wu et al., 2018).

| *Institution* | *Scale* | *IAEA S-1* $\delta^{33}S$ (‰) | *IAEA S-1* $\delta^{34}S$ (‰) |
|---|---|---|---|
| **UMD** | CDT | -0.091 | -0.40 |
| **UMD** | V-CDT | -0.061 | -0.30 |
| **Harvard** | V-CDT | -0.04751 | -0.30 |

The conversion is described in Equation 4.1, where $R_x$ is the isotope ratio ($^{34}S/^{32}S$; but is also applicable for $^{33}S/^{32}S$) of the sample. Isotope ratios are related to $\delta^{34}S$ values using Equation 1.1 rearranged and substituted directly (Equation 4.2).

Equation 4.1

$$\left(\frac{R_x}{R_{CDT}}\right) * \left(\frac{R_{CDT}}{R_{S-1}}\right) * \left(\frac{R_{S-1}}{R_{V-CDT}}\right) = \left(\frac{R_x}{R_{V-CDT}}\right)$$

Equation 4.2

$$\frac{\delta\,^{34}S}{1000} + 1 = \frac{^{34}R_{Sample}}{^{34}R_{V-CDT}}$$

Renormalizing the UMD data to the V-CDT scale via the above normalization resulted in a consistent downward shift in $\Delta^{33}S$ (Fig. 4.1), bringing some of the UMD data

points within 1σ analytical uncertainty of the Harvard data set. However, many of the samples analyzed at both laboratories were still not within the same uncertainty for both $\Delta^{33}S$ and $\delta^{34}S$ post normalization to the V-CDT scale and there remains a clear bias in datasets with respect to $\Delta^{33}S$, with the Harvard data systematically ~-0.04‰. (Fig. 4.2).

The source of the remaining post-normalization inter-laboratory discrepancy is unclear. Due to the analytical issues experienced during sample processing at UMD (e.g., poor CRS recovery and complications during fluorination) the Harvard data set is favoured for this thesis. The UMD data are nonetheless useful for identifying potential outliers in the Harvard data (i.e., when S isotope ratios for the same sample deviate significantly between both data sets). As such, the UMD data are used only for reference and all further modelling and interpretation uses only the Harvard data. Although the absolute $\Delta^{33}S$ values between the two datasets are shifted relative to each other, the interpretation of the data does not significantly change if one data set is used instead of the other.

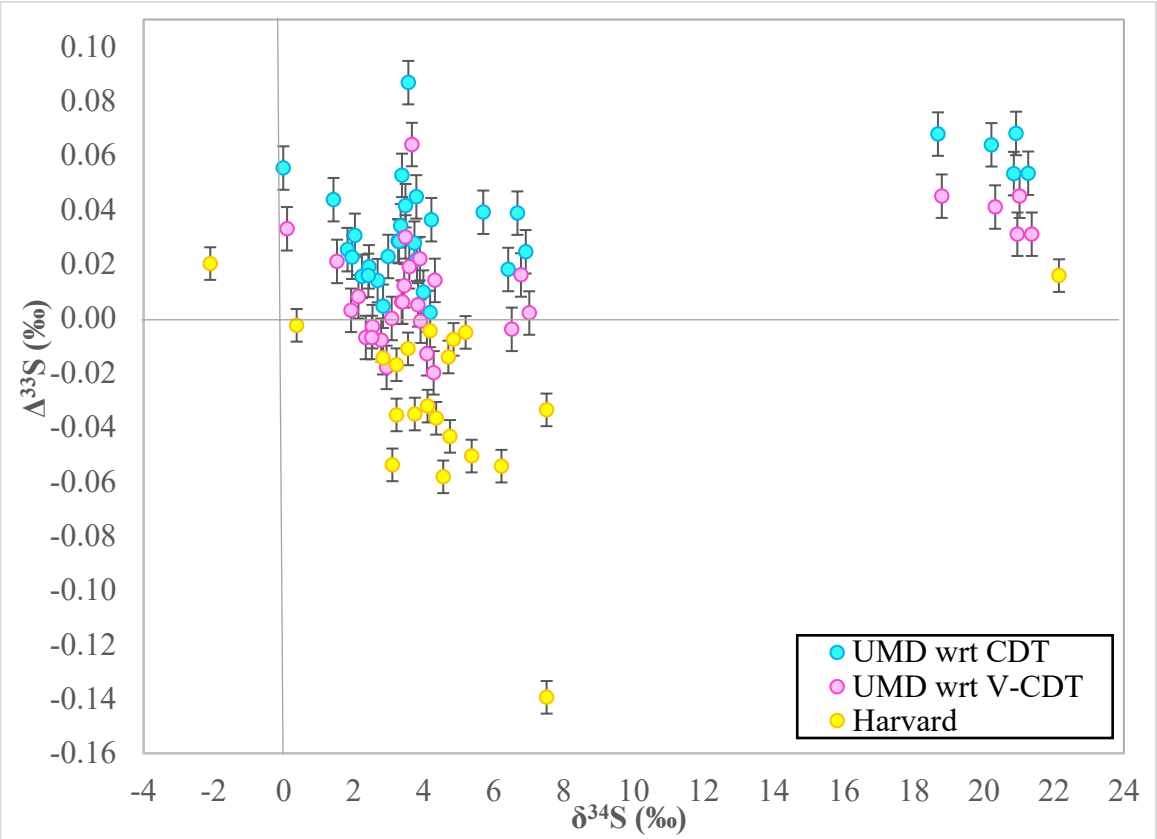


Figure 4.1: UMD values shown with respect to CDT and V-CDT, with the Harvard data set for comparison. All data are expressed using the exponential definition of $\Delta^{33}S$. Error bars are 1σ. For $\delta^{34}S$, error bars are smaller than the symbols used.

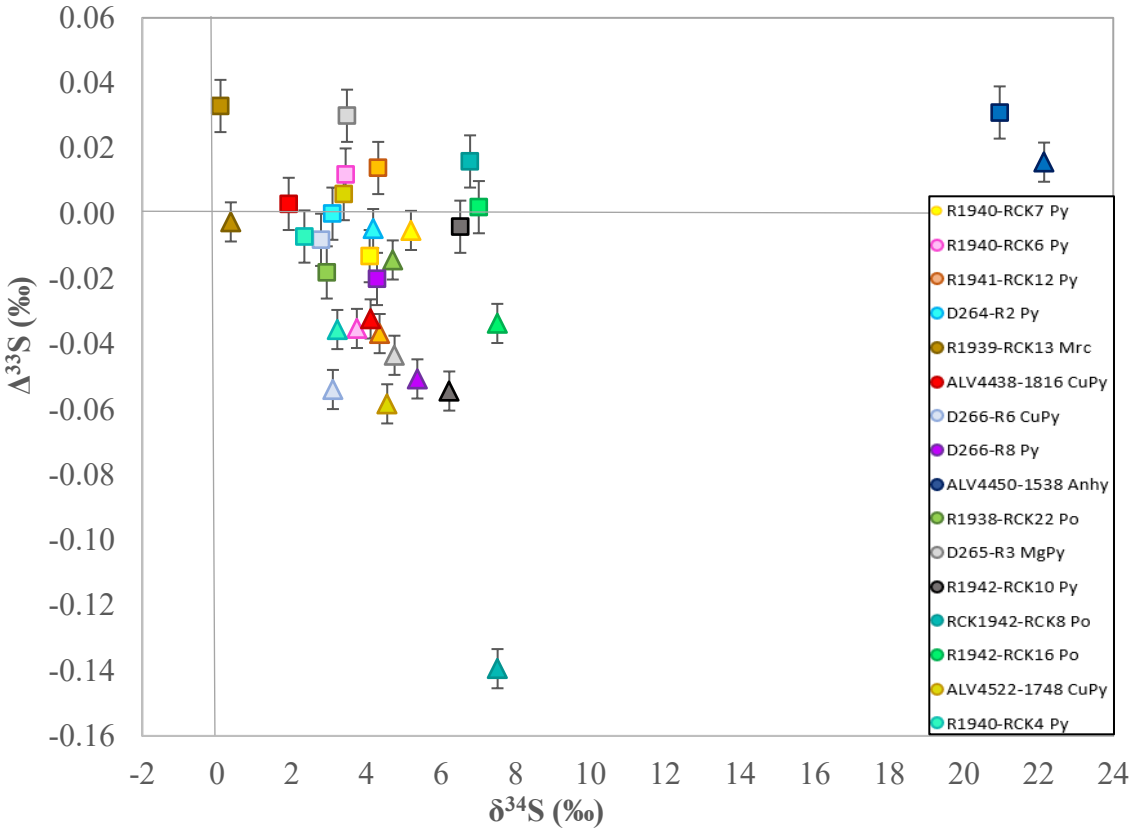


Figure 4.2: Corresponding results highlighting the differences in values for individual samples analyzed at University of Maryland (squares) and Harvard University (triangles). All data are expressed using the exponential definition of $\Delta^{33}S$. Error bars are 1σ. For $\delta^{34}S$, error bars are smaller than the symbols used.

#### 4.1.2.1 Sulfur-33 and IAEA S-1

The absence of a defined value for $\delta^{33}S$ for IAEA S-1 requires different laboratories to use different definitions for normalization (e.g., Ono et al. 2007; Wing and Farquhar, 2015; Tostevin et al., 2014; Peters et al., 2011). To test the significance of this variability on reported $\Delta^{33}S$ values, all the compiled S isotope data from S minerals at modern hydrothermal vent sites reported previously in Figure 1.6 were converted to the Harvard University definition of V-CDT (Table 4.1), where IAEA S-1 has a $\Delta^{33}S$ value of -0.107‰ (Masterson et al., 2016). In general, the normalization resulted in a positive shift of

~0.007‰ for all non-Harvard data, but this shift varies between laboratories, ranging from 0.003‰ to 0.023‰ (Fig. 4.3). Since most of the normalization shifts are within analytical uncertainty (1σ) of their respective data sets, the original values from the previous studies (as presented in Fig. 1.6) are used in this thesis. However, the shift in the data, albeit small, highlights the need to establish an internationally agreed upon $\delta^{33}S$ IAEA S-1 value to improve the quality of future inter-laboratory comparisons.

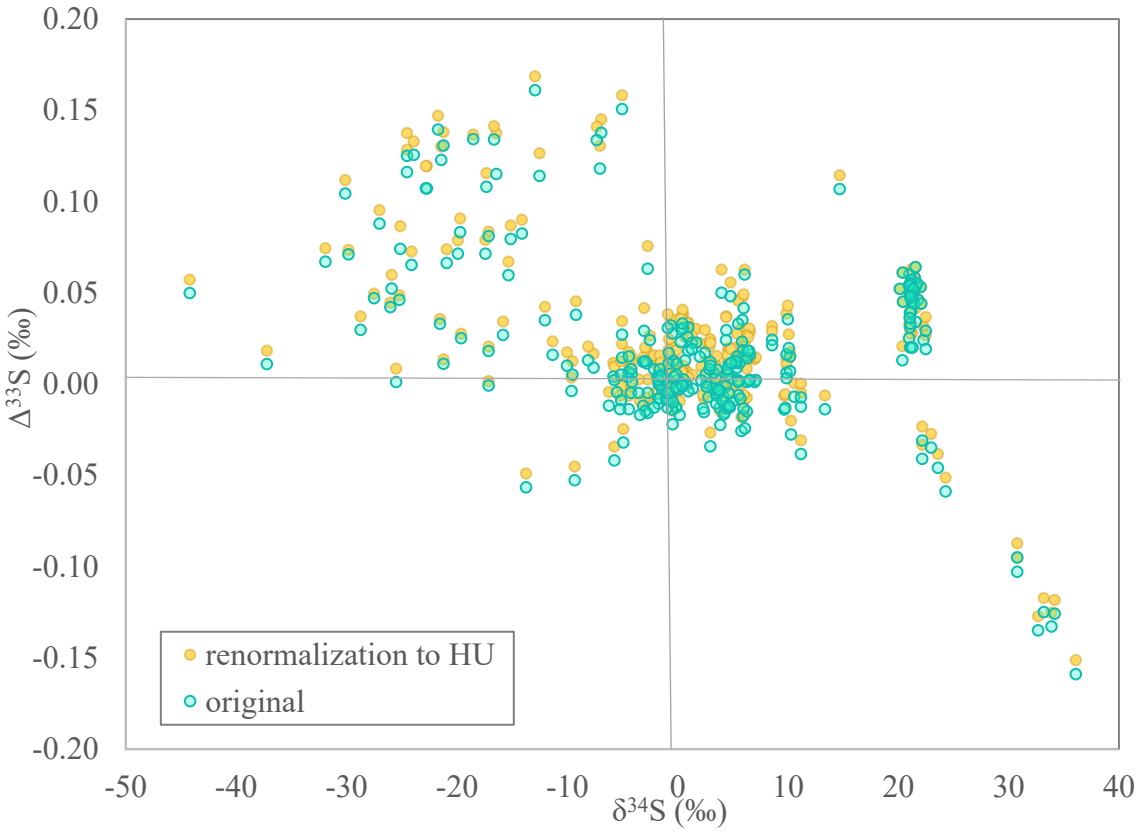


Figure 4.3: Compilation of renormalized and original $\Delta^{33}S$ and $\delta^{34}S$ values from previous multiple S isotope studies of modern MOR systems, (data extracted from: Peters et al., 2010; Peters et al., 2011; Eickmann et al., 2014; Jaeschke et al., 2014; Ono et al., 2007; Ono et al., 2012; McDermott, 2015; McDermott et al., 2015; McDermott et al., 2018; Tostevin et al., 2014; Johnston et al., 2014*). The $\Delta^{33}S$ value of V-CDT used for normalization was retrieved from Masterson et al., (2016). All data are expressed using the exponential definition of $\Delta^{33}S$ in per mil, with respect to V-CDT. Data are listed in Appendix A.

## 4.2 Hydrothermal Fluid Mixing

### 4.2.1 Mixing Models

A series of mixing models were developed to constrain different contributions of S at the different vent fields on the JdFR. Axial Volcano S isotope signatures were hypothesized to fall along a mixing curve between seawater sulfate and basalt-derived S (e.g., Fig. 1.8). Middle Valley samples were hypothesized to have a S source that reflected the influence of a biogenic sulfide contribution from sediments on a hydrothermal system with sulfur otherwise sourced from seawater sulfate and basalt-derived S. Endeavour S isotope signatures were hypothesized to fall within a three-component mixing model similar to Middle Valley if buried sediment did indeed contribute biogenic sulfur to the hydrothermal system.

A two-component mixing model showing mixing between two different S reservoirs is presented in Equation 4.3, where *P* represents the relative mass contribution of each reservoir (defined by Equation 4.6). A two-component mixing model showing the idealized, conservative mixing curve between bulk MOR S ($\delta^{34}S$ and $\Delta^{33}S$ = ~0‰) and seawater sulfate ($\delta^{34}S$ = 21.15‰; $\Delta^{33}S$ = 0.048‰; Johnston et al. [2014]) is shown in Figure 4.5 (by applying Equation 4.5 to both $\delta^{33}S$ and $\delta^{34}S$, and using the calculated values to determine $\Delta^{33}S$) along with the hydrothermal sulfides from a sediment-free hydrothermal

vent system representative of "typical" EPR-type mixing between seawater sulfate and basalt-derived reduced S (Ono et al., 2007).

Equation 4.3

$$\delta^{34}S_{Sample} = \delta^{34}S_{Reservoir\ A}(P_{Reservoir\ A}) + \delta^{34}S_{Reservoir\ B}(P_{reservoir\ B})$$

Equation 4.4

$$P_{Reservoir\ A} = P_{reservoir\ B} - 1$$

If only $\delta^{34}S$ values are considered in two-component mixing relationships (e.g. inset linear mixing line in Fig. 4.4), hydrothermal sulfides will plot on a conservative linear mixture array between the basalt-derived reduced S and seawater sulfate end-members in these sediment-free environments that suggests a simple two-component mixing relationship (e.g., Hannington et al., 2005 and sources therein). However, measurements of multiple S isotopes (i.e., $\Delta^{33}S$) reveal another component that adds a second dimension (y-axis in Fig. 4.4) to the mixing model. For submarine hydrothermal systems, microbially reduced S is the only known S reservoir in the marine/submarine environment with a distinctly positive $\Delta^{33}S$ signature that is coupled with a negative $\delta^{34}S$ signature (outlined field in top left of Fig. 4.4)(Peters et al., 2010; Peters et al., 2011; Eickmann et al., 2014). Therefore, for this thesis, sulfur sources are evaluated using $\delta^{34}S$-$\Delta^{33}S$ mixing models to constrain mixing between basalt-derived S, seawater sulfate, and sediment-derived, microbially reduced sulfide, the isotopic value of which is not well constrained, but averages $\delta^{34}S$ = -18.6‰ and $\Delta^{33}S$ = 0.085‰ (Fig. 4.4; Peters et al., 2010; Peters et al., 2011) (note: this average is used solely as an example, as biogenic sulfide material has a wide range of values; c.f. Fig. 1.7). The three component mixing models presented here

were developed by calculating S isotope endmember mixing lines between different S reservoirs (Samples from Endeavour, Axial Volcano, and Middle Valley are plotted in Figure 4.5 along with the three potential endmembers and their respective mixing lines.

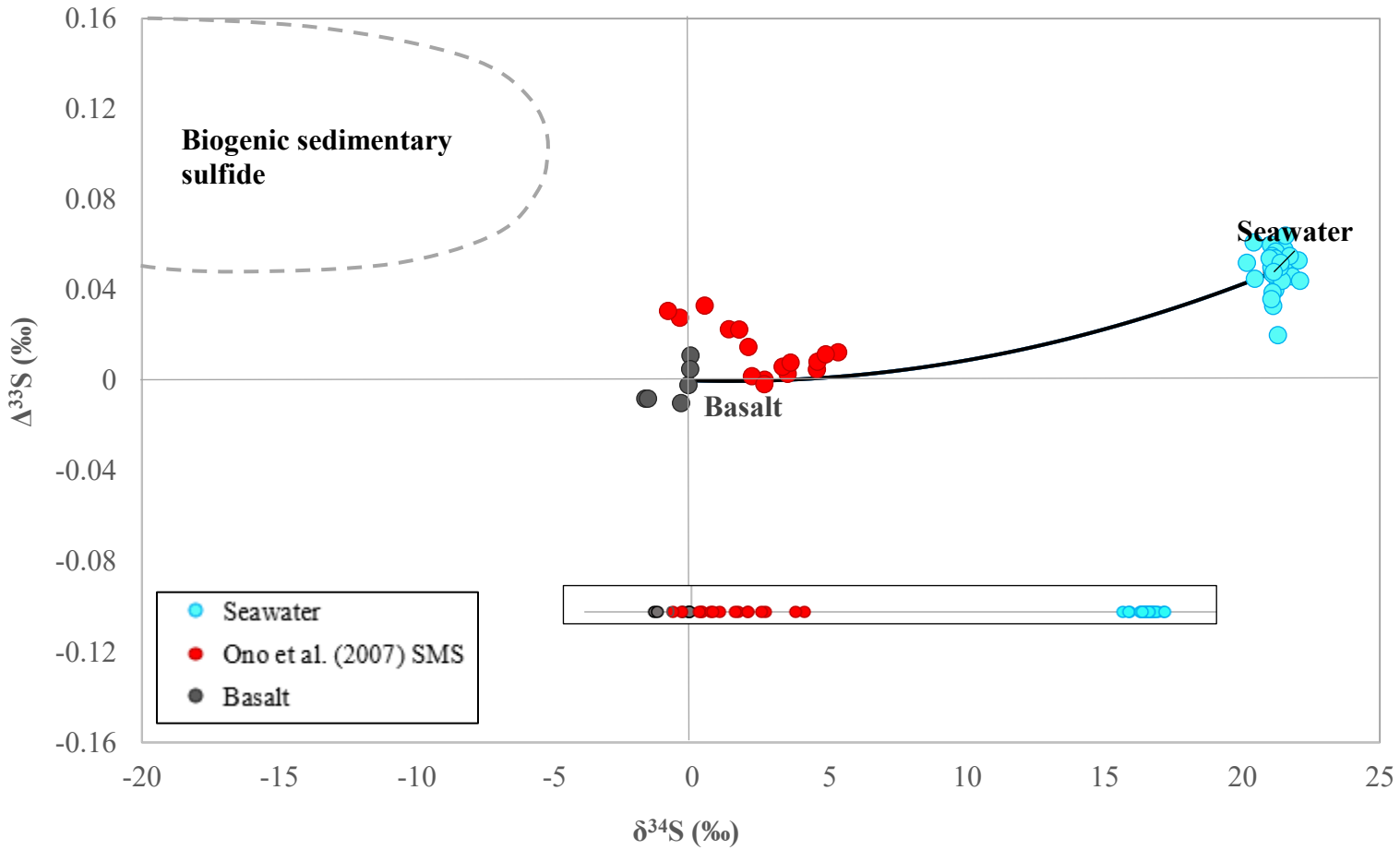


Figure 4.4: Two component mixing model showing theoretical mixing between idealized values of MOR basalt and seawater. The zone in which microbially reduced sulfide occurs is included for reference. Values from multiple S isotope studies of sediment-free modern marine hydrothermal systems (red circles) generally fit along or above the mixing curve. A traditional linear mixing array with only $\delta^{34}S$ data is shown below multiple S isotope data for comparison (Data retrieved from: Peters et al., 2010; Eickmann et al., 2014; Jaeschke et al., 2014; Ono et al., 2007; Ono et al., 2012; Johnston et al., 2014; Tostevin et al., 2014).

Based on the geological setting, it was initially hypothesized that the samples from Middle Valley and Axial Volcano would reveal predictable trends on the mixing plot due to their inferred S sources (i.e., Axial Volcano signatures would fall on the mixing curve between seawater and basalt, and Middle Valley S isotope signatures would trend towards the microbially reduced sulfide field due to entrainment of biogenic sulfide material). It was further hypothesized that these established "endmember scenarios" of S isotope signatures could be used to determine the relative degree to which the three main reservoirs (i.e., seawater, basalt, biogenic sulfide) contributed to the Endeavour samples, where a buried sediment source is hypothesized. However, very few data points fit within the space permissible of a three-component conservative mixture of the assumed S reservoirs and their endmember $\delta^{34}S$ and $\Delta^{33}S$ values. Most samples have more negative $\Delta^{33}S$ signatures than originally predicted (Fig. 4.5). Thus, the original hypotheses required revising to explain the data for all JdFR localities.

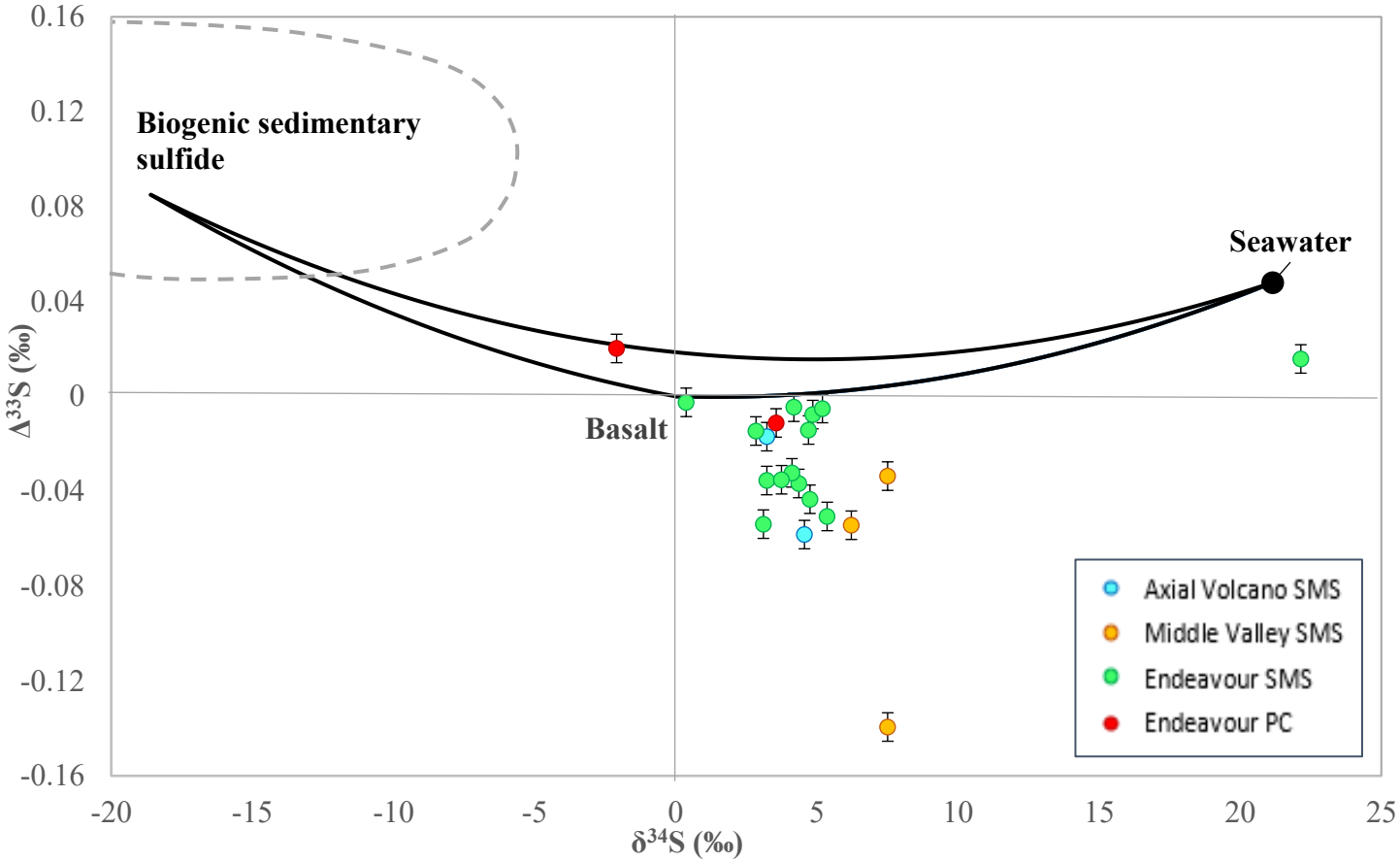


Figure 4.5: Three component mixing model of the main S reservoirs for modern marine hydrothermal systems along with data from the three JdFR sites. Error bars are 1σ. The sedimentary sulfide endmember value is average biogenic sulfide value for sediments from Peters et al. (2010) and (2011). The endmember seawater sulfate value is average calculated by Johnston et al. (2014).

Negative $\Delta^{33}S$ values cannot be produced by mixing of the three endmember reservoirs (Fig. 4.5). Eickmann et al. (2014) reported sulfate samples with negative $\Delta^{33}S$ and positive $\delta^{34}S$ from the Loki's Castle vent site on Mohns Ridge (Fig. 1.6). Eickmann et al. (2014) proposed that highly negative $\Delta^{33}S$ and positive $\delta^{34}S$ values in these sulfate samples were caused by microbial sulfate reduction fixing isotopically light sulfide in the subsurface of the seafloor, which caused the residual sulfate in the system to become progressively more isotopically heavy (more positive $\delta^{34}S$) and more negative $\Delta^{33}S$ prior to its capture in sulfate minerals. However, the model proposed in Eickmann et al. (2014) used a $\delta^{34}S$ value of 0‰ for the original sulfate reservoir that is microbially fractionated. Instead, here we assume standard seawater sulfate as the original sulfate reservoir and use the average values ($\delta^{34}S$: 21.15; $\Delta^{33}S$: 0.048) reported in Johnston et al. (2014).

Using Equation 4.5 (which can also be applied to $\delta^{33}S$), and assuming that the starting S isotope value ($\delta^{34}S_{initial}$) is equal to the average value for seawater sulfate presented in Johnston et al. (2014) and estimating that the biogenic sulfide produced during MSR ($\delta^{34}S_{product}$) is within the range of previously recorded values for sedimentary sulfide (Fig. 1.6), the residual sulfate produced during this reaction does not become more negative for $\Delta^{33}S$, but rather follows a positive trend, and would fall outside the model of endmember S reservoir mixing (Fig. 4.5).

Equation 4.5

$$\delta^{34}S_{residual} = \frac{[\delta^{34}S_{initial} - \delta^{34}S_{product}(P_{product})]}{(1 - P_{product})}$$

To generate hydrothermal sulfide precipitates with negative $\Delta^{33}S$ values and positive $\delta^{34}S$ values like the samples from the JdFR plotted in Figure 4.5, the mixing model was tested with different assumed S isotopic values of the MSR sulfide product. From this investigation, it was found that a minimum $\Delta^{33}S$ value of ~0.7‰ for sulfide product of MSR produced sedimentary sulfide product (denoted by 'x' in Fig. 4.6) is required to form a residual sulfate reservoir (i.e., sulfate remaining in the system after MSR) with $\Delta^{33}S$ values sufficiently negative to encompass most JdFR samples in the mixing model. However, this assumed $\Delta^{33}S$ value of 0.7‰ for the MSR product is well outside the range of values measured for any modern sulfides produced from this microbial process (Fig. 1.6 and included references), making even this modified three-component mixing model (Fig. 4.6) unrealistic.

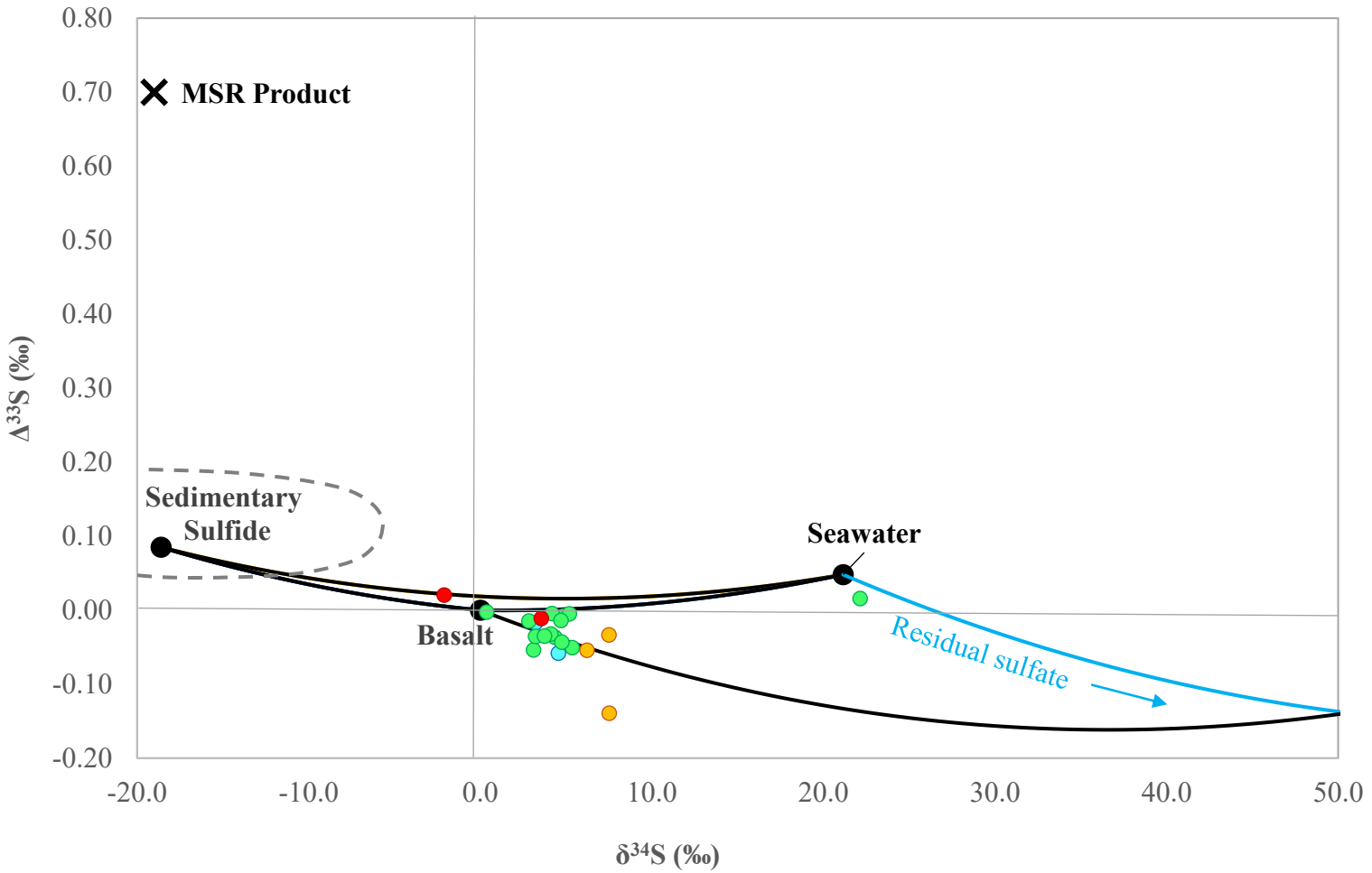


Figure 4.6: Three component mixing model for modern marine hydrothermal systems modified to incorporate a sedimentary sulfide value (denoted as 'X') that would create a residual sulfate value negative enough to produce the JdFR sample S isotope signatures. 1σ error bars are smaller than the symbols. Model data from: Peters et al. (2010); Peters et al. (2011); Eickmann et al. (2014); Jaeschke et al. (2014); Ono et al. (2012); McDermott (2015); McDermott et al. (2015); Johnston et al. (2014).

The initial three-component mixing models (Fig. 4.5 and Fig. 4.6) assume fixed isotopic values for $\delta^{34}S$ and $\Delta^{33}S$ end-member reservoir values. However, a range of S-isotopic values for sedimentary sulfide derived from MSR have been documented (e.g., Peters et al., 2010; Peters et al., 2011; Eickmann et al., 2014), and the seawater and basaltic bedrock S reservoirs, although generally well constrained, are also not unique values but show a range in isotopic values (Ono et al., 2012; Eickmann et al., 2014; Jaeschke et al., 2014; Tostevin et al., 2014; Peters et al., 2010). Measured S isotope measurements of seawater show a range in $\Delta^{33}S$ values from 0.02‰ to 0.064‰; Johnston et al., 2014), the average of which is often taken to represent a fixed S isotope value in mixing models. Similarly, although the S isotope value of unaltered basalt is often approximated to be ~0‰ for both $\Delta^{33}S$ and $\delta^{34}S$ (Fig. 4.4), altered basalts from mid-ocean ridges can show significantly more isotopic variance (Ono et al., 2012; Peters et al., 2010).

Using the full range of modern multiple S isotope values recorded for the three end-member mixing reservoirs (Fig. 4.6), a hybrid mixing-fractionation model (Fig. 4.7) was created. The ranges for S isotope values for the reservoirs were estimated using data from previous studies (Fig. 1.6 and references therein). Mixing lines were then calculated using the extents of ranges of possible S compositions for each reservoir (Fig. 4.7). Mixing lines between the average biogenic sedimentary sulfide and basalt values, and between average basalt and seawater sulfate (Johnston et al., 2014), are included for reference. This modified model allows for a more realistic interpretation of SMS S isotope signatures, as it considers the full extent of known multiple S isotope values in modern marine hydrothermal systems. Because the endmember reservoirs represent ranges of values, the

model is not quantitative. However, by considering the range of possible endmember reservoir values, the hydrothermal samples from the JdFR generally have isotopic values that fit within the hypothesized mixing and fractionation relationships.

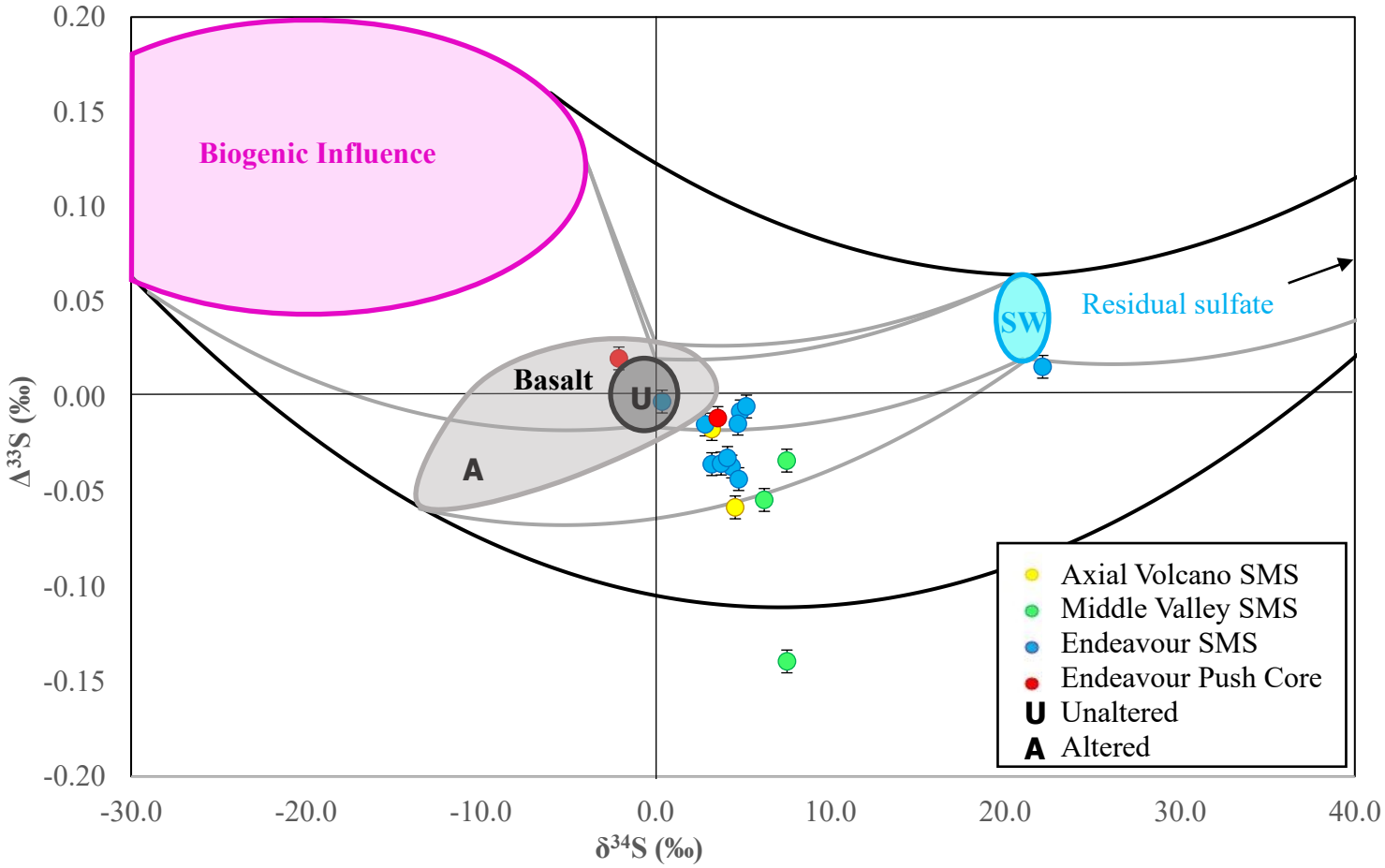


Figure 4.7: Modified mixing model that incorporates the full range of S isotope values for S each reservoir. Solid black lines represent extent of known parameters for modern systems, while grey solid denote the extent of two component mixing ranges within the overall range of known values. Error bars are 1σ. (Model data from: Peters et al., 2010; Peters et al., 2011; Eickmann et al., 2014; Jaeschke et al., 2014; Ono et al., 2012; McDermott, 2015; McDermott et al., 2015; Johnston et al., 2014; Rees, 1973; Kaplan and Rittenburg, 1964).

## 4.3 Site-Specific Sulfur Isotope Signatures

### 4.3.1 Middle Valley

The $\delta^{34}S$ values for sulfide samples from Middle Valley from this study range from 6.2‰ to 7.5‰. Corresponding $\Delta^{33}S$ values are all negative for these samples (-0.034‰ to -0.139‰). Middle Valley hosts abundant turbiditic sediment containing allochthonous organic carbon believed to support the anaerobic, hyperthermophilic, heterotrophic, sulfate reducing organisms present at the site (Frank et al., 2013; Ran and Simoneit, 1994). Sulfate reducing microbes preferentially metabolize lighter isotopes, thereby producing isotopically light reduced S products with $\delta^{34}S$ values as low as -50‰ (Canfield, 2001). Despite the documented presence of anaerobic sulfate reducing heterotrophic organisms at Middle Valley (Frank et al., 2013), previous S isotope studies of surficial hydrothermal sulfide samples at Middle Valley have consistently reported a range in positive $\delta^{34}S$ values (e.g., 1.3‰ to 9.8‰ [Duckworth et al., 1994]; 1.6‰ to 8.4‰ [Stuart et al., 1994]) that, consistent with this study, trend towards a more isotopically heavy average value ($\delta^{34}S$= ~8‰ [Adshead, 1996]) relative to typical sediment-free EPR (Hannington et al., 2005; Zierenberg, 1994; Adshead, 1996; Duckworth et al., 1994; Stuart et al., 1994). The only $\delta^{34}S$ values for sulfide material reported from Middle Valley that are consistent with expected signatures for MSR are from samples taken at depth from cores ($\delta^{34}S$ range: -39.7‰ to -12.8‰ [Goodfellow and Blaise, 1988]). The isotopically heavy values for the surficial samples contrast hypotheses posited by this thesis and others (e.g., McDermott et

al., 2015) that entrainment of biogenic sulfides produced by MSR in sedimented hydrothermal systems would produce isotopically light SMS deposits.

There have been several suggested sources for the isotopically heavy S present in Middle Valley SMS deposits, ranging from a primitive sulfur input (Goodfellow and Blaise, 1988), entrainment of isotopically heavy seawater sulfate in late stage hydrothermal fluids (e.g., Stuart et al., 1994; Goodfellow and Franklin 1993), to the entrainment of reduced seawater sulfate that was infiltrated and trapped in sedimentary pore fluids (Duckworth et al., 1994; Stuart et al., 1994). While the process of incorporation is contested, most of these studies agree that the isotopically heavy $\delta^{34}S$ values are related to the incorporation of a sulfur source ultimately derived from seawater. However, although one sample from Middle Valley has an isotopic value that is consistent with mixing between basalt and seawater sulfate, the other samples require a residual seawater sulfate source that has already been fractionated (Fig. 4.7).

Rayleigh distillation is a fractionation process that could account for both the anomalously positive $\delta^{34}S$ (relative to EPR) and negative $\Delta^{33}S$ values for Middle Valley SMS samples (Shanks et al., 1995). Rayleigh distillation is a distinct type of open system reservoir effect in which isotope fractionation occurs between two phases, and one of the phases is progressively removed from the system. Rayleigh distillation leads to a progressive overall change in the isotopic composition of the system and can lead to wide ranges in S isotope values (Shanks et al., 1995). At Middle Valley, which is an open system with respect to S (Goodfellow and Blaise, 1988), hyperthermophilic heterotrophic bacteria reduce seawater sulfate in the hydrothermal recharge zone below the seafloor (Frank et al., 2013), where it becomes fixed in the subsurface (Goodfellow and Blaise, 1988). The

systematic removal of the lighter isotopes would drive the remaining seawater sulfate in the fluid (residual sulfate) to become progressively more isotopically heavy with respect to $\delta^{34}S$ (e.g., Fig. 4.6). Sulfur reservoir mixing between thermochemically reduced residual sulfate and remobilised reduced sulfur leached from altered basalt could generate the $\Delta^{33}S$ values observed in Middle Valley SMS samples (Fig. 4.7).

Similarly, microbial reduction of sulfate from fluids in a basalt environment dominated by igneous sulfur with a near zero for both $\Delta^{33}S$ and $\delta^{34}S$ can result in residual sulfate with negative $\Delta^{33}S$ values, resulting in microbially altered basalts from open systems with negative $\Delta^{33}S$ values (e.g., Ono et al., 2012). Using the model in Figure 4.7, the S isotope signatures at Middle Valley are consistent with subseafloor interactions between open-system microbially altered basalt derived S and thermochemically-reduced seawater sulfate.

The mixing-fractionation model summarized in Figure. 4.7 is illustrated in Figure 4.8 with respect to the isotopic evolution of S in hydrothermal fluid at Middle Valley. Seawater sulfate infiltrates the permeable sedimented seafloor. Microbial sulfate reduction results in precipitation of isotopically light biogenic sulfide in the subsurface (e.g., the pyrite signatures of Goodfellow and Blaise, 1988) at temperatures high enough for anaerobic hyperthermophilic sulfate reducing bacteria to thrive (>80°C; Butterfield et al., 2004), but too low to readily dissolve iron sulfide (<150°C; Giggenbach, 1974), thereby removing light isotopes from downwelling seawater during hydrothermal recharge. The residual sulfate in the hydrothermal fluid becomes enriched in heavy S isotopes and more negative with respect to $\Delta^{33}S$. Anhydrite is precipitated at 150°C (Elderfield et al., 1999),

removing some sulfate from the hydrothermal fluid. The remaining sulfate is progressively heated, and thermochemically reduced. No significant fractionation is associated with thermochemical reduction of dissolved sulfate to sulfide when the process proceeds to completion (Machel et al., 1995). The reduced dissolved S in the hydrothermal fluid then interacts with leached, basalt-derived reduced S and subseafloor sediments. The mixed reduced S then ascends in thermally buoyant hydrothermal fluid to the seafloor and discharges at zones where sediment is at minimum (i.e., above basement edifices; Davis and Villinger [1992]). The precipitated SMS deposits formed by these processes are enriched in $^{34}S$ and have negative $\Delta^{33}S$ values.

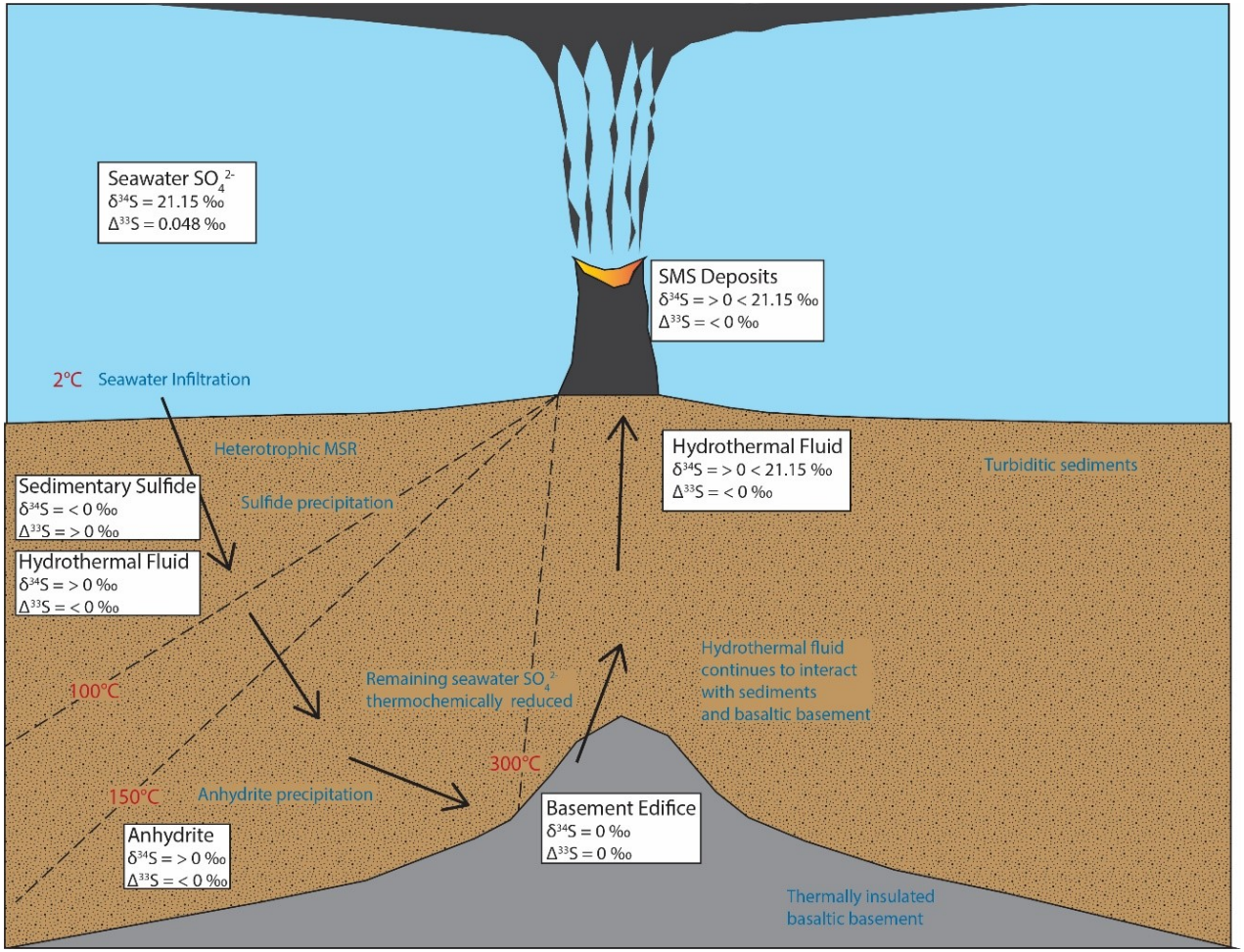


Figure 4.8: Model of hydrothermal fluid progression and evolution through interactions with various S sources at Middle Valley, on the Juan de Fuca Ridge. (Modified from Jamieson, 2005; including known parameters from Peters et al., 2010; Peters et al., 2011; Eickmann et al., 2014; Jaeschke et al., 2014; Ono et al., 2007; Ono et al., 2012; Johnston et al., 2014; Davis and Villinger, 1992; Machel et al., 1995). All data are expressed using the exponential definition of $\Delta^{33}S$ in per mil, with respect to V-CDT.

### 4.3.2 Axial Volcano

Axial volcano is a sediment-free site. Previous studies indicate that S isotope values from hydrothermal sulfides at these sites can generally be explained by two-component mixing between seawater sulfate and unaltered basalt-derived S (e.g., Ono et al., 2007) (Fig. 4.4). The lack of turbiditic sediment (and associated allochthonous organic material) at these sites make conditions generally unfavourable for heterotrophic sulfate reducers. However, results from this thesis and previous studies indicate that Axial Volcano exhibits S isotope signatures atypical for sediment-free MOR sites (i.e., more positive $\delta^{34}S$, with negative $\Delta^{33}S$ values potentially indicative of a significant microbial or alteration component).

Sulfur isotope values reported for vent fluid and SMS samples from Axial Volcano reported to date are generally enriched in the heavy isotopes of S. Vent fluid $H_2S$ at ASHES has positive $\delta^{34}S$ values that range from approximately 6.1‰ to 7.3‰ (Shanks et al., 1995 and sources therein). Hannington and Scott (1988) reported sulfide-rich samples at CASM with $\delta^{34}S$ values ranging from 2‰ to 6‰. Crowe and Valley (1992) reported isotopically heavy wurtzite at CASM, with $\delta^{34}S$ values of up to 9‰. The $\delta^{34}S$ values from these samples overlap but are on average slightly heavier than EPR-type SMS deposits (Hannington et al., 2005).

Hydrothermal sulfide samples that are enriched in the heavy isotope are typically attributed to a higher proportion of a seawater sulfate component, due to the well-

constrained positive $\delta^{34}S$ value of 21‰ for seawater sulfate. For example, Hannington and Scott (1988) suggested the possibility of anhydrite incorporation and replacement in addition to abiotic sulfate reduction of seawater sulfate in the hydrothermal fluid to explain the positve $\delta^{34}S$ values at Axial. The $\Delta^{33}S$ data from this study allows the premise of significant incorporation of seawater sulfate to be tested in a similar fashion to the Middle Valley samples.

The sulfide sample $\delta^{34}S$ values from Axial Volcano for this study are 3.2‰ and 4.6‰, which are consistent with previous work on surficial samples from Axial Volcano. However, like Middle Valley, the $\Delta^{33}S$ values are all negative for these samples (-0.058‰ to -0.017‰) suggesting that the samples do not fall along the two-component mixing curve between seawater sulfate and magmatic S (Fig. 4.5) and fractionation processes and/or S reservoirs other than those described in EPR-type two-component mixing are affecting the hydrothermal fluids at Axial Volcano. Two potential explanations that can account for the coupled positive $\delta^{34}S$ and negative $\Delta^{33}S$ values sulfide samples at Axial Volcano are 1) MSR; and 2) disproportionation of magmatic $SO_2$.

Despite conditions not being favourable for heterotrophic MSR at sediment-free submarine hydrothermal systems, Butterfield et al. (2004) reported the presence of thermophilic and hyperthermophilic microbes, including anaerobic heterotrophic sulfate reducers (*Thermodesulfobacterium* spp.) and chemolithoautotrophic sulfate reducers (*Desulfurobacterium* spp.), in low-temperature (<80°C) diffuse vent fluids at Axial Volcano. Both types of bacteria are associated with optimum growth at high temperatures (>80°C), indicating that the bacteria did not originally grow in the low-temperature diffuse

fluids from which they were collected, but rather were transported from higher temperature fluids occurring at depth within the hydrothermal system. The presence of thermophilic heterotrophic and chemolithoautotrophic sulfate reducers indicates both inorganic and organic-supported MSR occurring at depth within the high temperature subseafloor hydrothermal system (Butterfield et al., 2004). Butterfield et al. (2004) proposed that organic-supported MSR occurring at depth is supported by former macrofaunal communities buried underneath later basalt flows. Subsurface MSR could produce microbially altered basalt and residual sulfate that would influence the S isotope signatures of hydrothermal fluids and related SMS deposits at Axial Volcano to produce isotopic values compatible with the three-component mixing model outlined in Figure 4.7. The isotopic values of hydrothermal deposits at Axial would be similar to Middle Valley but without the requirement for organic-rich sediments in the downwelling zones. Specifically, while both Axial Volcano samples are not within the mixing curve between seawater sulfate and unaltered basalt, they do fit within the range of mixing between open system microbially altered basalt and seawater sulfate.

At typical mid-ocean ridge systems, hydrothermal sulfate minerals generally have $\delta^{34}S$ values equal to that of seawater (21‰) (e.g., Jaeschke et al., 2014). However, S disproportionation at submarine hydrothermal systems can result in isotopically lighter sulfate minerals with $\delta^{34}S$ values slightly less than that of seawater (Kim et al., 2004; McDermott et al., 2015). Sulfur disproportionation had not been considered as a potential source of fractionation at Axial because this process is typically associated with gas-rich arc-related settings (McDermott et al., 2015 and sources therein). However, previously

reported $\delta^{34}S$ values of sulfate minerals from CASM are generally slightly less than that of seawater, with some samples having $\delta^{34}S$ values as low as 16‰ (Hannington and Scott, 1988), potentially indicative of $SO_2$ disproportionation. Axial Volcano is enriched in volatiles relative to other MOR sites as evidenced by $CO_2$-enriched melt inclusions present in the abundant pyroclastic deposits surrounding the volcano (Helo et al., 2011), high levels of magmatic $CO_2$ in hydrothermal fluids (Butterfield et al., 1990; Butterfield et al., 2004), and high total gas content in hydrothermal fluids indicative of magmatic degassing (Butterfield et al., 2004). These data indicate that $SO_2$ may provide an additional sulfur source to the hydrothermal system at Axial. However, the reduced S product of $SO_2$ disproportionation is relatively depleted in $^{34}S$ and would result in sulfide minerals or fluid $H_2S$ with a more negative $\delta^{34}S$ values (McDermott et al., 2015). However, the positive $\delta^{34}S$ values of the sulfide deposits at Axial suggest that, if $SO_2$ is providing an additional source of sulfur to the system, that relative abundance of that source is negligible within the limits of the resolution of the sulfur isotope analyses, with respect to both $\Delta^{33}S$ and $\delta^{34}S$.

The sub-surface mixing-disproportionation model for Axial Volcano is illustrated in Figure 4.9 with respect to the isotopic evolution of S in hydrothermal fluid. Seawater sulfate infiltrates the subseafloor, where it is progressively heated with depth. Anearobic hyperthermophilic and thermophilic heterotrophic and chemolithoautotrophic microbial sulfate reducers convert some of the seawater sulfate present in the heated hydrothermal fluid to $H_2S$. The $H_2S$ precipitates as isotopically light biogenic sulfide, while isotopically heavy residual sulfate continues to cycle through the hydrothermal system. Some of this residual sulfate precipitates as anhydrite at ~150°C (Elderfield et al, 1999), and the

remainder is thermochemically reduced with progressive heating (e.g., Machel et al., 1995). At ~400°C, the hydrothermal fluid may interact with products of magmatic degassing (i.e., disproportionated isotopically heavy $HSO_4$ and isotopically light $H_2S$ or $S^0$. These sub-surface processes result in SMS deposits with varied, but generally isotopically heavy S (positive $\delta^{34}S$) with negative $\Delta^{33}S$ values.

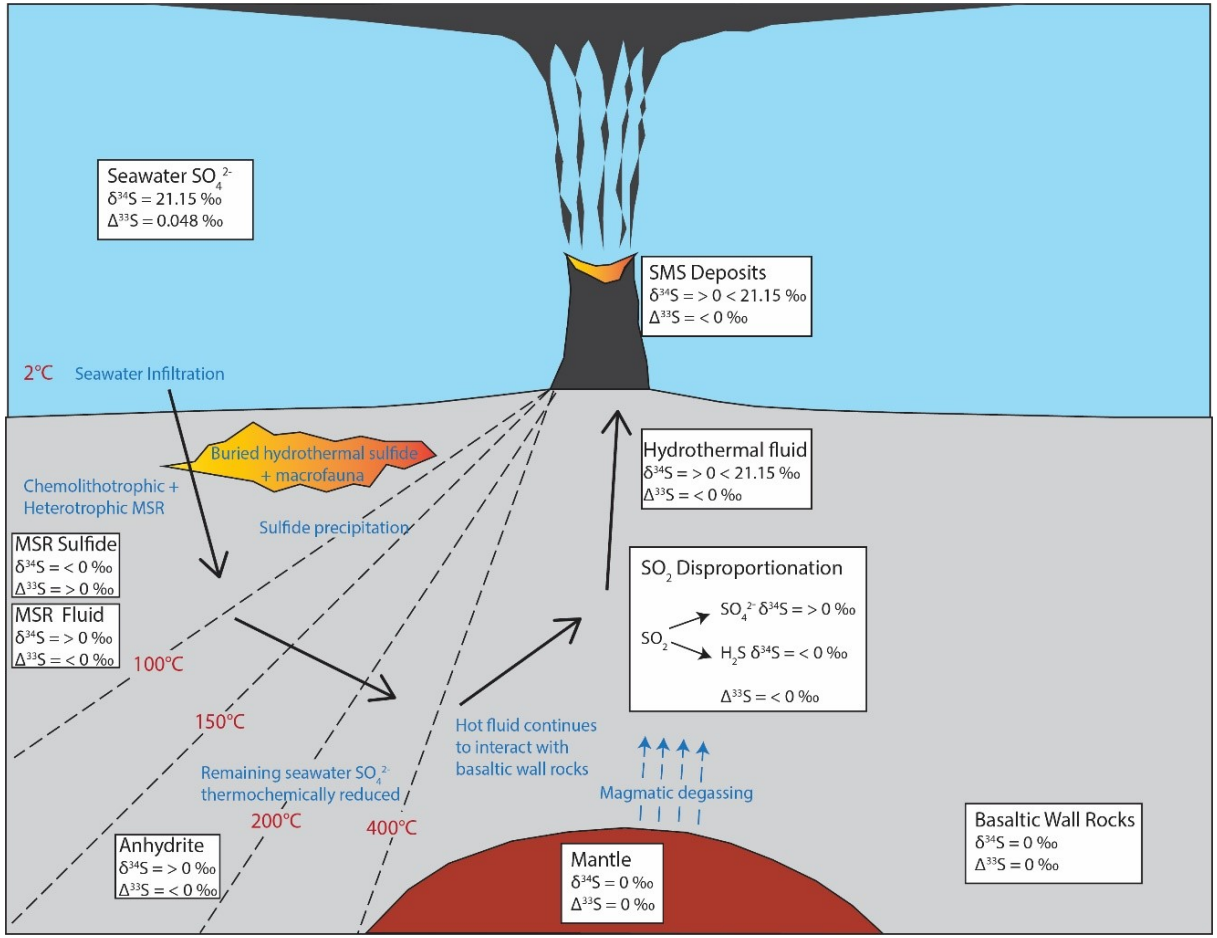


Figure 4.9: Model of hydrothermal fluid progression and evolution through interactions with various S sources at Axial Volcano, on the Juan de Fuca Ridge. (Modified from Jamieson, 2005; including known parameters from Peters et al., 2010; Peters et al., 2011; Eickmann et al., 2014; Jaeschke et al., 2014; Ono et al., 2007; Ono et al., 2012; Johnston et al., 2014; Machel et al., 1995; Jamieson et al., 2016a; Reeves et al., 2011). All data are expressed using the exponential definition of $\Delta^{33}S$ in per mil, with respect to V-CDT.

### 4.3.3 Endeavour

Endeavour is a sediment-free MOR site, but one which may have buried sediment (Lilley et al., 1993; You et al., 1994; Kelley et al., 2012; Seyfried et al., 2003). Accordingly, S isotope signatures of sulfide and sulfate samples could capture a mixture between seawater sulfate and basalt-derived S, with potential entrainment of biogenic sulfide indicative of buried sediment, as was initially hypothesized. Endeavour S isotope signatures show significant variation within and between the various vent areas, particularly with respect to $\Delta^{33}S$. Excluding one anhydrite sample (ALV4450-1538; $\delta^{34}S$: 22.2‰ and $\Delta^{33}S$: 0.016‰), which is thought to represent seawater sulfate heating to 150°C upon interaction with high temperature vent fluid, and one marcasite sample (R1939-RCK-13; $\delta^{34}S$: 0.4‰ and $\Delta^{33}S$: -0.003‰), the S isotope values of SMS samples at Endeavour have a generally consistent slight heavy isotope enrichment (average $\delta^{34}S$: 4.2‰; standard deviation: 0.8‰) with variable but generally negative $\Delta^{33}S$ values (range from -0.005‰ to -0.054‰) without clear or consistent mineral-specific deviations between locations. It is assumed that, because of the lack of variation in isotopic composition, these samples are generally representative of direct precipitation from hydrothermal vent fluid.

Similar to Middle Valley and Axial, the negative $\Delta^{33}S$ values of the SMS samples at Endeavour eliminates the application of the two-component mixing model for seawater sulfate and S derived from unaltered basalt for most samples (Fig. 4.5). In the following sections, the sulfur sources for all SMS samples from Endeavour, except for the marcasite sample from the Main Endeavour Field (considered separately in Section 4.3.3.1), are

discussed in groups based on sampling locality. Two push core sediment samples from the Endeavour area are also discussed separately in Section 4.3.3.2.

The $\delta^{34}S$ values for SMS samples from MEF, Salty Dawg and High Rise (4.2‰ to 4.9‰) are consistent with previously reported vent fluid $H_2S$ $\delta^{34}S$ values at Endeavour, which ranged from of 3.8‰ to 5‰ (Shanks et al., 1995; Hannington et al., 2005), and are consistent with $\delta^{34}S$ values from the sediment-free EPR. These conditions are supported by the near-zero $\Delta^{33}S$ values for the Salty Dawg sample and one sample from High Rise. These two samples (and one sulfide sample from MEF, discussed below) constitute the only samples that fall (within uncertainty) directly on a S isotopic mixing curve between S derived unaltered basalt and seawater sulfate. The more negative $\Delta^{33}S$ value from the remaining High Rise sample does not fall on this mixing curve. However, it does fall within the mixing range between microbially altered basalt-derived S and seawater sulfate, and thus could indicate a microbial component (Fig. 4.10).

The $\delta^{34}S$ values for SMS samples from the Main Endeavour Field (MEF) display a larger range (3.2‰ to 5.2‰) than previously reported from vent fluid $H_2S$ $\delta^{34}S$ at Endeavour (Shanks et al., 1995; Hannington et al., 2005). The most isotopically heavy sample from the MEF ($\delta^{34}S$= 5.2‰) has a $\Delta^{33}S$ value (-0.005‰) that lies along the mixing curve between unaltered basalt and seawater sulfate within its analytical uncertainty (Fig. 4.10). Therefore, this is the only sample from MEF where seawater sulfate incorporation in late stage hydrothermal fluids, i.e., EPR-type two component mixing, is supported. In contrast, three samples from MEF have negative $\Delta^{33}S$ values that lie outside of the two-component mixing curve between seawater sulfate and unaltered basalt. Similar to the

single High Rise sample, the S isotopic value of this sample can be explained by mixing S from altered basalt and seawater sulfate and thus indicate a potential altered basalt/microbial component. The sulfate sample from Mothra has a S isotopic value ($\delta^{34}S$: 22.2‰ and $\Delta^{33}S$: 0.016‰) that overlaps, within uncertainty, with seawater sulfate and thus can be explained as being derived entirely from seawater without any S disproportionation (Jaeschke et al., 2014).

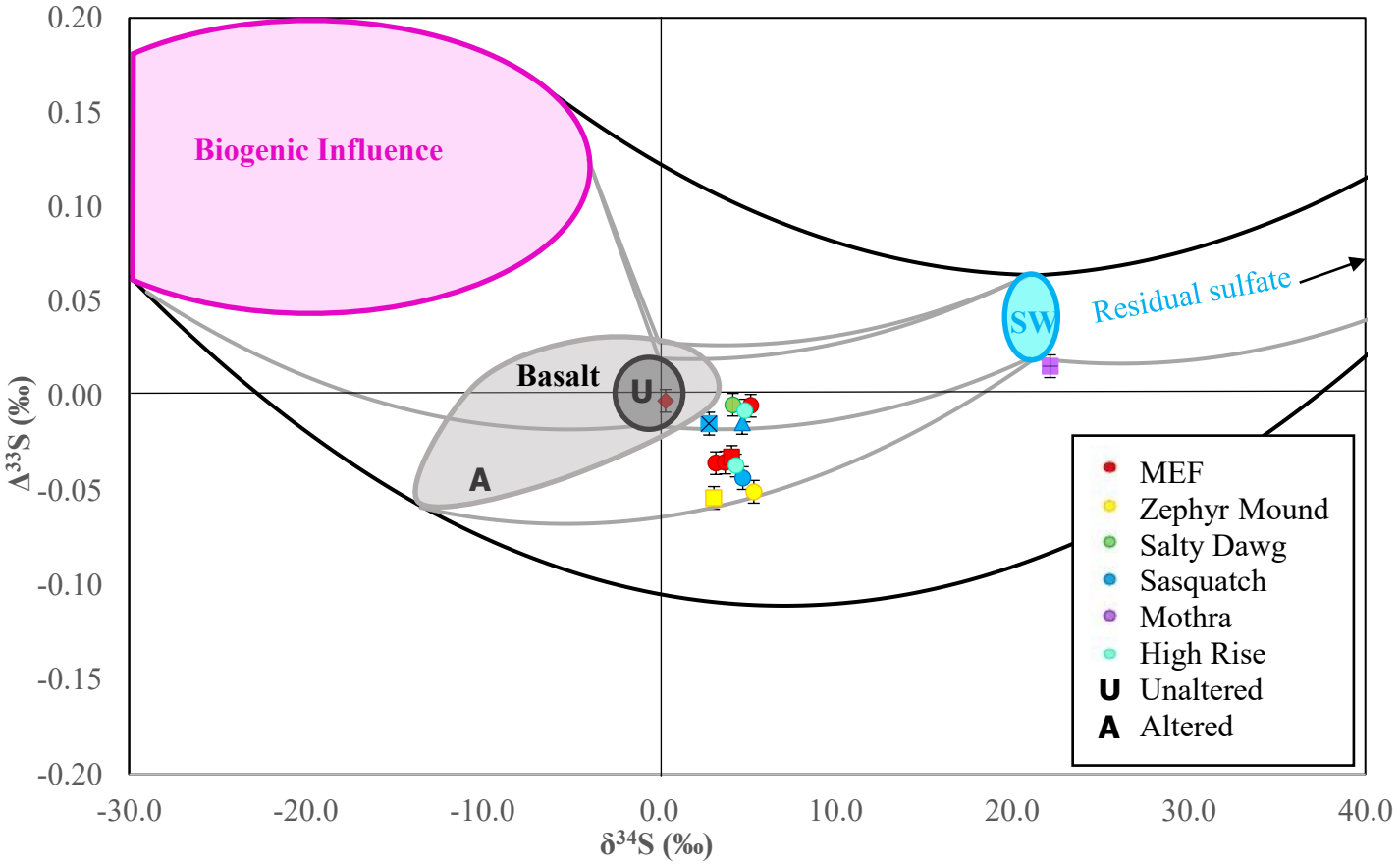


Figure 4.10: Mixing model from Fig. 4.7 with location and mineral specific data from Endeavour. Error bars are 1σ. Pyrite is denoted by circles, chalcopyrite by squares, marcasite by a diamond, pyrrhotite by a triangle, sulfate by a square with a "+", and wurtzite by a square with an "x." (Model data retrieved from: Peters et al., 2010; Peters et al., 2011; Eickmann et al., 2014; Jaeschke et al., 2014; Ono et al., 2012; McDermott, 2015; McDermott et al., 2015; Johnston et al., 2014; Rees, 1973; Kaplan and Rittenburg, 1964).

Based on the range in S isotope data at Endeavour, two separate processes could generate the isotopic signatures in the sulfide samples. For samples with near-zero $\Delta^{33}S$, a more straightforward mixture between unaltered basalt-derived S and seawater sulfate can be invoked. For samples with more negative $\Delta^{33}S$, similar mixing scenario of seawater sulfate with altered basalt rather than unaltered basalt can be invoked. In both cases, the original hypothesis of testing for buried sediments beneath basaltic flows cannot be resolved, as it is not possible to distinguish between sediment buried beneath basalt flows and microbially altered basalt through the use of S isotopes alone. Instead, the S isotope signatures at Endeavour overlap largely with those at Axial Volcano and thus could be explained entirely by having a buried organic source (such as the macrofaunal communities suggested by Butterfield et al. [2004]) that drive open-system MSR.

The two separate S source/mixing processes inferred at Endeavour are illustrated in Figure 4.11 with respect to the isotopic evolution of S in hydrothermal fluid. Where sulfide samples exhibit evidence of EPR-type two-component mixing, infiltrated seawater is progressively heated causing anhydrite to precipitate. The hydrothermal fluid further interacts with basalt-derived S in the subseafloor, where remaining sulfate is thermochemically reduced. As temperatures continue to increase and the fluid becomes thermally buoyant, it ascends and discharges at the seafloor, forming chimney structures.

The isotope signatures associated with interactions between hydrothermal fluid and various potential S reservoirs are less clear where signatures exhibit evidence of microbial influence, as several factors could influence these various sources. Some of the infiltrated

seawater sulfate is reduced to $H_2S$ via MSR through heterotrophic mechanisms via interactions buried sediments and/or macrofauna. Likewise, some infiltrated seawater is reduced to $H_2S$ via MSR through chemolithoautotrophic sulfate reduction. In both cases, resultant $H_2S$ is precipitated as biogenic sulfide, removing light isotopes from the hydrothermal fluid and generating isotopically heavy residual sulfate (positive $\delta^{34}S$) with a negative $\Delta^{33}S$ signature. The residual sulfate is thermochemically reduced and discharged onto the seafloor, producing sulfide samples with positive $\delta^{34}S$ and negative $\Delta^{33}S$ values.

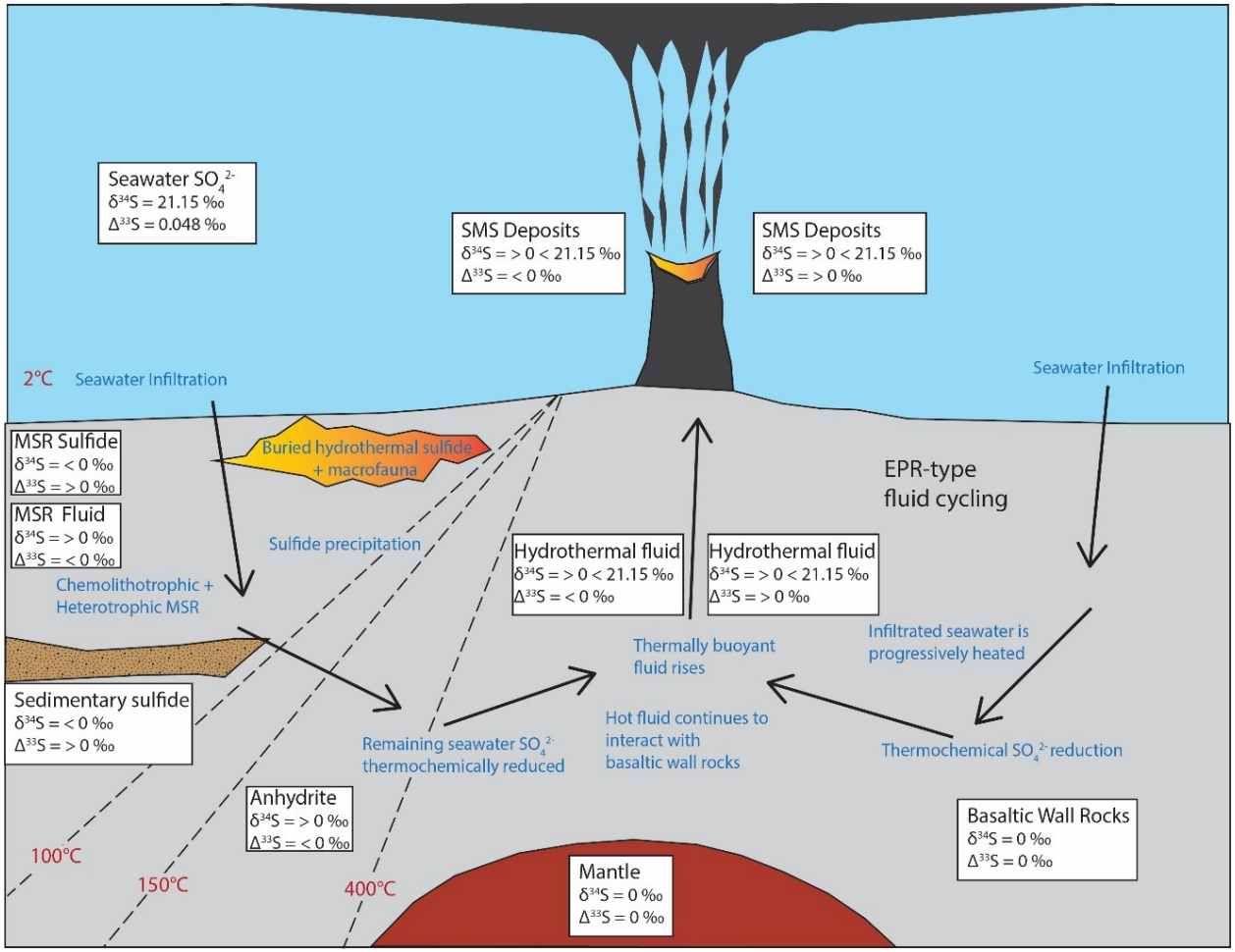


Figure 4.11: Model of hydrothermal fluid progression and evolution through interactions with various S sources at Endeavour, on the Juan de Fuca Ridge. (Modified from Jamieson, 2005; including known parameters from Peters et al., 2010; Peters et al., 2011; Eickmann et al., 2014; Jaeschke et al., 2014; Ono et al., 2007; Ono et al., 2012; Johnston et al., 2014; Jamieson et al., 2016a; Machel et al., 1995). All data are expressed using the exponential definition of $\Delta^{33}S$ in per mil, with respect to V-CDT.

#### 4.3.3.1 Isotopically Light Marcasite

The single marcasite sample from the MEF (R1939-RCK-13) differs from other SMS with its near-zero values for both $\delta^{34}S$ and $\Delta^{33}S$ (Fig. 3.2). These signatures are, however, consistent with previously published values for hydrothermal vent marcasite (Fig. 3.4)(Ono et al., 2007). The marcasite sample's near-zero S isotope values place the sample in the region of basalt-derived S (Fig 4.12). To achieve these near-zero values through basalt/seawater S mixing alone, the sample must be composed nearly entirely of basalt-derived S with little to no seawater sulfate component. This was unlike all other sulfide samples from Endeavour, which had consistent slightly positive $\delta^{34}S$ values with slightly negative $\Delta^{33}S$ values (Fig. 4.7), indicating precipitation from a relatively homogenous hydrothermal fluid with S derived from both seawater sulfate and altered basalt and localized microbial components (Fig. 4.10). Several iron disulfides (including marcasite) from Ono et al. (2007) were stated to be in isotopic disequilibrium with corresponding sulfide samples (i.e., sphalerite and chalcopyrite). This suggests that marcasite, which normally forms on the exterior of active chimneys under slightly lower pH conditions than pyrite, may be forming via other mechanisms rather than direct precipitation from a homogenous hydrothermal fluid (Juniper et al., 1992).

Paradis et al. (1988) reported the presence of marcasite beneath colonies of hydrothermal vent vestimentiferan tube worms, while Juniper at al. (1988) noted the presence of elemental S in worm tubes at hydrothermal vents. Though direct marcasite precipitation is not a significant process at temperatures below 300°C (Shoonen and Barnes, 1991a), intermediary species, such as elemental S, can promote precipitation of

marcasite (Juniper et al., 1992; Shoonen and Barnes, 1991a; Shoonen and Barnes, 1991b; Shoonen and Barnes, 1991c). Elemental S can be released as a by-product during biological sulfide oxidation and can also be produced by biological digestion processes, thereby released as a component of fecal matter (Desbruyères et al., 1985; Juniper et al., 1992). Paradis et al. (1988) suggested that iron sulfide (FeS) could react with the elemental S present in tube mucous, thereby forming the marcasite ($FeS_2$) lining observed beneath the tube worm colonies. Though it provides a helpful context, the formation of marcasite via organically produced intermediary species at submarine hydrothermal vents is likely not a process that is limited to tube worms, as many different autotrophic S oxidizing microbial species have been isolated from hydrothermal vent fluids collected from numerous sites (e.g., Ruby et al., 1981; Seivert et al., 2008; Meier et al., 2017).

If a biogenic sulfide component is assumed to be involved and contributing to the marcasite S isotope value, there is another mechanism to explain the near-zero $\delta^{34}S$ and $\Delta^{33}S$ values apart from a dominance of basalt-derived S. Specifically, it is possible that the hydrothermal vent fluid $H_2S$ mixed subsequently with biogenic sulfide. To explore this possibility, the mean S isotope value of all other MEF sulfide samples ($\delta^{34}S$: 4.1‰; $\Delta^{33}S$: -0.027‰) is used as an end-member (presumed to represent the vent fluids) and mixed with an average biogenic sulfide value ($\delta^{34}S$: -18.6‰; $\Delta^{33}S$: 0.085‰) of sedimentary pyrite samples reported in Peters et al. (2010) and (2011) (average value used solely as an example, as biogenic sulfide material has a wide range of values; c.f. Fig. 4.12). The marcasite sample S isotope value falls along the trend of a mixing curve between these endmembers (Fig. 4.12). Similarly, the S isotope signatures of marcasite from Lucky Strike

reported in Ono et al. (2007) fall along the trend of a mixing curve between the mean S isotope value of other sulfide samples from Lucky Strike reported in the same study (chalcopyrite; presumed to represent endmember vent fluids) and the average biogenic sulfide value of sedimentary pyrite samples reported in Peters et al. (2010; 2011); Fig. 4.12). It is therefore possible that the some isotopically lighter marcasite formed at submarine hydrothermal vent systems via a reaction between by-products of biological processes (S) and iron sulfide (FeS) source from hydrothermal fluid. However, the wide range in S isotopic values of possible biogenic S leaves a wide envelope of uncertainty on these models.

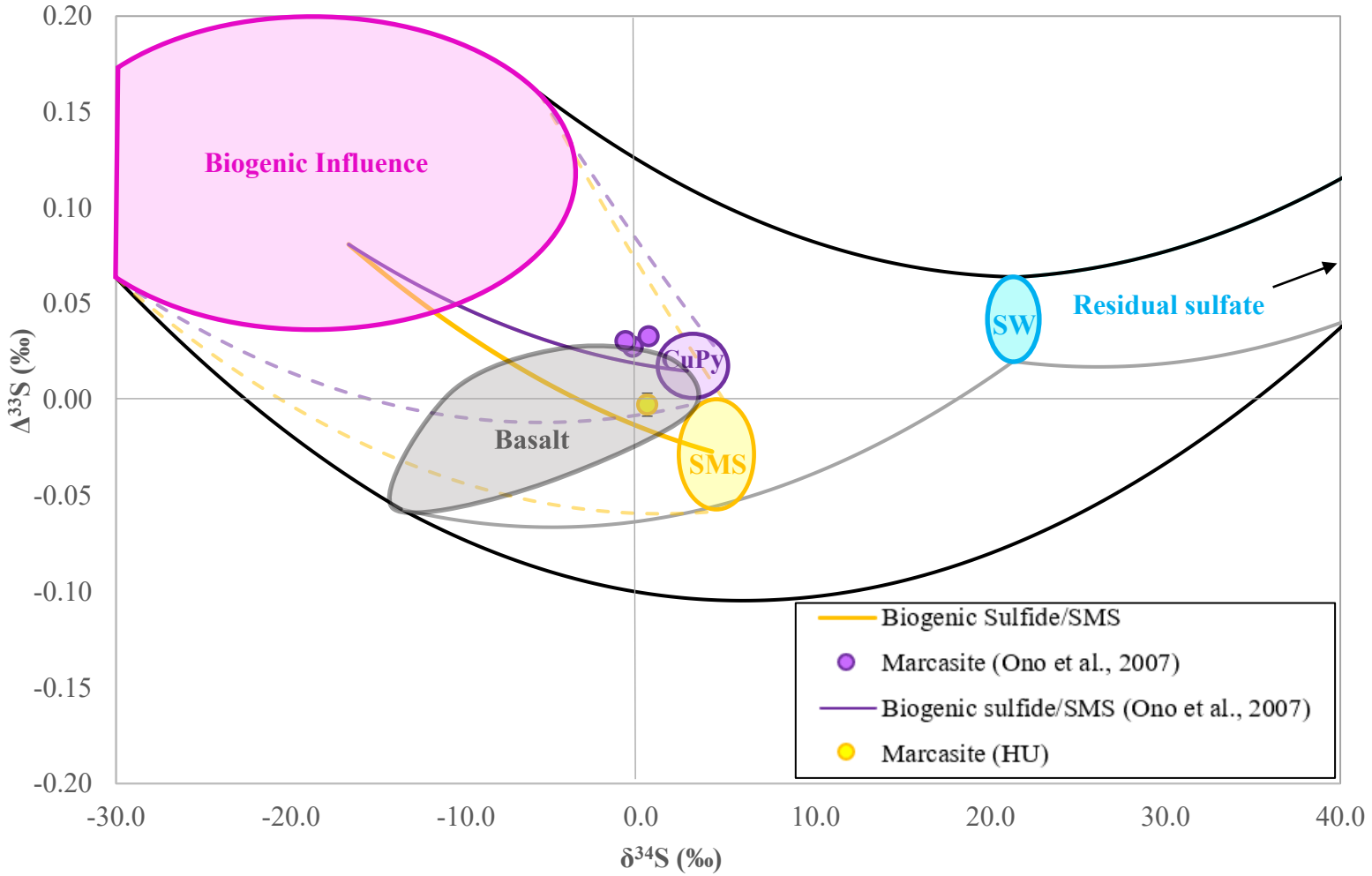


Figure 4.12: Marcasite data from this study and Ono et al. (2007) with corresponding mixing curves between averaged values for sulfide samples from MEF (this study), CuPy from Lucky Strike (Ono et al., 2007) and biogenic sulfide (Peters et al., 2010; Peters et al., 2011; Tostevin et al, 2014; Johnston et al., 2014). Error bars are 1σ.

#### 4.3.3.2 Push Core Sediment Samples

##### 4.3.3.2.1 Core Sample J2-1102-2-PC1-WC

Core sample J2-1102-2-PC1-WC, was collected from the axial valley floor at Endeavour. The core is composed of turbiditic sediment and significant hydrothermal plume fallout (Table 2.1), has a $\delta^{34}S$ value of 3.6‰ ±0.2‰ (1σ) that overlaps with previously reported vent fluid $H_2S$ $\delta^{34}S$ values reported from Endeavour (3.8‰ to 5.0‰) (Shanks et al., 1995; Hannington et al., 2005). Sulfide minerals present in the sample have an average $\Delta^{33}S$ value (-0.011‰) within the range of other SMS samples measured at Endeavour (Fig. 4.13) and thus likely represent the direct product of hydrothermal plume fallout. However, the S isotope value also falls along the trend of a mixing curve between the average (excluding marcasite) Endeavour sulfide S isotope signatures presented in this thesis ($\delta^{34}S$: 3.9‰; $\Delta^{33}S$: -0.026‰) and average biogenic sulfide, as described for the marcasite sample (Section 4.3.3.1) and illustrated in Figure 4.13. Accordingly, the sulfide present in the sample may be product of mixing between minor biogenic sulfide and primary hydrothermal plume fallout. Again, the very wide range in S isotopic values of possible biogenic S leaves a wide envelope of uncertainty on these models and no convincing conclusion for sulfur source can be drawn.

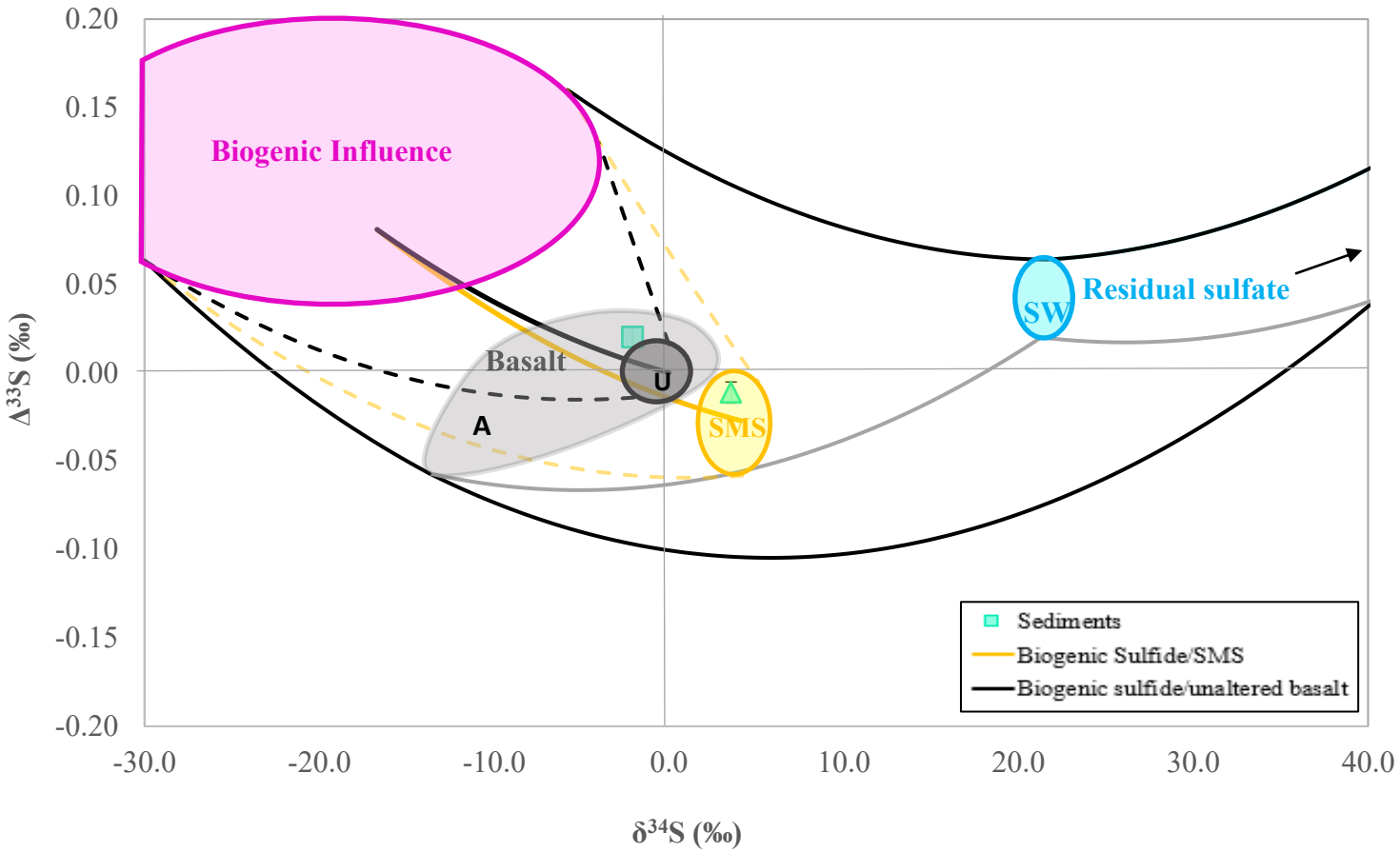


Figure 4.13: Sediment data from this study and mixing curves between averaged values (excluding marcasite) Endeavour sulfide samples (this thesis) and unaltered basalt with biogenic sulfide. Pyroclast containing sediment sample (J2-1101-9-PC1-B) is denoted by a square, while the sample rich in plume fallout (J2-1102-2-PC1-WC) is denoted by a triangle. Error bars are 1σ (Averaged S reservoir data from: Peters et al., 2010; Peters et al., 2011; Eickmann et al., 2014; Ono et al., 2007; Ono et al., 2012; Tostevin et al, 2014; Johnston et al., 2014).

#### 4.3.3.2.2 Core Sample J2-1101-9-PC1-B

Core sample J2-1101-9-PC1-B, collected from just outside the axial valley, west of MEF, is composed of a mix of turbiditic sediment and basaltic pyroclasts (Table 2.1), and had an negative $\delta^{34}S$ value of -2.1‰ and a slightly positive $\Delta^{33}S$ value of 0.020‰. These values fall within the range of altered basalt (Fig. 4.13). While sulfide grains were not visible in the sample via a stereomicroscope, a minor biogenic sulfide component is likely present, as indicated by the negative $\delta^{34}S$ values. However, the S isotope signature also falls along a mixing curve between unaltered basalt and biogenic sulfide (Fig. 4.13). As such, the S isotope signature was likely produced via the dual influence of the basaltic pyroclasts, which would be expected to contribute near-zero isotope values for both $\Delta^{33}S$ and $\delta^{34}S$, and the sediment, which would be expected to contribute positive $\Delta^{33}S$ values and negative $\delta^{34}S$ values.

The S isotope signature from core sample J2-1101-9-PC1-B further illustrates the difficulty in distinguishing between the different potential microbial influences in hydrothermal fluids and related SMS deposits at submarine hydrothermal systems (i.e., microbial presence in buried sediment at basalt hosted systems versus direct microbial alteration of basalt). Separate S isotope analyses of the turbiditic sediments and pyroclastic debris may enable confirmation of the potential dual source contributing to the S isotope value of the sediment.

# 5. Summary

## 5.1 Findings

New multiple S isotope data from sulfides and sulfates sampled at three sites of the JdFR (Middle Valley, Axial Volcano, Endeavour) have resulted in a refined understanding of hydrothermal processes at this site, which are also relevant to the application of multiple S isotopes as a tool for constraining S cycling in other modern submarine hydrothermal systems. A summary of the key findings based on this work is:

1. Models used to illustrate S mixing in hydrothermal systems must include the full extent of S isotopic data observed for each S reservoir (in conjunction with fixed endmember values) for the most comprehensive interpretation of the data that considers the range and possible isotopic values of the endmember source reservoirs.
2. When a full range of S isotope values of a reservoir are considered, one of the core hypotheses of this study, that entrainment of microbial sulfide would uniquely generate S isotope signatures with negative $\delta^{34}S$ values and positive $\Delta^{33}S$ values at sedimented sites, is rejected. In fact, the opposite appears to be true. Biogenic sulfide is fixed in the subsurface at temperatures high enough for anaerobic hyperthermophilic sulfate reducing bacteria to thrive (>80°C) (Butterfield et al., 2004), but too low to readily dissolve iron sulfide (<150°C) (Giggenbach, 1974), thereby removing light isotopes from the hydrothermal fluid during cycling.

3. Axial Volcano does not exhibit the same two-component S reservoir mixing typical of other active volcanic sediment-free MOR hydrothermal sites. This may be due to influence from one or more of the following: a) $SO_2$ disproportionation; b) microbial altered basalt due to thermophilic and hyperthermophilic sulfate reducing bacteria present in the subseafloor; c) entrainment of residual sulfate from MSR. The source models presented in this study cannot distinguish between these different processes.
4. Hydrothermal S isotope signatures at Endeavour exhibit both EPR-type two component mixing, as well as a larger range of $\Delta^{33}S$ values indicative of microbial influence (i.e., altered basalt or residual sulfate). It is possible that the microbial influence could be caused by pockets of buried sediment overlain by later basalt flows, but isotopic results are not conclusive.
5. Multiple sulfur isotopes alone do not provide a diagnostic tool for identifying buried sediment at submarine hydrothermal sites, as the isotopic signature of reduced sulfur in sediment is indistinguishable from microbially altered basalt, both of which can result in residual sulfate incorporation and produce sulfide S isotope signatures with negative $\Delta^{33}S$ values.
6. Marcasite is isotopically lighter than other sulfide samples analyzed in this study. Though the near-zero $\delta^{34}S$ and $\Delta^{33}S$ values are consistent with basalt-derived S, contextual observations (i.e., well constrained isotopically heavy hydrothermal fluid at the site; similar discordance between marcasite and other related SMS mineral samples reported in Ono et al. [2007]) indicate other processes may be contributing to the S isotope signatures of some iron

disulfides. These discordances may be due to biogenic $S^0$ mixing with hydrothermal fluid FeS to produce near zero multiple S isotope signatures.

7. Pyroclast and plume fallout containing push core sediments from Endeavour are representative of two-component mixing between their respective components. The plume fallout sample falls along a mixing curve between average biogenic sedimentary sulfide from Peters et al. (2010) and (2011) and Endeavour sulfide from this thesis. Similarly, the pyroclast-containing sample falls along a mixing curve between biogenic sedimentary sulfide (Peters et al., 2010; Peters et al., 2011) and unaltered basalt.

## 5.2 Recommendations

Though the use of the V-CDT scale produced repeatable intralaboratory results, data normalization with respect to the V-CDT scale remains inconsistent between laboratories and results in minor offsets between data sets. This offset highlights the need for the scientific community to establish an internationally agreed upon value for $\delta^{33}S$ with respect to V-CDT. If a consensus cannot be reached regarding the multiple S isotopic value of IAEA S-1, it may be necessary to adopt new standardization (e.g., Geng et al., 2019) and normalization procedures (e.g., Paul et al., 2007) for improved accuracy and precision of future studies. This study also illustrates the importance of reporting IAEA S-1 $\delta^{33}S$ values for future normalizations to different standardization scales.

## 5.3 Future Research

Future multiple S isotope research stemming from this study should focus on a broader system-scale approach through multi-faceted investigations of S isotopes signatures coupled with regional mapping of hydrothermal systems at various tectonic settings. Future research should involve analyzing hydrothermal fluids, volcanic host rocks, and sediments, rather than focusing solely on hydrothermal sulfide deposits. Constraining these endmember S reservoirs will allow for more refined endmember components for multi-component mixing models. Additional multiple S isotope analyses should be conducted on samples from the East Pacific Rise in order to build upon the data set by Ono et al. (2007) and further constrain two-component mixing between seawater sulfate and basalt, as well as at Endeavour in order to map potential locations of subseafloor geological anomalies. It is recommended that future studies apply other methods (e.g., hydrothermal fluid geochemistry), in conjunction with multiple S isotopes, in order to constrain differences in subseafloor geologic composition potentially indicative of buried sediment and/or altered basalt.

## 5.4 Conclusions

Multiple S isotope analyses were conducted on SMS deposit samples collected from three different hydrothermal vent fields along the Juan de Fuca Ridge in order to constrain variations in hydrothermal fluid cycling and related sulfide mineral precipitation between sedimented and sediment-free MOR environments. Unexpected standardization issues during analyses led to a review of standard use and normalization procedures for multiple

S isotope studies in modern systems. New models were developed to encompass the full range of S reservoirs affecting submarine hydrothermal vent systems in a $\Delta^{33}S$ versus $\delta^{34}S$ framework, enabling more accurate interpretations of the contributions of different sources and fractionation processes to S cycling within hydrothermal systems. At Middle Valley, S isotope signatures are indicative of significant microbial influence, but the signatures indicate an altered basalt and/or residual sulfate source as opposed to the originally hypothesized biogenic sulfide entrainment. Despite being a sediment-free active MOR volcano, Axial Volcano S isotope signatures do not exhibit EPR-type two-component mixing between seawater sulfate and basalt as originally hypothesized. There is evidence that negative $\Delta^{33}S$ values from sulfide deposits at Axial may indicate a variety of processes, including microbial influence (residual sulfate, altered basalt) and/or $SO_2$ disproportionation. Analyses of additional sedimented and sediment-free hydrothermal systems will be required to establish endmember S isotope signatures for each respective substrate.

As expected, Endeavour S isotope signatures exhibit a mix of values between Axial and Middle Valley. Some samples are indicative of EPR-type two component mixing, while others likely have a microbial S source. Samples showing evidence of a microbial influence could potentially be indicative of a sedimentary source, supporting the theory that buried sediment is present underneath later stage basaltic flows at Endeavour. However, this interpretation is not definitive as it is impossible to distinguish between chemolithoautotrophic MSR supported by basalt and heterotrophic MSR supported by organic rich sediments.

The analysis and interpretations presented in this study are based on a limited sample set from just one mid-ocean ridge. Thus, caution must be applied to the interpretations presented here. The analysis of more samples from additional submarine hydrothermal vent systems related to a wider range of geological contexts would provide greater constraints on the compositions of the various S reservoirs outlined in this study, and thus greater reliability for the interpretations presented here.

## References


Adshead, J.D., 1996, Stable isotopes, $^{14}C$ dating, and geochemical characteristics of carbonate nodules and sediment from an active vent field, northern Juan de Fuca Ridge, Northeast Pacific: Chemical Geology, v. 129, p. 133-152.

Ames, D.E., Franklin, J.M., and Hannington, M.D., 1993, Mineralogy and geochemistry of active and inactive chimneys and massive sulfide, Middle Valley, northern Juan de Fuca Ridge; an evolving hydrothermal system: Canadian Mineralogist, v. 31, p. 997-1024.

Antonelli, M.A., Kim, S-T., Peters, M., Labidi, J., Cartigny, P., Walker, R.J., Lyons, J.R., Hoek, J., and Farquhar, J., 2014, Early inner solar system origin for anomalous sulfur isotopes in differentiated protoplanets: Proceedings of the National Academy of Sciences of the United States of America, v. 111, p. 17749-17754.

Axial Seamount Hydrothermal Emissions Study (ASHES), 1986, Pisces submersible exploration of a high-temperature vent field in the caldera of Axial Seamount, Juan de Fuca Ridge: Eos Transactions American Geophysical Union, v. 67, p. 1027.

Baker, E.T., Lavelle, J.W., and Massoth, G.J., 1985, Hydrothermal particle plumes over the southern Juan de Fuca Ridge: Nature, v. 316, p. 342–344.

Barr, S.M, and Chase, R.L., 1974, Geology of the Northern End of Juan de Fuca Ridge and Sea-Floor Spreading: Canadian Journal of Earth Sciences, v. 1l, p. 1384-1406, doi: /10.1139/e74-134.

Beaudoin, G., Taylor, B.E., Rumble, III, D., and Thiemens, M., 1994, Variations in the sulfur isotope composition of troilite from the Cañon Diablo iron meteorite: Geochimica et Cosmochimica Acta, v. 58, p. 4253-4255.

Bilenker, L.D., Romano, G.Y., and McKibben, M.A., 2016, Kinetics of sulfide mineral oxidation in seawater: Implications for acid generation during in situ mining of seafloor hydrothermal vent deposits: Applied Geochemistry, v.75, p. 20-31.

Bischoff, J.L., and Rosenbauer, R.J., 1988, Liquid-vapor relations in the critical region of the system NaCl-H2O from 380 to 415°C: A refined determination of the critical

point and two-phase boundary of seawater: Geochemica et Cosmochimica Acta, v. 52, p. 2121-2126, doi: 10.1016/0016-7037(88)90192-5.

Bischoff, J.L., and Seyfried, W.E., 1978. Hydrothermal chemistry of seawater from 25-degrees-C to 350-degrees-C: American Journal of Science, v. 278, p. 838–860.

Blowes, D.W., Ptacek, C.J., Jambor, J.L., and Weisener, C.G., 2003, The Geochemistry of Acid Mine Drainage: Treatise on Geochemistry, v. 9, p. 149-204.

Butterfield, D.A., Massoth, G.J., McDuff, R.E., Lupton, J.E., and Lilley, M.D., 1990, Geochemistry of hydrothermal fluids from Axial Seamount hydrothermal emissions study vent field, Juan de Fuca Ridge: Subseafloor boiling and subsequent fluid-rock interaction: Journal of Geophysical Research, v. 95, p.12895.

Butterfield, D.A., McDuff, R.E., Franklin, J.M., and Wheat, C.G., 1994, Geochemistry of hydrothermal vent fluids from Middle Valley, Juan de Fuca Ridge: Proceedings of the Ocean Drilling Program, Scientific Results, v. 139, p. 395–410.

Butterfield, D.A., Roe, K.K., Lilley, M.D., Huber, J.A., Baross, J.A., Embley, R.W., and Massoth, G.J., 2004, Mixing, Reaction and Microbial Activity in the Sub-seafloor Revealed by Temporal and Spatial Variation in Diffuse Flow Vents at Axial Volcano: The Subseafloor Biosphere at Mid-Ocean Ridges, Geophysical Monograph, v. 144, p. 267-285.

Canadian American Seamount Expedition (CASM), 1985, Hydrothermal vents on an axial seamount on the Juan de Fuca Ridge: Nature, v. 313, p. 212-24.

Canfield, D.E., 2001, Biogeochemistry of sulfur isotopes: Reviews in Mineralogy and Geochemistry, v.43, p. 607–636, doi: https://doi.org/10.2138/gsrmg.43.1.607.

Canfield, D.E., Raiswell, R., Westrich, J.T., Reaves, C.M., and Berner, R.A., 1986, The use of chromium reduction in the analysis of reduced inorganic sulfur in sediments and shales: Chemical Geology, v. 54, p. 149-155.

Carbotte, S.M., Detrick, R.S., Harding, A., Canales, J.P., Babcock, J., Kent, G., Van Ark, E., Nedimovic, M., and Diebold, J., 2006, Rift topography linked to magmatism at the intermediate spreading Juan de Fuca Ridge: Geology, v. 34, p. 209–212.

Carbotte, S.M., Canales, J.P., Nedimovic, M.R., Carton, H., and Mutter, J.C., 2012, Recent seismic studies at the East Pacific Rise 8˚ 20'- 10˚ 10' N and Endeavour Segment

insights into mid-ocean ridge hydrothermal and magmatic processes: Oceanography, v. 25, p. 100–112.

Chadwick, J., Perfit, M., Ridley I., Jonasson, I., Kamenov, G., Chadwick, W., Embley, R., le Roux, P., and Smith, M., 2005, Magmatic effects of the Cobb hot spot on the Juan de Fuca Ridge: Journal of Geophysical Research, v. 110, doi:10.1029/2003JB002767.

Chadwick, W.W, Nooner, S.L., Butterfield, D.A., Lilley, M.D., Clague, D.A., Caress, D.W., Dziak, R.P., and Haxel, J.H., 2011, Discovery of the 2011 eruption at Axial Seamount: American Geophysical Union Fall Meeting, v. 2011.

Chadwick, W.W., Clague, D.A., Embley, R.W., Perfit, M.R., Butterfield, D.A., Caress, D.W., Paduan, J.B., Martin, J.F., Sasnett, P., Merle, S.G., and Bobbitt, A.M., 2013, The 1998 eruption of Axial Seamount: New insights on submarine lava flow emplacement from high-resolution mapping: Geochemistry, Geophysics, Geosystems, v. 14, p. 3939-3968.

Chadwick, W.W., Devaney, R., Collasius, T., Yoerger, D., and Bobbitt, A., 2015, Axial 2015 Cruise Report, R/V Thompson TN327, JASON Dives J2-820 – J2-826, August 14-29, 2015, p. 29.

Chadwick, W., Embley, R., Clague, D., and Butterfield, D., 2015, Processed Swath Bathymetry Grids (NetCDF:GMT format) derived from Multibeam Sonar Data from the Juan de Fuca - Axial Seamount assembled as part of the JdF_Gorda: NOAA_VENTS Data Compilation. Interdisciplinary Earth Data Alliance (IEDA), doi:10.1594/IEDA/317691.

Charlou, J.L. and Donval, J.P., 1993, Hydrothermal methane venting between 12°N and 26°N along the Mid-Atlantic Ridge: Journal of Geophysical Research, v. 98, p. 9625–9642.

Clague, D.A., Caress, D.W., Thomas, H., Thompson, D., Calarco, M., Holden, J., and Butterfield, D., 2008, Abundance and distribution of hydrothermal chimneys and mounds on the Endeavour Ridge determined by 1-m resolution AUV multibeam

mapping surveys: Eos Transactions American Geophysical Union, v. 89, Fall Meeting Supplement Abstract V41B-2079.

Clague, D., and Caress, D., 2015, Processed Near-bottom Multibeam Sonar Data from the Juan de Fuca Spreading Center - Endeavour Segment acquired during the Zephyr expedition ZPR1108 (2011): Interdisciplinary Earth Data Alliance (IEDA), doi:10.1594/IEDA/321986.

Coplen, T.B., and Krouse, H.R., 1998, Sulphur isotope data consistency improved: Nature, v. 392, p. 32, doi:10.1038/32080.

Cousens, B.L., Blenkinsop, J., and Franklin, J.M., Lead isotope systematics of sulfide minerals in the Middle Valley hydrothermal system, northern Juan de Fuca Ridge: Geochemistry, Geophysics, Geosystems, v. 3, p. 1-16, doi: 10.1029/2002GC000257.

Crowe, D.E., and Valley, J.W., 1992, Laser microprobe study of sulfur isotope variation in a sea-floor hydrothermal spire, Axial Seamount, Juan de Fuca Ridge, eastern Pacific: Chemical Geology (Isotope Geoscience Section), v. 101, p. 63-70.

Cruse, A.M., Seewald, J.S., Saccocia, P.J., and Zierenberg, R., 2008, Hydrothermal Fluid Composition at Middle Valley, Northern Juan de Fuca Ridge: Temporal and Spatial Variability: Geophysical Monograph Series, v. 178, doi:10.1029/178GM08.

Davis, E.E., Mottl, M.J., Fisher, A.T., and Shipboard Scientific Party, 1992a, Introduction: Proceedings of the Ocean Drilling Program, Initial Reports, v. 139, p. 5-7.

Davis, E.E., Mottl, M.J., Fisher, A.T., and Shipboard Scientific Party, 1992b, Site 856: Proceedings of the Ocean Drilling Program, Initial Reports, v. 139, p. 161-281.

Davis, E.E., Mottl, M.J., Fisher, A.T., and Shipboard Scientific Party, 1992c, Site 858: Proceedings of the Ocean Drilling Program, Initial Reports, v. 139, p. 431-569.

Davis, E.E., and Villinger, H., 1992, Tectonic and thermal structure of the Middle Valley sedimented rift, Northern Juan de Fuca Ridge: Proceedings of the Ocean Drilling Program, Initial Reports, v. 139, p. 9-41.

Davis E.E., and Fisher, A.T., 1994, On the nature and consequences of hydrothermal circulation in the Middle Valley sedimented rift: inferences from geophysical and

geochemical observations, Leg 139: Proceedings of the Ocean Drilling Program, Scientific Results, v. 139, p. 695-717.

Desbruyères, D., Gaill, F., Laubier, L., and Fouquet, Y., 1985, Polychaetous annelids from hydrothermal vent ecosystems: An ecological overview: Biological Society of Washington Bulletin 6, p. 103-116.

Delaney, J.R., McDuff, R.E., and Lupton, J.E., 1984, Hydrothermal fluid temperatures of 400 °C on the Endeavour Segment, northern Juan de Fuca Ridge: Eos Transactions American Geophysical Union, Fall Meeting Supplement v., 65, p. 973.

Delaney, J.R., Robigou, V., McDuff, R.E., and Tivey, M.K., 1992, Geology of a vigorous hydrothermal system on the Endeavour Segment Juan de Fuca Ridge: Journal of Geophysical Research: Solid Earth, v. 97, p. 19663–19682.

Delaney, J.R., 2015, The first-ever detection and tracking of a mid-ocean ridge volcanic eruption using the recently completed, NSF-funded, submarine fiber-optic network in the Juan de Fuca region: American Geophysical Union Fall Meeting, v. 2015.

Ding, T., Valkiers, S., Kipphardt, H., De Bievre, P., Taylor, P.D.P., Gonfiantini, R., and Krouse, R., 2001, Calibrated sulfur isotope abundance ratios of three IAEA sulfur isotope reference materials and V-CDT with a reassessment of the atomic weight of sulfur: Geochimica et Cosmochimica Acta, v. 65, p. 2433-2437.

Divins, D.L., 2003, Total Sediment Thickness of the World's Oceans & Marginal Seas: NOAA National Geophysical Data Center, Boulder, CO.

Duckworth, R.C., Fallick, A.E., and Rickard, D., 1994, Mineralogy and sulfur isotopic composition of the Middle Valley massive sulfide deposit, northern Juan de Fuca Ridge: Proceedings of the Ocean Drilling Program, Scientific Results, v. 139, p. 373-385.

Edmond, J.M., Measures, C., McDuff, R.E., Chan, L.H., Collier, R., Grant, B., Gordon, L.I., and Corliss, J.B., 1979, Ridge crest hydrothermal activity and the balances of the major and minor elements in the ocean: The Galapagos data: Earth and Planetary Science Letters, v. 46, p. 1–18, doi: 10.1016/0012-821X(79)90061-X.

Eickmann, B., Thorseth, I.H., Peters, M., Strauss, H., Brocker, M., and Pedersen, R.B., 2014, Barite in hydrothermal environments as a recorder of subseafloor processes: a multiple-isotope study from the Loki's Castle vent field: Geobiology, v. 12, p. 308-321.

Elderfield, H., Wheat, C.G., Mottl, M.J., Monnin, C., and Spiro, B., 1999, Fluid and geochemical transport through oceanic crust: a transect across the eastern flank of the Juan de Fuca Ridge: Earth and Planetary Science Letters, v. 172, p. 151–165, doi: 10.1016/S0012-821X(99)00191-0.

Embley, R.W., Murphy, K.M., and Fox, C.G., 1990, High-resolution studies of the summit of Axial volcano: Journal of Geophysical Research, v. 95, p. 12, 785–12,812.

Embley, R.W., Chadwick, W.W., Clague, D.A., and Stakes, D., 1999, 1998 eruption of Axial Volcano; multibeam anomalies and seafloor observations: Geophysical Research Letters, v. 26, p. 3425-3428, doi: 10.1029/1999GL002328.

Endeavour-Axial Geochemistry and Ecology Research (EAGER), 2009, R/V Atlantis – DSV Alvin AT15-47 Cruise to the Endeavour Segment and Axial Volcano on the Juan de Fuca Ridge, Northeast Pacific Ocean, June 13 – 27.

Farquhar, J., Bao, H.M., and Thiemens, M., 2000, Atmospheric influence of Earth's earliest sulfur cycle: Science, v. 289, p. 756–758.

Farquhar, J., Johnston, D.T., Wing, B.A., Habicht, K.S., Canfield, D.E., Airieau, S., Thiemens, M.H., 2003, Multiple sulphur isotopic interpretations of biosynthetic pathways; implications for biological signatures in the sulphur isotope record: Geobiology, v. 1, p. 27–36.

Farquhar, J., and Wing, B., 2003, Multiple sulfur isotopes and the evolution of the atmosphere: Earth and Planetary Science Letters, v. 213, p. 1-13.

Farquhar, J., Johnston, D.T., and Wing, B.A., 2007, Implications of conservation of mass effects on mass-dependent isotope fractionations: Influence of network structure on sulfur isotope phase space of dissimilatory sulfate reduction: Geochimica et Cosmochimica Acta, v. 71, p. 5862–5875.

Feely, R.A., Gendron, J.F., Baker, E.T., and Lebon, G.T., 1994, Hydrothermal plumes along the East Pacific Rise, 8-degrees-400 to 11-degrees-500N - Particle distribution and composition: Earth and Planetary Science Letters, v. 128, p. 19–36.

Fisher, A., Langseth, M., Baker, P., Ryan, W., Stein, J., Glenn, S., Shultheiss, P., Zierenberg, R., Iturrino, G., Jin, W., Darlington, E., Goodfellow, W., Daniel, D. N., Conly, A., Cross, S., Grove, M., and Cramer, B., 1997, The devil's in the details: Fine-scale hydrogeology of areas of active venting in Middle Valley, northern Juan de Fuca Ridge: Eos (Transactions, American Geophysical Union), v. 78, p. 165–170.

Forrest, J., and Newman, L., 1977, Silver-110 microgram sulfate analysis for the short time resolution of ambient levels of sulfur aerosol: Analytical Chemistry, v. 49, p. 1579–1584.

Fouquet, Y., Zierenberg, R.A., Miller, D.J., and Shipboard Scientific Party, 1998, Middle Valley: Bent Hill area (Site 1035): Proceedings of the Ocean Drilling Program, Initial Reports, v. 169, p. 35-152.

Gamo, T., Okamura, K., Charlou, J.L., Urabe, T., Auzende, J.M., Ishibashi J., Shitashima, K., and Chiba, H., 1997, Acidic and sulfate-rich hydrothermal fluids from the Manus Back-Arc Basin, Papua New Guinea: Geology, v. 25, p. 139–142.

Gao, X., and Thiemens, M.H., 1991, Systematic study of sulfur isotopic composition in iron meteorites and the occurrence of excess 33S and 36S: Geochimica et Cosmochimica Acta, v. 55, p. 2671–2679.

Geng, L., Savarino, J., Caillon, N., Gautier, E., Farquhar, J., Dottin, III, J.W., Magalh˜aes, N., Hattori, S., Ishino, S., Yoshida, N., Albar`ede,F., Albalat, E., Cartigny, P., Ono, S., and Thiemens, M.H., 2019, Intercomparison measurements of two $^{33}S$ enriched sulfur isotope standards: Journal of Analytical Atomic Spectrometry, v. 34, p. 1263-1271.

Giggenbach, W.F., 1974, Equilibria involving polysulfide ions in aqueous sulfide solutions up to 240°: Inorganic Chemistry, v. 13, p. 1724–1730.

Glickson, D.A., Kelley, D.S., and Delaney, J.R., 2006, The Sasquatch Hydrothermal Field: Linkages Between Seismic Activity, Hydrothermal Flow, and Geology: American Geophysical Union Fall Meeting Abstracts.

Glickson, D.A., Kelley, D.S., and Delaney, J.R., 2007, Geology and hydrothermal evolution of the Mothra Hydrothermal Field, Endeavour Segment, Juan de Fuca Ridge: Geochemistry, Geophysics Geosystems, v. 8, doi: 10.1029/2007GC001588.

Goodfellow, W.D., and Blaise, B., 1988, Sulfide formation and hydrothermal alteration of hemipelagic sediment in Middle Valley, Northern Juan de Fuca Ridge: Canadian Mineralogist, v. 26, p. 675-696.

Goodfellow, W.D., and Franklin, J.M., 1993, Geology, Mineralogy, and Chemistry of Sediment-Hosted Clastic Massive Sulfides in Shallow Cores, Middle Valley, Northern Juan de Fuca Ridge: Economic Geology, v. 88, p. 2037-2068.

Golden, C.E., Webb, S.C., and Sohn, R.A., 2003, Hydrothermal microearthquake swarms beneath active vents at Middle Valley, northern Juan de Fuca Ridge: Journal of Geophysical Research, v. 108, p. 2027.

Goldstein, S.J., Murrell, M.T., Janecky, D.R., Delaney, J.R., and Clague, D.A., 1991, Geochronology and petrogenesis of MORB from the Juan de Fuca and Gorda Ridges by U-238 Th-230 disequilibrium, Earth and Planetary Science Letters, v. 107, p. 25–41.

Hannington, M.D., and Scott, S.D., 1988, Mineralogy and geochemistry of a hydrothermal silica-sulfide-sulfate spire in the caldera of Axial Seamount, Juan De Fuca Ridge: Canadian Mineralogist, Canada, v. 26, p. 603-625.

Hannington, M.D., Jonasson, I.R., Herzig, P.M., and Peterson, S., 1995, Physical and Chemical Processes of Seafloor Mineralization at Mid-Ocean Ridges: Geophysical monograph, v. 91, p. 115-157.

Hannington, M.D., de Ronde, C.E.J., and Peterson, S., 2005, Sea-Floor Tectonics and Submarine Hydrothermal Systems: Economic Geology, 100th Anniversary Volume, p. 111–141.

Hannington, M.D., Petersen, S., Herzig, P.M., and Jonasson, I.R., 2004, A global database of seafloor hydrothermal systems, including a digital database of geochemical analyses of seafloor polymetallic sulfides: Geological Survey of Canada Open File 4598, CD-ROM.

Hannington, M., Jamieson, J., Monecke, T., Petersen, S., Beaulieu, S., 2011, The Abundance of Seafloor Massive Sulfide Deposits: Geology, v. 39, p. 1155-1158.

Helo, C., Clague, D.A., and Stix, J., 2008, Pyroclastic eruptions from Axial Caldera, Juan de Fuca Ridge, NE Pacific Ocean, 8 IOP Conf. Ser.: Earth and Environmental Science 3 012005, doi:10.1088/1755-1307/3/1/012005.

Helo, C., Longpre, M.A., Shimizu, N., Clague, D.A., and Stix, J., 2011, Explosive eruptions at mid-ocean ridges driven by $CO_2$-rich magmas: Nature Geoscience, v. 4, p. 260-263.

Holden, J.F., Di Iorio, D., Butterfield, D.A., and Clague, D., 2008, R/V Atlantis – DSV Alvin AT15-36 Cruise to the Endeavour Segment and Axial Volcano Juan de Fuca Ridge, Northeast Pacific Ocean, August 18 – September 7.

Holland, H., 1965 Some applications of thermochemical data to problems of ore deposits; Part 2, Mineral assemblages and the composition of ore forming fluids: Economic Geology, v. 60, p. 1101–1166.

Hulston, J.R., and Thode, H.G. 1965a, Variations in 33S, 34S and 36S, contents of meteorites and their relation to chemical and nuclear effects: Journal of Geophysical Research, v. 70, p. 3475-3484.

Hulston, J.R. and Thode, H.G., 1965b, Cosmic-ray-produced 36S and 33S in metallic phase of iron meteorites: Journal of Geophysical Research, v. 70, p. 4435-4442.

Jaeschke, A., Eickmann, B., Lang, S.Q., Bernasconi, S.M., Strauss, H., and Fru¨h-Green, G.L., 2014, Biosignatures in chimney structures and sediment from the Loki's Castle low-temperature hydrothermal vent field at the Arctic Mid-Ocean Ridge, Extremophiles, v. 18, p. 545-560.

Jambor, J.L., 1994, Mineralogy of sulfide-rich tailings and their oxidation products: Mineralogical Association of Canada Short Course Handbook, v.22, p. 59-102.

Jamieson, J.W., 2005, Tracing sulfur sources in an Archean hydrothermal system using sulfur multiple isotopes–A case study from the Kidd Creek volcanogenic massive sulfide deposit [M.Sc. thesis]: University of Maryland, p. 40.

Jamieson, J.W., Hannington, M.D., and Farquhar, J., 2006, Evaluating isotopic equilibrium among sulfide mineral pairs in Archean ore deposits: case study from the Kidd Creek VMS deposit, Ontario, Canada: Economic Geology, v. 101, p. 1055–1061.

Jamieson, J.W., Hannington, M.D., Clague, D.A., Kelley, D.S., Delaney, J.R., Holden, J.F., Tivey, M.K., and Kimpe, L.E., 2013a, Sulfide geochronology along the Endeavour Segment of the Juan de Fuca Ridge: Geochemistry, Geophysics, Geosystems, v. 14,7, p. 2084-2099, doi: 10.1002/ggge.20133.

Jamieson, J.W., Wing, B.A., Farquhar, J., and Hannington, M.D., 2013b, Neoarchaean seawater sulphate concentrations from sulphur isotopes in massive sulphide ore: Nature Geoscience, v. 6, p. 61-64, doi: 10.1038/NGEO1647.

Jamieson, J.W., Clague, D.A., and Hannington, M.D., 2014, Hydrothermal sulfide accumulation along the Endeavour Segment, Juan de Fuca Ridge: Earth and Planetary Science Letters, v. 395, p. 136–148, doi: 10.1016/j.epsl.2014.03.035.

Jamieson, J.W., Hannington, M.D., Tivey, M.K., Hansteen, T., and Williamson, N.M.B., Stewart, M., Fietzke, J., Butterfield, D., Frische, M., Allen, L., Cousens, B., and Langer, J., 2016a, Precipitation and Growth of Barite within Hydrothermal Vent Deposits from the Endeavour Segment, Juan de Fuca Ridge: Geochimica et Cosmochimica Acta, v. 173, p. 64-85.

Jamieson, J.W., Petersen, S., Bach, W., and Hannington, M.D., 2016b, Hydrothermalism: Encyclopedia of Marine Geosciences, doi: 10.1007/978-94-007-6644-0_15-1.

Janecky, D.R., and Seyfried, W.E., Jr., 1983, The solubility of magnesium-hydroxide-sulfate-hydrate in seawater at elevated temperatures and pressures: American Journal of Science, v. 283, p. 831–860.

Johnson, H.P., and Embley, R.W., 1990, Axial Seamount: An active ridge axis volcano on the central Juan de Fuca Ridge: Journal of Geophysical Research, v. 105, p. 12,689–12,696.

Johnson, H.P., Hutnak, M., Dziak, R.P., Fox, C.G., Urcuyo, I., Cowen, J.P., Nabelek, J., and Fisher, C., 2000, Earthquake induced changes in a hydrothermal system on the Juan de Fuca mid-ocean ridge, Nature, v. 407, p. 174–177.

Johnston, D.T., 2011, Multiple sulfur isotopes and the evolution of Earth's surface sulfur cycle: Earth-Science Reviews, v. 106, p. 161-183.

Johnston, D.T., Farquhar, J., Wing, B.A., Kaufman, A.J., Canfield, D.E., Habicht, K.S., 2005, Multiple sulfur isotope fractionations in biological systems: a case study with sulfate reducers and sulfur disproportionators: American Journal of Science, v. 305, p. 645–660.

Johnston, D.T., Gill, B.C., Masterson, A., Beirne, E., Casciotti, K.L., Knapp A.N., and Berelson, W., 2014, Placing an upper limit on cryptic marine sulphur cycling: Nature, v. 513, p. 530-533.

Juniper, S.K., Tunnicliffe, V., and Fontaine, A.R., 1988, Biological influences on mineral deposition at deep-sea hydrothermal vents: NOAA National Undersea Research Program Report 88-4, p. 99-118.

Juniper, S.K., Jonasson, I.R., Tunnicliffe, V., and Southward, A.J., 1992, Influence of a tube-building polychaete on hydrothermal chimney mineralization: Geology, v. 20, p. 895-898.

Kaplan, I.R., Rittenberg, S.C., 1964, Microbiological fractionation of sulphur isotopes: Journal of General Microbiology v. 34, p. 195–212.

Karsten, J.L., Hammond, S.R., and Davis, E.E., 1986, Detailed geomorphology and neotectonics of the Endeavour Segment, Juan de Fuca Ridge – new results from seabeam swath mapping: Geological Society of America Bulletin, v. 97, p. 213–221.

Kelley, D.S., Delaney, J.R., Lilley, M.D., and Butterfield, D.A., 2001a, Vent Field Distribution and Evolution Along the Endeavour Segment, Juan de Fuca Ridge: Eos Transactions American Geophysical Union, v. 82, Fall Meeting Supplement, Abstract OS21B-0439.

Kelley, D.S., Delaney, J.R., and Yoerger, D.R., 2001b, Geology and venting characteristics of the Mothra hydrothermal field, Endeavour segment, Juan de Fuca Ridge: Geology, v. 29, p. 959-962.

Kelley, D.S., Baross, J.A., and Delaney, J.R., 2002, Volcanoes, fluids, and life in submarine environments: Annual Reviews Earth and Planetary Sciences, v. 30, p. 385–491, doi: /10.1146/annurev.earth.30.091201.141331.

Kelley, D.S., Carbotte, S.M., Caress, D.W., Clague, D.A., Delaney, J.R., Gill, J.B., Hadaway, H., Holden, J.F., Hooft, E.E.E., Kellog, J.P., Lilley, M.D., Stoermer, M., Toomey, D., Weekly, R., and Wilcock, W.S.D., 2012, Endeavour Segment of the Juan de Fuca Ridge: One of the most remarkable places on Earth: Oceanography, v. 25, p. 44-61, doi: 10.5670/oceanog.2012.03.

Kelley, D.S., Delaney, J.R., and Juniper, S.K., 2014, Establishing a new era of submarine volcanic observatories: Cabling Axial Seamount and the Endeavour Segment of the Juan de Fuca Ridge: Marine Geology, v. 325, p. 426-450.

Kelley, D., Delaney, J., Yoerger, D., Caress, D., Clague, D., and Denny, A., 2015, Processed Gridded (ESRI ASCII format) Bathymetry Data from the Juan de Fuca Endeavour Segment assembled as part of the JdF: Endeavour_Bathymetry Data Compilation: Interdisciplinary Earth Data Alliance (IEDA), doi:10.1594/IEDA/321401.

Kim, J., Lee, I., and Lee, K.Y., 2004, S, Sr, and Pb isotopic systematics of hydrothermal chimney precipitates from the Eastern Manus Basin, western Pacific: Evaluation of magmatic contribution to hydrothermal system: Journal of Geophysical Research: Solid Earth, v. 109, doi: /10.1029/2003JB002912.

Kristall, B., Nielsen, D., Hannington, M.D., Kelley, D.S., and Delaney, J.R., 2011, Chemical microenvironments within sulfide structures from the Mothra Hydrothermal Field: Evidence from high-resolution zoning of trace elements: Chemical Geology, v. 290, p. 12–30.

Kurnosov, V., Murdmaa, I., Rosanova, T., Kashintzev, G., Eroshchev-Shak, V., and Krasnov, S., 1994, Mineralogy of hydrothermally altered sediments and igneous

rocks at Sites 856-858, Middle Valley, Juan de Fuca Ridge, Leg 139: Proceedings of the Ocean Drilling Program, Scientific Results, v. 139, p. 113-131.

Kusakabe, M., Komoda, Y., Takano, B., and Abiko, T., 2000, Sulfur isotopic effects in the disproportionation reaction of sulfur dioxide in hydrothermal fluids: implications for the d34S variations of dissolved bisulfate and elemental sulfur from active crater lakes: Journal of Volcanology and Geothermal Research, v. 97, p. 287–307.

Labidi, J., Cartigny, P., Hamelin, C., Moreira, M., and Dosso, L., 2014, Sulfur isotope budget ($^{32}S$, $^{33}S$, $^{34}S$ and $^{36}S$) in Pacific–Antarctic ridge basalts: A record of mantle source heterogeneity and hydrothermal sulfide assimilation: Geochimica et Cosmochimica Acta, v. 133, p. 47-67.

Lawrie, D., and Miller, D.J., 2000, Data report: Sulfide mineral chemistry and petrography from Bent Hill, ODP Mound, and Tag Massive Sulfide Deposits: Proceedings of the Ocean Drilling Program, Scientific Results, v. 169, p. 1-34.

Li, B., Shi, X., Li, C., Wang, J., Pei, Y., and Ye, J., 2016, Lead, Sulfur, and Oxygen Isotope Systematics in Hydrothermal Precipitates form the 14˚S Hydrothermal Field, South Mid-Atlantic Ridge: Resource Geology, v. 66, p. 274-285.

Lilley, M.D., Butterfield, D.A., Olsen, E.J., Lupton, J.E., Macko, S.A., and McDuff, R.E., 1993, Anomalous CH4 and NH4 + concentrations at an unsedimented mid-ocean ridge hydrothermal System: Nature, v. 364, p. 45–47, doi:10.1038/364045a0.

Lonsdale, P., 1977, Clustering of suspension-feeding macrobenthos near abyssal hydrothermal vents at oceanic spreading centers: Deep-Sea Research, v. 24, p. 857–863.

Machel, H.G., Krouse, H.R., and Sassen, R., 1995, Products and distinguishing criteria of bacterial and thermochemical sulfate reduction: Applied Geochemistry, v. 10, p. 373–389.

Masterson, A.L., 2016, Multiple Sulfur Isotope Applications in Diagenetic Models and Geochemical Proxy Records [Doctoral Dissertation]: Harvard University, Graduate School of Arts and Sciences.

Masterson, A.L., Wing, B.A., Paytan, A., Farquhar, J., and Johnston, D.T., 2016, The minor sulfur isotope composition of Cretaceous and Cenozoic seawater sulfate: Paleoceanography, v. 31, p. 779-788.

McManus, D.A., Holmes, M.L., Carson, B., and Barr, S.M, 1972, Late Quaternary tectonics, northern end of Juan de Fuca Ridge (northeast Pacific): Marine Geology, v. 12, p. 141-164.

McDermott, J.M., 2015, Geochemistry of deep-sea hydrothermal vent fluids from the Mid-Cayman Rise, Caribbean Sea [PhD Thesis]: Massachusetts Institute of Technology, p. 92.

McDermott, J.M., Ono, S., Tivey, M.K., Seewald, J.S., Shanks, III, W.C., and Solow, A.R., 2015, Identification of sulfur sources and isotopic equilibria in submarine hot-springs using multiple sulfur isotopes: Geochimica et Cosmochimica Acta, v. 150, p. 169-187.

McDermott, J.M., Sylva, S.P., Ono, S., German, C.R., and Seewald, J.S., 2018, Geochemistry of fluids from Earth's deepest ridge-crest hot-springs: Piccard hydrothermal field, Mid-Cayman Rise: Geochimica et Cosmochimica Acta, v. 228, p. 95-118.

Meier, D.V., Pjevac, P., Bach, W., Hourdez, S., Girguis, P.R., Vidoudez, C., Amann, R., and Meyerdierks, A., 2017, Niche partitioning of diverse sulfur-oxidizing bacteria at hydrothermal vents: Multidisciplinary Journal of Microbial Ecology, v. 11, p. 1545-1558.

Merle, S., 2015, Processed Swath Bathymetry Grids (NetCDF: GMT format) derived from Multibeam Sonar Data from the Juan de Fuca Focus Site: Ridge2000 assembled as part of the JdF_Gorda: NOAA_VENTS Data Compilation: Interdisciplinary Earth Data Alliance (IEDA), doi:10.1594/IEDA/317692.

Metz, S., and Trefry, J.H., 1993, Field and laboratory studies of metal uptake and release by hydrothermal precipitates: Journal of Geophysical Research-Solid Earth, v. 98, p. 9661–9666.

Miller, M.F., 2002, Isotopic fractionation and the quantification of $^{17}O$ anomalies in the oxygen three-isotope system; an appraisal and geochemical significance: Geochimica et Cosmochimica Acta, v. 66, p. 1881-1889.

Mottl, M.J., and McConachy, T.F., 1990, Chemical processes in buoyant hydrothermal plumes on the East Pacific Rise near 21-degrees-N: Geochimica et Cosmochimica Acta, v. 54, p. 1911–1927.

Frank, K.L., Rogers, D.R., Olins, H.C., Vidoudez, C., and Girguis, P.R., 2013, Characterizing the distribution and rates of microbial sulfate reduction at Middle Valley hydrothermal vents: The International Society for Microbial Ecology, v. 7, p., 1391-1401.

Ohmoto, H., 1972, Systematics of carbon and sulfur isotopes in hydrothermal ore deposits: Economic Geology, v. 67, p. 551-578.

Ono, S., Eigenbrode, J.L., Pavlov, A.A., Kharecha, P., Rumble, D., Kasting, J.F., and Freeman, K.H., 2003, New insights into Archean sulfur cycle from mass-independent sulfur isotope records from the Hamersley Basin, Australia: Earth and Planetary Science Letters, v. 213, p. 15-30.

Ono, S., Wing, B.A., Johnston, D., Farquhar, J., and Rumble, D., 2006, Mass-dependent fractionation of quadruple stable sulfur isotope system as a new tracer of sulfur biogeochemical cycles: Geochimica et Cosmochimica Acta, v. 70, p. 2238–2252.

Ono, S., Shanks, III, W.C., Rouxel, O.J., and Rumble, D., 2007, S-33 constraints on the seawater sulfate contribution in modern seafloor hydrothermal vent sulfides: Geochimica et Cosmochimica Acta, v. 71, p. 1170-1182.

Ono, S., Keller, N.S., Rouxel, O., and Alt, J.C., 2012, Sulfur-33 constraints on the origin of secondary pyrite in altered oceanic basement: Geochimica et Cosmochimica Acta, v. 87, p. 323–340.

Paradis, S., Jonasson, I.R., Le Cheminant, G.M., and Watkinson, D.H., 1988, Two zinc-rich chimneys from the plume site, southern Juan de Fuca: Canadian Mineralogist, v. 26, p. 637-654.

Paul, D., Skrzypek, G., and, Forizs, I., 2007, Normalization of measured stable isotopic compositions to isotope reference scales – a review: Rapid Communications in Mass Spectrometry, v. 21, p. 3006–3014.

Pellerin, A., Hao Bui, T., Rough, M., Mucci, A., Canfield, D.E., and Wing, B.A., 2015, Mass-dependent sulfur isotope fractionation during reoxidative sulfur cycling: A case study from Mangrove Lake, Bermuda: Geochimica et Cosmochimica Acta, v. 149, p. 152-164.

Peter, J.M., Goodfellow, W.D., Leybourne, M.I., 1994, Fluid Inclusion petrography and microthermometry of the Middle Valley hydrothermal system, Northern Juan de Fuca Ridge: Proceedings of the Ocean Drilling Program, Scientific Results, v. 139, p. 411-428.

Peters, M., Strauss, H., Farquhar, J., Ockert, C., Eickmann, B. and Jost, C.L., 2010, Sulfur cycling at the Mid-Atlantic Ridge: A multiple sulfur isotope approach: Chemical Geology, v. 269, p. 180–196.

Peters, M., Strauss, H., Petersen, S., Kummer, N.A., and Thomazo, C., 2011, Hydrothermalism in the Tyrrhenian Sea: Inorganic and microbial sulfur cycling as revealed by geochemical and multiple sulfur isotope data: Chemical Geology, v. 280, p. 217-231.

Plumlee, G.S., 1999, The environmental geochemistry of mineral deposits: Review in Economic Geology, v. 6A, p. 71-116

Proskurowski, G., Lilley, M.D., and Brown, T.A., 2004, Isotopic evidence of magmatism and seawater bicarbonate removal at the endeavour hydrothermal system, Earth and Planetary Science Letters, v. 225, p. 53–61.

Ran, B., and Simoneit B.R.T., 1994, Dissolved organic carbon in interstitial waters from sediments of Middle Valley, Proceedings of the Ocean Drilling Program, Scientific Results, v. 139, p. 441–446.

Rees, C.E., 1973, Steady-state model for sulfur isotope fractionation in bacterial reduction processes: Geochimica Et Cosmochimica Acta v. 37, p. 1141–1162.

Reeves, E.P., Seewald, J.S., Saccocia, P., Bach, W., Craddock, P.R., Shanks, III, W.C., Sylva, S.P., Walsh, E., Pichler, T., and Rosner, M., 2011, Geochemistry of hydrothermal fluids from the PACMANUS, Northeast Pual and Vienna Woods hydrothermal fields, Manus Basin, Papua New Guinea: Geochimica et Cosmochimica Acta, v. 75, p. 1088–1123.

Riddihough, R., 1984, Recent movements of the Juan-de Fuca plate system, Journal of Geophysical Research, v. 89, p. 6980–6994.

Robigou, V., Delaney, J.R., and Stakes, D.S., 1993, Large massive sulfide deposits in a newly discovered active hydrothermal system, the Highrise Field, Endeavour Segment, Juan-de-Fuca Ridge: Geophysical Research Letters, v. 20, p. 1887–1890.

Rouxel, O., Ono, S., Alt, J., Rumble, D., and Ludden, J., 2008, Sulfur isotope evidence for microbial sulfate reduction in altered oceanic basalts at ODP Site 801: Earth and Planetary Science Letters, v. 268, p. 110-123.

Ruby, E.G., Wirsen, C.O., and Jannasch, H.W., 1981, Chemolithotrophic Sulfur-Oxidizing Bacteria from the Galapagos Rift Hydrothermal Vents: Applied and Environmental Microbiology, v. 42, p., 317-324.

Sakai, H., Casadevall, T.J., and Moore J.G., 1982, Chemistry and isotope ratios of sulfur in basalts and volcanic gases at Kilauea Volcano, Hawaii: Geochimica et Cosmochimica Acta, v. 46, p. 729–738.

Sakai, H., Des Marais, D.J., Ueda, A., and Moore, J.G., 1984, Concentrations and isotope ratios of carbon, nitrogen and sulfur in ocean-floor basalts: Geochimica et Cosmochimica Acta, v. 48, p. 2433–2441.

Scholten, J.C., Lackschewitz, K.S., Marchig, V., Stoffers, P., and Mangini, A., 2000, 230Th/234U and 231Pa/235U Disequilibria in massive sulfides from the Bent Hill area (Legs 139 and 169): Proceedings of the Ocean Drilling Program, Scientific Results, v. 169, p. 1-15.

Schoonen, M.A.A., and Barnes, H.L., 1991a, Reactions forming pyrite and marcasite from solution: I. Nucleation of FeS2 below 100° C: Geochimica et Cosmochimica Acta, v. 55, p. 1495-1504.

Schoonen, M.A.A., and Barnes, H.L., 1991b, Reactions forming pyrite and marcasite from solution: II. Via FeS precursors below 100°C: Geochimica et Cosmochimica Acta, v. 55, p. 1505-1514.

Schoonen, M.A.A., and Barnes, H.L., 1991c, Mechanisms of pyrite and marcasite formation from solution: III. Hydrothermal processes: Geochimica et Cosmochimica Acta, v. 55, p. 3491-3504.

Shanks, III, W.C., Bohlke, J.K., and Seal, II, R.R., 1995, Stable Isotopes in Mid-Ocean Ridge Hydrothermal Systems: Interactions between Fluids, Minerals, and Organisms: Geophysical Monograph, v. 91, p. 194-221.

Sievert, S.M., Hügler, M., Taylor, C.D., Wirsen, C.O., 2008, Microbial Sulfur Metabolism: Springer, p. 238–258.

Seyfried, W.E., Seewald, J.S., Berndt, M.E., Ding, K., and Foustoukos, D.I., 2003, Chemistry of hydrothermal vent fluids from the Main Endeavour Field, northern Juan de Fuca Ridge: Geochemical controls in the aftermath of June 1999 seismic events: Journal of Geophysical Research, v. 108, p. 2429, doi:10.1029/2002JB001957.

Smith, W.H.F., and Sandwell, D.T., 1997, Global seafloor topography from satellite altimetry and ship depth soundings: Science, v. 277, p. 1957-1962.

Spiess, F.N., Macdonald, K.C., Atwater, T., Ballard, R., Carranza, A., Cordoba, D., Cox, C., Diaz, Garcia, V.M., Francheteau, J., Guerrero, J., Hawkins, J., Haymon, R., Hessler, R., Juteau, T., Kastner, M., Larson, R. Luyendyk, B., Macdougall, J.D., Miller, S., Normark, W., Orcutt, J., and Rangin, C., 1980, East Pacific Rise: Hot Springs and Geophysical Experiments: Science, v. 207, p. 1421-1432.

Stefansson, A., Keller, N.S., Gunnarsson Robin, J., and Ono, S., 2015, Multiple sulfur isotope systematics of Icelandic geothermal fluids and the source and reactions of sulfur in volcanic geothermal systems at divergent plate boundaries: Geochimica et Cosmochimica Acta, v. 165, p. 307-323.

Stuart, F.M., Duckworth, R., Turner, G., and Schofield, P.F., 1994, Helium and sulfur isotopes of sulfide minerals from Middle Valley, Northern Juan de Fuca Ridge: Proceedings of the Ocean Drilling Program, Scientific Results, v. 139, p. 387-392.

Thode, H.G., Monster, J., and Dunford, H.B., 1961, Sulphur isotope geochemistry: Geochimica et Cosmochimica Acta, v. 25, p. 159–174.

Tivey, M.K., and Delaney, J.R., 1986, Growth of large sulfide structures on the Endeavour Segment of the Juan de Fuca Ridge: Earth and Planetary Science Letters, v. 77, p. 303–317.

Tostevin, R., Turchyn, A.V., Farquhar, J., Johnston, D.T., Eldridge, D.L., Bishop, J.K.B., and McIlvin, M., 2014, Multiple sulfur isotope constraints on the modern sulfur cycle: Earth and Planetary Science Letters, v. 396, p. 14-21.

Tsurumi, M., and Tunnicliffe, V., 2003, Tubeworm-associated communities at hydrothermal vents on the Juan de Fuca Ridge, northeast Pacific: Deep Sea Research Part I: Oceanographic Research Papers, v. 50, p. 611-629.

Urey, H.C., 1947, The thermodynamic properties of isotopic substances: Journal of the Chemical Society, p. 562-581.

Ushikubo, T., Williford, K.H., Farquhar, J., Johnston, D.T., Van Kranendonk, M.J., and Valley, J.W., 2014, Development of in situ sulfur four-isotope analysis with multiple Faraday cup detectors by SIMS and application to pyrite grains in a Paleoproterozoic glaciogenic sandstone: Chemical Geology, v. 383, p. 86-99.

Van Ark, E.M., Detrick, R.S., Canales, J.P., Carbotte, S.M., Harding, A.J., Kent, G.M., Nedimovic, M.R., Wilcock, W.S.D., Diebold, J.B., and Babcock, J.M., 2007, Seismic structure of the Endeavour Segment, Juan de Fuca Ridge: Correlations with seismicity and hydrothermal activity, Journal of Geophysical Research, v. 112, doi:10.1029/2005JB004210.

Vine, F.J., and Wilson, J.T., 1965, Magnetic anomalies over a young oceanic ridge off Vancouver Island, Science: v.150, p.485–489.

Volpe, A.M., and Goldstein S.J., 1993, Ra-226 Th-230 disequilibrium in axial and off-axis mid-ocean ridge basalts, Geochimica et Cosmochimica Acta, v. 57, p. 1233–1241.

Willoughby, E.C., and Hyndman, R.D., 2005, Earthquake rate, slip rate, and the effective seismic thickness for oceanic transform faults of the Juan de Fuca plate system: Geophysical Journal International, v. 160, p. 855-868.

Wing, B.A., and Farquhar, J., 2015, Sulfur isotope homogeneity of lunar mare basalts: Geochimica et Cosmochimica Acta, v. 170, p. 266-280.

Wu, N., Farquhar, J., Dottin, III, J.W., and Magalhaes, N., 2018, Sulfur isotope signatures of eucrites and diogenites: Geochimica et Cosmochimica Acta, v. 233, p. 1-13.

You, C.F., Butterfield, D.A., Spivack, A.J., Gieskes, J.M., Gamo, T., and Campbell, A.J., 1994, Boron and halide systematics in submarine hydrothermal systems—Effects of phase separation and sedimentary contributions: Earth and Planetary Science Letters, v. 123, p. 227–238.

Young, E.D., Galy, A., and Nagahara, H., 2002, Kinetic and equilibrium mass-dependent isotope fractionation laws in nature and their geochemical and cosmochemical significance: Geochimica et Cosmochimica Acta, v. 66, p. 1095–1104.

Zierenberg, R.A., Koski, R.A., Morton, J.L., Bouse, R.M., and Shanks, III, W.C., 1993, Genesis of Massive Sulfide Deposits on a Sediment-Covered Spreading Center, Escanaba Trough, Southern Gorda Ridge: Economic Geology, v. 88, p. 2069-2098.

Zierenberg, R.A., 1994, Data report: Sulfur content of sediment and sulfur isotope values of sulfide and sulfate minerals from Middle Valley, Leg 139: Proceedings of the Ocean Drilling Program, Scientific Results, v. 139, p. 739-748.

Zierenberg, R.A., Fouquet, Y., Miller, J., and Shipboard Scientific Party, 1998, The deep structure of a seafloor hydrothermal deposit: Nature, v. 392, p. 485–488.

# Appendix A. Reference Data

Table A1: $H_2S$ sulfur isotope data from previous studies of modern marine hydrothermal systems, used in compilations figures (Data compiled from Peters et al., 2010[a]; Ono et al., 2007[b]; McDermott et al., 2015[c], McDermott et al., 2018[d]; McDermott, 2015[e]).

| Location | Vent field | Sample | $\delta^{34}S$ (‰) | $\Delta^{33}S$ (‰) (exponential) |
|---|---|---|---|---|
| SMAR[a] | Turtle Pits | 12 ROV-8 bottle 9 | 6.6 | 0.016 |
| SMAR[a] | Red Lion | 7 ROV-4 | 4.6 | 0.007 |
| SMAR[a] | Wideawake | 3 ROV-3 | 7 | 0.001 |
| SMAR[a] | Red Lion | 7 ROV-13 | 4.9 | 0.003 |
| SMAR[a] | Turtle Pits | 12 ROV-8 bottle 5 | 7.1 | 0.002 |
| EPR[b] | 9-10˚N | 2736-12 | 4.435 | 0.0294 |
| EPR[b] | 9-10˚N | 2748-14 | 4.674 | 0.0106 |
| EPR[b] | 9-10˚N | 2752-11 | 5.849 | 0.0230 |
| EPR[b] | 9-10˚N | 2756-14 | 4.825 | 0.0480 |
| Manus Basin[c] | Su Su Knolls | J2-224-IGT1 | -2.746 | 0.0111 |
| Manus Basin[c] | Su Su Knolls | J2-227-IGT1 | -5.016 | 0.0144 |
| Manus Basin[c] | Su Su Knolls | J2-227-IGT2 | -4.459 | 0.0039 |
| Manus Basin[c] | Su Su Knolls | J2-223-IGT7 | -4.887 | -0.0322 |
| Manus Basin[c] | PACMANUS | J2-222-IGT1 | 3.851 | -0.0044 |
| Manus Basin[c] | PACMANUS | J2-214-lGT8 | 0.838 | -0.0005 |
| Manus Basin[c] | PACMANUS | J2-213-lGT3 | 5.411 | 0.0090 |
| Manus Basin[c] | PACMANUS | J2-213-IGT7 | 1.392 | -0.0026 |
| Manus Basin[c] | PACMANUS | J2-208-IGT8 | 2.991 | -0.0342 |
| Manus Basin[c] | PACMANUS | J2-209-lGT6 | 0.545 | 0.0024 |
| Lau Basin[c] | Tui Malila (vent) | J2-442-IGT4 | 2.414 | -0.0155 |
| Lau Basin[c] | Mariner (vent) | J2-437-IGT5(rep1) | 6.108 | 0.0150 |
| Lau Basin[c] | Mariner (vent) | J2-437-IGT5(rep2) | 5.938 | 0.0183 |
| Lau Basin[c] | Mariner (vent) | J2-437-IGT6 | 5.944 | -0.0178 |
| Lau Basin[c] | ABE North (vent) | J2-449-IGT6 | 4.417 | -0.0013 |
| SEPR[c] | Wally (vent) | 3296-12C | 5.538 | -0.0063 |
| SEPR[c] | Simon (vent) | 3288-1C | 5.042 | -0.0095 |
| SEPR | Hobbes (vent) | 3299-9C | 5.707 | -0.0080 |
| Guaymas Basin[c] | Busted Mushroom (vent) | IGT-T525-4-H2S1 | -0.419 | -0.0222 |
| Guaymas Basin[c] | Rebecca's Roost (vent) | 4462-IGT1-H2S1 | -0.574 | -0.0073 |
| Guaymas Basin[c] | Cathedral Hill (vent) | IGT-T526-4-H2S1 | 2.315 | -0.0136 |
| Guaymas Basin[c] | Theme Park (vent) | 4458-IGT1-H2S2(rep1) | 4.153 | -0.0066 |
| Guaymas Basin[c] | Theme Park (vent) | 4458-IGT1-H2S2(rep2) | 4.749 | -0.0129 |
| Mid-Cayman Rise[d] | Piccard | J2-613-IGT1 | 5.8 | -0.02581 |
| Mid-Cayman Rise[d] | Piccard | J2-619-IGT4 | 6.3 | 0.00094 |
| Mid-Cayman Rise[d] | Piccard | J2-618-IGT2 | 6.3 | -0.01506 |
| Mid-Cayman Rise[d] | Piccard | J2-618-IGT8 | 6.0 | -0.01352 |
| Mid-Cayman Rise[e] | Von Damm | J2-612-IGT2 | 10.6 | -0.00704 |
| Mid-Cayman Rise[e] | Von Damm | J2-616-IGT8 | 10.3 | -0.02782 |
| Mid-Cayman Rise[e] | Von Damm | J2-616-IGT1 | 11.2 | -0.01242 |
| Mid-Cayman Rise[e] | Von Damm | J2-617-IGT4 | 9.9 | 0.00618 |
| Mid-Cayman Rise[e] | Von Damm | J2-617-IGT2 | 11.2 | -0.03842 |
| Mid-Cayman Rise[e] | Von Damm | J2-621-IGT4 | 10.2 | 0.00693 |
| Mid-Cayman Rise[e] | Von Damm | J2-612-IGT8 | 11.2 | -0.00742 |
| Mid-Cayman Rise[e] | Von Damm | J2-621-IGT2 | 9.9 | 0.00318 |

Table A2: Sulfate sulfur isotope data from previous studies of modern marine hydrothermal systems, used in compilations figures (Data compiled from Eickmann et al., 2014[a]; Jaeschke et al., 2014[b]).

| Location | Vent field | Sample | $\delta^{34}S$ (‰) | $\Delta^{33}S$ (‰) (exponential) |
|---|---|---|---|---|
| Arctic Mid-Ocean Ridge[a] | Loki's Castle | GS09ROV7-1-1 | 23 | -0.035 |
| Arctic Mid-Ocean Ridge[a] | Loki's Castle | GS09ROV7-1-2 | 22.2 | -0.031 |
| Arctic Mid-Ocean Ridge[a] | Loki's Castle | GS09ROV7-1-3 | 23.6 | -0.046 |
| Arctic Mid-Ocean Ridge[a] | Loki's Castle | GS09ROV7-1-4 | 22.2 | -0.041 |
| Arctic Mid-Ocean Ridge[a] | Loki's Castle | GS09ROV7-1-5 | 30.8 | -0.103 |
| Arctic Mid-Ocean Ridge[a] | Loki's Castle | GS09ROV7-1-6 | 24.3 | -0.059 |
| Arctic Mid-Ocean Ridge[a] | Loki's Castle | GS09ROV7-1-7 | 30.8 | -0.095 |
| Arctic Mid-Ocean Ridge[a] | Loki's Castle | GS09ROV7-1-8 | 33.2 | -0.125 |
| Arctic Mid-Ocean Ridge[a] | Loki's Castle | GS09ROV7-1-9 | 33.9 | -0.133 |
| Arctic Mid-Ocean Ridge[a] | Loki's Castle | GS09ROV7-1-10 | 34.2 | -0.126 |
| Arctic Mid-Ocean Ridge[a] | Loki's Castle | GS09ROV7-1-11 | 36.1 | -0.159 |
| Arctic Mid-Ocean Ridge[a] | Loki's Castle | GS09ROV7-1-12 | 32.7 | -0.135 |
| Arctic Mid-Ocean Ridge[b] | Loki's Castle | GS10-ROV8-2b | 9.7 | -0.014 |
| Arctic Mid-Ocean Ridge[b] | Loki's Castle | GS10-ROV8-4b | 22.3 | 0.024 |
| Arctic Mid-Ocean Ridge[b] | Loki's Castle | GS10-ROV8-5b | 21.6 | 0.034 |
| Arctic Mid-Ocean Ridge[b] | Loki's Castle | GS10-ROV8-6b | 21.1 | 0.031 |
| Arctic Mid-Ocean Ridge[b] | Loki's Castle | GS10-ROV8-7b | 22.5 | 0.019 |
| Arctic Mid-Ocean Ridge[b] | Loki's Castle | GS10-ROV8-8b | 21 | 0.025 |
| Arctic Mid-Ocean Ridge[b] | Loki's Castle | GS10-ROV8-9b | 21.3 | 0.02 |
| Arctic Mid-Ocean Ridge[b] | Loki's Castle | GS10-ROV8-10a | 22.5 | 0.029 |
| Arctic Mid-Ocean Ridge[b] | Loki's Castle | GS10-ROV5BS-1 | 21.1 | 0.02 |
| Arctic Mid-Ocean Ridge[b] | Loki's Castle | GS10-ROV5BS-2 | 20.4 | 0.013 |

Table A3: Sedimentary sulfide isotope data from previous studies of modern marine hydrothermal systems, used in compilations figures (Data compiled from Peters et al., 2011[a]; Peters et al., 2010[b]; Eickmann et al., 2014[c]).

| Location | Vent field | Sample | $\delta^{34}S$ (‰) | $\Delta^{33}S$ (‰) (exponential) |
|---|---|---|---|---|
| Tyrrhenian Sea[a] | Palinuro Volcanic Complex | 872 GC - 50 | 1 | 0.031 |
| Tyrrhenian Sea[a] | Palinuro Volcanic Complex | 872 GC - 105 | 6.1 | 0.06 |
| Tyrrhenian Sea[a] | Palinuro Volcanic Complex | 872 GC - 130 | -0.6 | 0.032 |
| Tyrrhenian Sea[a] | Palinuro Volcanic Complex | 872 GC - 140 | 10.2 | 0.015 |
| Tyrrhenian Sea[a] | Palinuro Volcanic Complex | 872 GC - 170 | -18.5 | 0.134 |
| Tyrrhenian Sea[a] | Palinuro Volcanic Complex | 872 GC - 180 | -2.5 | 0.024 |
| Tyrrhenian Sea[a] | Palinuro Volcanic Complex | 872 GC - 220 | -17.1 | 0.081 |
| Tyrrhenian Sea[a] | Palinuro Volcanic Complex | 872 GC - 230 | -25.2 | 0.046 |
| Tyrrhenian Sea[a] | Palinuro Volcanic Complex | 872 GC - 250 | -29.8 | 0.071 |
| Tyrrhenian Sea[a] | Palinuro Volcanic Complex | 872 GC - 290 | -27.5 | 0.047 |
| MAR[b] | Logatchev | 946GC-2/60cm | -22.7 | 0.107 |
| MAR[b] | Logatchev | 946GC-2/85cm | -22.8 | 0.107 |
| MAR[b] | Logatchev | 946GC-1A/25cm | -24.5 | 0.116 |
| MAR[b] | Logatchev | 946GC-1B/25cm | -24.5 | 0.125 |
| MAR[b] | Logatchev | 946GC-1/55cm | -25.1 | 0.074 |
| MAR[b] | Logatchev | 953GC-2/15cm | 6.5 | 0.018 |
| MAR[b] | Logatchev | 953GC-2/55cm | 3 | 0.012 |
| MAR[b] | Logatchev | 953GC-1/35cm | -12.5 | 0.114 |
| MAR[b] | Logatchev | 953GC-1/55cm | -7 | 0.118 |
| MAR[b] | Logatchev | 963GC-1/14–16cm | 5.5 | 0.002 |
| MAR[b] | Logatchev | 963GC-1/27–30cm | 5.5 | 0.001 |
| Arctic Mid-Ocean Ridge[c] | Loki's Castle | GS10ROV4 | -16.4 | 0.115 |

Table A4: Native sulfur isotope data from previous studies of modern marine hydrothermal systems, used in compilations figures (Data compiled from Peters et al., 2011[a]; McDermott et al., 2015[b]).

| Location | Vent field | Sample | $\delta^{34}S$ (‰) | $\Delta^{33}S$ (‰) (exponential) |
|---|---|---|---|---|
| Tyrrhenian Sea[a] | Palinuro Volcanic Complex | 851RD | -4.6 | 0.035 |
| Tyrrhenian Sea[a] | Palinuro Volcanic Complex | 865RD | -9.3 | 0.067 |
| Tyrrhenian Sea[a] | Palinuro Volcanic Complex | 865RD | -6.2 | 0.056 |
| Tyrrhenian Sea[a] | Palinuro Volcanic Complex | 865RD | -2.1 | 0.044 |
| Tyrrhenian Sea[a] | Palinuro Volcanic Complex | 932RD | -9 | 0.069 |
| Tyrrhenian Sea[a] | Palinuro Volcanic Complex | 932RD | -15.7 | 0.109 |
| Tyrrhenian Sea[a] | Palinuro Volcanic Complex | 932RD | -6 | 0.059 |
| Tyrrhenian Sea[a] | Palinuro Volcanic Complex | 932RD | -5.1 | 0.077 |
| Manus Basin[b] | DESMOS | J2-220-IGT2 | -5.197 | -0.0092 |
| Manus Basin[b] | DESMOS | J2-220-M4(rep1) | -4.776 | -0.0115 |
| Manus Basin[b] | DESMOS | J2-220-M4(rep2) | -7.686 | -0.0013 |
| Manus Basin[b] | DESMOS | J2-220-11-R1 | -7.64 | 0.0099 |
| Manus Basin[b] | DESMOS | J2-220-5-R2 | -8.19 | -0.0117 |
| Manus Basin[b] | Su Su Knolls | J2-221-IGT5 | -3.568 | 0.0091 |
| Manus Basin[b] | Su Su Knolls | J2-221-IGT6 | -1.476 | -0.0016 |
| Manus Basin[b] | Su Su Knolls | J2-221-M2 | -1.395 | 0.0027 |
| Manus Basin[b] | Su Su Knolls | J2-221-13-R1A | -3.700 | 0.0222 |
| Manus Basin[b] | Su Su Knolls | J2-221-13-R1B | -2.480 | 0.0000 |

Table A5: Pyrite sulfur isotope data from previous studies of modern marine hydrothermal systems, used in compilations figures (Data compiled from Eickmann et al., 2014[a]; Ono et al., 2007[b]; Peters et al., 2010[c]).

| Location | Vent field | Sample | $\delta^{34}S$ (‰) | $\Delta^{33}S$ (‰) (exponential) |
|---|---|---|---|---|
| Arctic Mid-Ocean Ridge[a] | Loki's Castle | GS09ROV7-1 | 9.9 | 0.016 |
| EPR[b] | 13˚N | 3938 | 0.525 | 0.031 |
| EPR[b] | 13˚N | 3938 | 0.391 | 0.030 |
| EPR[b] | 13˚N | 3938 | 0.925 | 0.026 |
| EPR[b] | 13˚N | 3938 | 1.002 | 0.018 |
| SMAR[c] | Nibelungen | 62 ROV-2 (CRS) | 4 | 0.05 |
| SMAR[c] | Nibelungen | 62 ROV-6 (CRS) | 5.9 | 0.035 |

Table A6: Sphalerite sulfur isotope data from previous studies of modern marine hydrothermal systems, used in compilations figures (Data compiled from Peters et al., 2010[a]; Ono et al., 2007[b]).

| Location | Vent field | Sample | $\delta^{34}S$ (‰) | $\Delta^{33}S$ (‰) (exponential) |
|---|---|---|---|---|
| SMAR[a] | Nibelungen | 62 ROV-2 (AVS) | 5.5 | 0.033 |
| SMAR[a] | Red Lion | 7 ROV-7 (AVS) | 2.9 | 0.008 |
| EPR[b] | 13˚N | 3938 | 2.18 | 0.002 |
| EPR[b] | 13˚N | 3938 | 2.632 | -0.002 |
| EPR[b] | 13˚N | 3938 | 2.046 | 0.015 |
| EPR[b] | 21˚S | 3290-7-1b | 5.307 | 0.012 |
| EPR[b] | 21˚S | 3290-7-1b | 4.863 | 0.012 |

Table A7: Marcasite sulfur isotope data from a previous study of modern marine hydrothermal systems, used in compilations figures (Ono et al., 2007).

| Location | Vent field | Sample | $\delta^{34}S$ (‰) | $\Delta^{33}S$ (‰) (exponential) |
|---|---|---|---|---|
| MAR | Lucky Strike | FL24-01 | -0.448 | 0.028 |
| MAR | Lucky Strike | FL24-02 | 0.46 | 0.033 |
| MAR | Lucky Strike | FL24-02 | -0.875 | 0.031 |

Table A8: Seawater isotope data from previous studies of modern marine hydrothermal systems, used in compilations figures (Data compiled from Eickmann et al., 2014[a]; Jaeschke et al., 2014[b]; Ono et al., 2012[c]; Tostevin et al., 2014[d]; Johnston et al., 2014[e]*).

| **Location** | **Depth** | **Sample** | **$\delta^{34}S$ (‰)** | **$\Delta^{33}S$ (‰) (exponential)** |
|---|---|---|---|---|
| Arctic Mid-Ocean Ridge[a,b] | Ambient deep water | GS09CTD7-2 | 21.3 | 0.02 |
| Arctic Mid-Ocean Ridge[a,b] | Ambient deep water | GS09CTD84 | 21.2 | 0.04 |
| Hawaii[c] | 1250 mbsl | KOK | 21.4 | 0.052 |
| Hawaii[c] | 2500 mbsl | KOK | 21.43 | 0.044 |
| Hawaii[c] | 3000 mbsl | KOK | 21.35 | 0.053 |
| Hawaii[c] | 12 mbsl | KOK | 21.26 | 0.054 |
| Bermuda[c] | Surface | EN408 | 21.31 | 0.049 |
| Bermuda[c] | 2000 mbsl | EN408 | 21.29 | 0.053 |
| Western Pacific Ocean[d] | n.d. | 1 | 21.81 | 0.046 |
| Western Pacific Ocean[d] | n.d. | 2 | 20.17 | 0.052 |
| Western Pacific Ocean[d] | n.d. | 3 | 21.29 | 0.045 |
| Western Pacific Ocean[d] | n.d. | 4 | 21.38 | 0.052 |
| Western Pacific Ocean[d] | n.d. | 5 | 21.26 | 0.045 |
| Western Pacific Ocean[d] | n.d. | 6 | 21.21 | 0.051 |
| Western Pacific Ocean[d] | n.d. | 7 | 21.53 | 0.058 |
| Western Pacific Ocean[d] | n.d. | 8 | 21.04 | 0.06 |
| Western Pacific Ocean[d] | n.d. | 9 | 21.22 | 0.057 |
| Western Pacific Ocean[d] | n.d. | 10 | 21.11 | 0.047 |
| Western Pacific Ocean[d] | n.d. | 11 | 21.62 | 0.053 |
| Western Pacific Ocean[d] | n.d. | 12 | 21.02 | 0.054 |
| Western Pacific Ocean[d] | n.d. | 13 | 21.58 | 0.064 |
| Western Pacific Ocean[d] | n.d. | 14 | 22.05 | 0.053 |
| Western Pacific Ocean[d] | n.d. | 15 | 21.12 | 0.033 |
| Western Pacific Ocean[d] | n.d. | 16 | 21.45 | 0.044 |
| Western Pacific Ocean[d] | n.d. | 17 | 21.73 | 0.055 |
| Western Pacific Ocean[d] | n.d. | 18 | 22.1 | 0.044 |
| Western Pacific Ocean[d] | n.d. | 19 | 20.46 | 0.045 |
| Western Pacific Ocean[d] | n.d. | 20 | 21.08 | 0.055 |
| Western Pacific Ocean[d] | n.d. | 21 | 20.42 | 0.061 |
| Western Pacific Ocean[d] | n.d. | 22 | 21.37 | 0.05 |
| Western Pacific Ocean[d] | n.d. | 23 | 21.2 | 0.054 |
| Western Pacific Ocean[d] | n.d. | 24 | 21.06 | 0.05 |
| Western Pacific Ocean[d] | n.d. | 25 | 21 | 0.054 |
| Western Pacific Ocean[d] | n.d. | 26 | 21.1 | 0.039 |
| Western Pacific Ocean[d] | n.d. | 27 | 21.39 | 0.052 |
| Western Pacific Ocean[d] | n.d. | 28 | 21.06 | 0.036 |
| N/A[e] | N/A | average* | 21.15 | 0.048 |

Table A9: Mixed/massive sulfide sulfur isotope data from previous studies of modern marine hydrothermal systems, used in compilations figures (Data compiled from Peters et al., 2011[a]; Peters et al., 2010[b]; Ono et al., 2007[c]).

| Location | Depth | Sample | $\delta^{34}S$ (‰) | $\Delta^{33}S$ (‰) (exponential) |
|---|---|---|---|---|
| Tyrrhenian Sea[a] | Palinuro Volcanic Complex | 851RD | -3.1 | 0.012 |
| Tyrrhenian Sea[a] | Palinuro Volcanic Complex | 851RD | -4.4 | 0.015 |
| Tyrrhenian Sea[a] | Palinuro Volcanic Complex | 865RD | -21.2 | 0.011 |
| Tyrrhenian Sea[a] | Palinuro Volcanic Complex | 865RD | -26 | 0.042 |
| Tyrrhenian Sea[a] | Palinuro Volcanic Complex | 865RD | -21.5 | 0.033 |
| Tyrrhenian Sea[a] | Palinuro Volcanic Complex | 865RD | -17.1 | 0.018 |
| Tyrrhenian Sea[a] | Palinuro Volcanic Complex | 865RD | -4.2 | -0.005 |
| Tyrrhenian Sea[a] | Palinuro Volcanic Complex | 865RD | -3.1 | -0.012 |
| Tyrrhenian Sea[a] | Palinuro Volcanic Complex | 932RD | -17.1 | -0.001 |
| Tyrrhenian Sea[a] | Palinuro Volcanic Complex | 932RD | -19.6 | 0.025 |
| SMAR[b] | Comfortless Cove | 20 ROV-1A (CRS) | 6.3 | 0.014 |
| SMAR[b] | Comfortless Cove | 20 ROV-2 (total) | 6.6 | 0.002 |
| SMAR[b] | Comfortless Cove | 20 ROV-2 (CRS) | 6.5 | 0.002 |
| SMAR[b] | Comfortless Cove | 20 ROV-3a (CRS) | 4.4 | 0.024 |
| EPR[c] | 9-10˚N | 2748-6-2 | 3.471 | 0.0029 |
| EPR[c] | 9-10˚N | 2736-3-4 | 2.634 | 0.0004 |
| EPR[c] | 9-10˚N | 2752-4-7 | 3.288 | 0.0060 |
| EPR[c] | 9-10˚N | 2756-4-2 | 1.341 | 0.0226 |

Table A10: Chalcopyrite sulfur isotope data from previous studies of modern marine hydrothermal systems, used in compilations figures (McDermott et al., 2015[a]; Ono et al., 2007[b]; Peters et al., 2010[c]).

| Location | Depth | Sample | $\delta^{34}S$ (‰) | $\Delta^{33}S$ (‰) (exponential) |
|---|---|---|---|---|
| Manus Basin[a] | Su Su Knolls | J2-223-1-RIA(1) | -4.431 | 0.0064 |
| Manus Basin[a] | Su Su Knolls | 2-223-1-R1A(2) | -4.131 | 0.0056 |
| Manus Basin[a] | PACMANUS | J2-209-1-R1(1) | -0.740 | -0.0018 |
| Manus Basin[a] | PACMANUS | J2-209-1-R1(2)(rep1) | -0.368 | 0.0125 |
| Manus Basin[a] | PACMANUS | J2-209-1-R1(2)(rep2) | -0.792 | 0.0170 |
| Manus Basin[a] | PACMANUS | J2-213-6-R1 | 5.640 | 0.0114 |
| Manus Basin[a] | PACMANUS | J2-214-3-R1A(rep1) | 0.498 | -0.0014 |
| Manus Basin[a] | PACMANUS | J2-214-3-R1A(rep2) | 0.431 | 0.0001 |
| Manus Basin[a] | PACMANUS | J2-222-4-R1-SO | 3.61 | -0.0065 |
| Manus Basin[a] | PACMANUS | J2-222-4-R1-SP | 3.896 | -0.0225 |
| Manus Basin[a] | PACMANUS | J2-213-3-R1A | 2.557 | 0.0050 |
| Manus Basin[a] | PACMANUS | J2-208-1-R1 | 2.818 | -0.0073 |
| Manus Basin[a] | Su Su Knolls | J2-227-10-R1-TS | -5.477 | -0.0046 |
| Manus Basin[a] | Su Su Knolls | J2-224-12-R1 | -2.925 | 0.0124 |
| Lau Basin[a] | Mariner (vent) | J2-437-3-R3 | 5.299 | 0.0115 |
| Lau Basin[a] | Tui Malila (vent) | J2-442-4-R2(1)(rep1) | 3.516 | -0.0062 |
| Lau Basin[a] | Tui Malila (vent) | J2-442-4-R2(1)(rep2) | 3.517 | -0.0107 |
| Lau Basin[a] | Tui Malila (vent) | J2-442-4-R2(2) | 3.18 | -0.0024 |
| Lau Basin[a] | ABE North (vent) | J2-449-6-R1(1) | 3.861 | -0.0036 |
| Lau Basin[a] | ABE North (vent) | J2-449-6-R1(2) | 4.198 | -0.0168 |
| Lau Basin[a] | ABE North (vent) | J2-449-6-R1(3) | 4.08 | -0.0091 |
| SEPR[a] | Simon (vent) | 3288-5-1a | 3.709 | -0.0034 |
| SEPR[a] | Wally (vent) | 3296-4 | 4.644 | -0.0130 |
| SEPR[a] | Hobbes (vent) | 3299-6-1e | 4.697 | -0.0122 |
| Guaymas Basin[a] | Busted Mushroom (vent) | T591-TA4-28a | -1.350 | -0.0035 |
| EPR[b] | 21˚S | 3290-7-1b | 4.543 | 0.005 |
| EPR[b] | 21˚S | 3290-7-1b | 4.558 | 0.008 |
| MAR[b] | Lucky Strike | FL24-01 | 1.72 | 0.023 |
| MAR[b] | Lucky Strike | FL29-02 | 3.584 | 0.008 |
| SMAR[c] | Red Lion | 7 ROV-7 (CRS) | 2.5 | 0.017 |
| SMAR[c] | Turtle Pits | 12 ROV-1 (total) | 5.4 | 0.015 |

Table A11: Basalt sulfur isotope data from previous studies of modern marine hydrothermal systems, used in compilations figures (Data from Peters et al., 2010[a]; Ono et al., 2012[b]). This list is not comprehensive.

| Location | Depth | Sample | $\delta^{34}S$ (‰) | $\Delta^{33}S$ (‰) (exponential) |
|---|---|---|---|---|
| SMAR[a] | Comfortless Cove | 20 ROV-3B (CRS) | -1.7 | -0.008 |
| SMARa | Wideawake | 12 ROV-3B (CRS) | -1.6 | -0.008 |
| EPR[b] | 9˚N | ALV4055-B6 | -0.06 | 0.0110 |
| EPR[b] | 9˚N | ALV4055-B6 | -0.13 | -0.0020 |
| EPR[b] | 9˚N | ALV4055-B6 | -0.4 | -0.0100 |
| EPR[b] | 9˚N | ALV4055-B6 | -0.07 | 0.0050 |
| MAR[a] | Logatchev | 954 RD-2 12–15cm | -3 | 0.029 |
| MAR[a] | Logatchev | 954 RD-4 0–10cm | 0.3 | 0.023 |
| MAR[a] | Logatchev | 954 RD-4 38–43cm | -2.7 | 0.063 |
| MAR[a] | Logatchev | 962 RD-8 20–25cm | 3 | 0.01 |
| MAR[a] | Logatchev | 962 RD-11 55–60cm | 0.7 | 0.013 |
| JdFR[b] | N/A | 1301B1-1 | -5.1 | 0.0050 |
| JdFR[b] | N/A | 1301B2-2 | -1.8 | 0.0040 |
| JdFR[b] | N/A | 1301B4R2-122B | -0.1 | -0.0130 |
| JdFR[b] | N/A | 1301B4R2-122G | -0.1 | -0.0130 |
| JdFR[b] | N/A | 1301B4-2 | 1 | -0.0040 |
| JdFR[b] | N/A | 1301B5-2 | 0.2 | -0.0170 |
| JdFR[b] | N/A | 1301B5-2 | -2.1 | 0.0080 |
| JdFR[b] | N/A | 1301B6-2G | -2.7 | -0.0160 |
| JdFR[b] | N/A | 1301B12R-1-28G | -0.8 | 0.0110 |
| JdFR[b] | N/A | 1301B14R1-65P | -1.7 | 0.0000 |
| JdFR[b] | N/A | 1301B14R1-65P | -4.1 | 0.0010 |
| JdFR[b] | N/A | 1301B14R1-65B | -10 | 0.0099 |
| JdFR[b] | N/A | 1301B14R1-65G | -1 | -0.0080 |
| JdFR[b] | N/A | 1301B14-1G | -5.7 | -0.0419 |
| JdFR[b] | N/A | 1301B14-1B | -9.3 | -0.0527 |
| JdFR[b] | N/A | 1301B14-1B | -13.7 | -0.0566 |
| JdFR[b] | N/A | 1301B17-16G | -2.7 | -0.0050 |
| JdFR[b] | N/A | 1301B19R1-41G | -2.9 | -0.0150 |
| JdFR[b] | N/A | 1301B19R1-41G | -3.5 | -0.0050 |
| JdFR[b] | N/A | 1301B19R1-41B | -4.4 | -0.0140 |
| JdFR[b] | N/A | 1301B19R1-41B | -0.5 | -0.0140 |
| JdFR[b] | N/A | 1301B20-1 | -0.9 | -0.0130 |
| JdFR[b] | N/A | 1301B23R2-66P | -9.6 | -0.0040 |
| JdFR[b] | N/A | 1301B23R2-66G | -5.1 | -0.0090 |
| JdFR[b] | N/A | 1301B23R2-66G | -0.7 | -0.0050 |
| JdFR[b] | N/A | 1301B23R2-66B | -0.9 | -0.0090 |
| JdFR[b] | N/A | 1301B23-2B | 0 | 0.0020 |
| JdFR[b] | N/A | 1301B23-2G | 0 | -0.0030 |
| JdFR[b] | N/A | 1301B23-2G | -2.1 | -0.0130 |
| JdFR[b] | N/A | 1301B25R1-123P | -3.4 | -0.0170 |
| JdFR[b] | N/A | 1301B25R1-123G | -5.2 | -0.0140 |
| JdFR[b] | N/A | 1301B25R1-123B | -1.5 | -0.0010 |
| JdFR[b] | N/A | 1301B26-1G | -1.2 | 0.0020 |
| JdFR[b] | N/A | 1301B26-1G | -0.9 | -0.0050 |
| JdFR[b] | N/A | 1301B32R3-50G | -1.4 | 0.0050 |
| JdFR[b] | N/A | 1301B32R3-50G | -1.6 | 0.0080 |
| JdFR[b] | N/A | 1301B32R3-50B | -4.2 | 0.0080 |
| JdFR[b] | N/A | 1301B36R1-53G | 0.1 | -0.0030 |
| JdFR[b] | N/A | 1301B36R1-53B | -1.7 | 0.0020 |
| JdFR[b] | N/A | 1301B36R1-53G | -1.5 | 0.0040 |

# Appendix B. Sample Data

Table B1: Sulfide samples and corresponding silver sulfide yields from analyses at University of Maryland (May 2018). Sample purities ranged from 80-99%, however specific estimates were lost and irretrievable after a hardware issue and failed data backup.

| Mineral | Sample | $Ag_2S$ Full Yield (mg) |
|---|---|---|
| Py | D264-R2 | 7.17 |
| Sph | ALV4450-1538 | 0.638 |
| Py | D266-R6 | 3.931 |
| Po | D265-R3 | 2.594 |
| Py | D266-R8 | 1.726 |
| Py | R1941-RCK12 | 5.235 |
| Sph | ALV4451-1725 | 8.591 |
| Po | ALV4522-1748 | 2.229 |
| Po | R1942-RCK16 | 5.761 |
| Py | R1940-RCK4 | 8.248 |
| CuPy | ALV4438-1816 | 6.627 |
| Po | R1938-RCK22 | 1.973 |
| Py | R1938-RCK21 | 6.32 |
| Py | R1938-RCK16 | 5.147 |
| Po | R1942-RCK10 | 2.168 |
| CuPy | R1939-RCK14 | 4.61 |
| Po | ALV4449-1938 | 1.303 |
| Py | R1940-RCK7 | 1.04 |
| Po | D264-R2 | 2.275 |
| | (Redo)D264-R2 | 7.761 |
| Py | R1940-RCK6 | 0.849 |
| | (Redo)R1940-RCK6 | 3.98 |
| Po | R1942-RCK8 | 0.975 |
| | (Redo)R1942-RCK8 | 2.543 |
| Mrc | R1939-RCK13 | 5.731 |
| CuPy | ALV4522-1748 | 3.974 |
| Py | R1940-RCK8 | 2.45 |
| CuPy | D266-R6 | 4.234 |
| CuPy | R1941-RCK12 | 3.467 |
| Py | R1941-RCK13 | 1.144 |
| Po | (Redo)D265-R3 | 10.493 |

Table B2: Sulfate samples analysed at University of Maryland (May 2018).

| Sample | Location | Sub location | Cruise | Mineral |
|---|---|---|---|---|
| D264-R22 | Endeavour | West of MEF (Outside Valley) | MBARI - Western Flyer - 2011 | Barite |
| ALV4522-1748 | Axial | International District | At15-47 - Atlantis - 2009 | Anhy |
| ALV4451-1725 | Endeavour | Sasquatch | AT15-36 - Atlantis - 2008 | Anhy |
| ALV4450-1538 | Endeavour | Mothra | AT15-36 - Atlantis - 2008 | Anhy |
| ALV4450-1829 | Endeavour | Mothra | AT15-36 - Atlantis - 2008 | Barite |

Table B3: Sulfide and sulfate samples and corresponding silver sulfide yields from analyses at Harvard University (February – March 2019).

| **Sample Name** | **Location** | **Vent Field** | **Cruise** | **Mineral** | **Estimated mineral purity (%)** | **$Ag_2S$ Yield (%)** |
|---|---|---|---|---|---|---|
| ALV4438-1816 | Endeavour | MEF | AT15-36 - Atlantis - 2008 | CuPy | 98 | 21%* |
| ALV4450-1538 | Endeavour | Mothra | AT15-36 - Atlantis - 2008 | Anhy | 95 | 71% |
| ALV4450-1829 | Endeavour | Mothra | AT15-36 - Atlantis - 2008 | Barite | 90 | 76% |
| ALV4451-1725 | Endeavour | Sasquatch | AT15-36 - Atlantis - 2008 | Wz | 85 | 30%* |
| ALV4522-1725 | Axial | International District | At15-47 - Atlantis - 2009 | Py | 98 | 73% |
| ALV4522-1748 | Axial | International District | At15-47 - Atlantis - 2009 | CuPy | 95 | 92% |
| D264-R2 | Endeavour | Salty Dawg | MBARI - Western Flyer - 2011 | Py | 95 | 34%* |
| D265-R3 | Endeavour | Sasquatch | MBARI - Western Flyer - 2011 | MgPy | 99 | 83% |
| D266-R6 | Endeavour | Flank of Zephyr Mound | MBARI - Western Flyer - 2011 | CuPy | 90 | 92% |
| D266-R8 | Endeavour | North of Zephyr Mound | MBARI - Western Flyer - 2011 | Py | 100 | 83% |
| R1938-RCK-21 | Endeavour | Sasquatch | CCGS Tully - 2016 | Py | 99 | 23%* |
| R1938-RCK-22 | Endeavour | Sasquatch | CCGS Tully - 2016 | Po | 95 | 75% |
| R1939-RCK-13 | Endeavour | SE of MEF | CCGS Tully - 2016 | Mrc | 95 | 77% |
| R1940-RCK-4 | Endeavour | North of MEF | CCGS Tully - 2016 | Py | 90 | 94% |
| R1940-RCK-6 | Endeavour | North of MEF | CCGS Tully - 2016 | Py | 99 | 86% |
| R1940-RCK-7 | Endeavour | North of MEF | CCGS Tully - 2016 | Py | 100 | 31%* |
| R1941-RCK-12 | Endeavour | High Rise | CCGS Tully - 2016 | Py | 100 | 63% |
| R1941-RCK-13 | Endeavour | High Rise | CCGS Tully - 2016 | Py | 100 | 26%* |
| R1942-RCK-10 | Middle Valley | Bent Hill | CCGS Tully - 2016 | Py/po mix | 98 | 88% |
| R1942-RCK-16 | Middle Valley | Bent Hill | CCGS Tully - 2016 | Po | 100 | 88% |
| R1942-Rock 8 | Middle Valley | Bent Hill | CCGS Tully - 2016 | Po | 90 | 75% |

*analysed during first round of reductions, no anti-foaming agent used

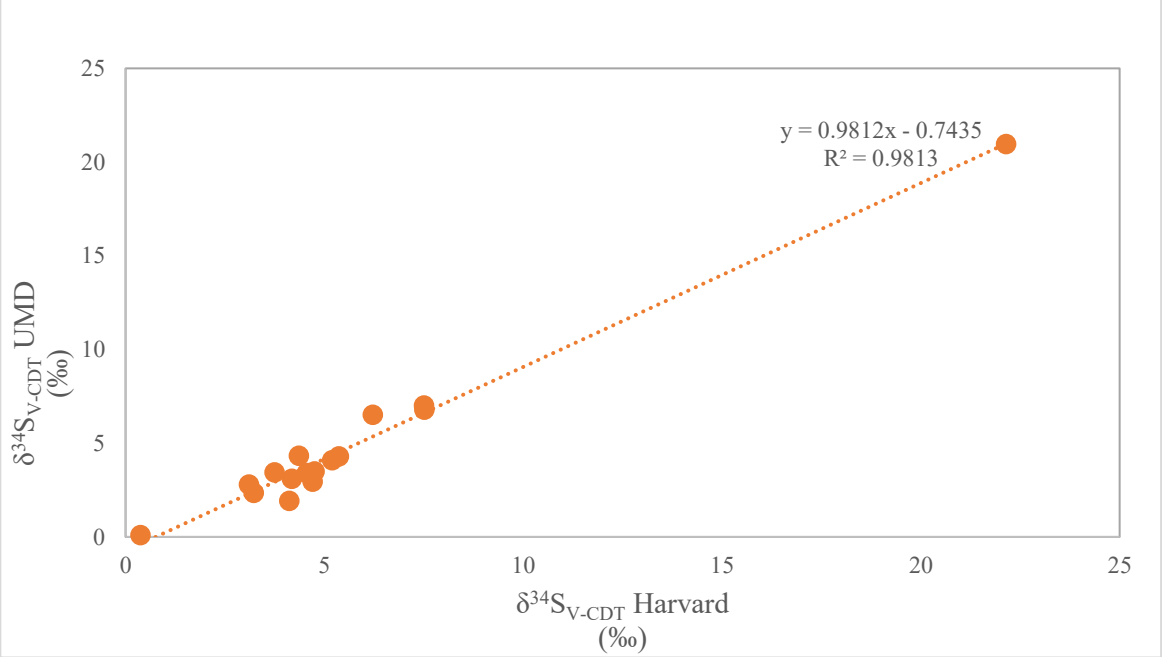


Figure B. 1 Biplot of renormalized $\delta^{34}S$ data from UMD against corresponding values from Harvard. 1σ error bars are the size of the symbols.

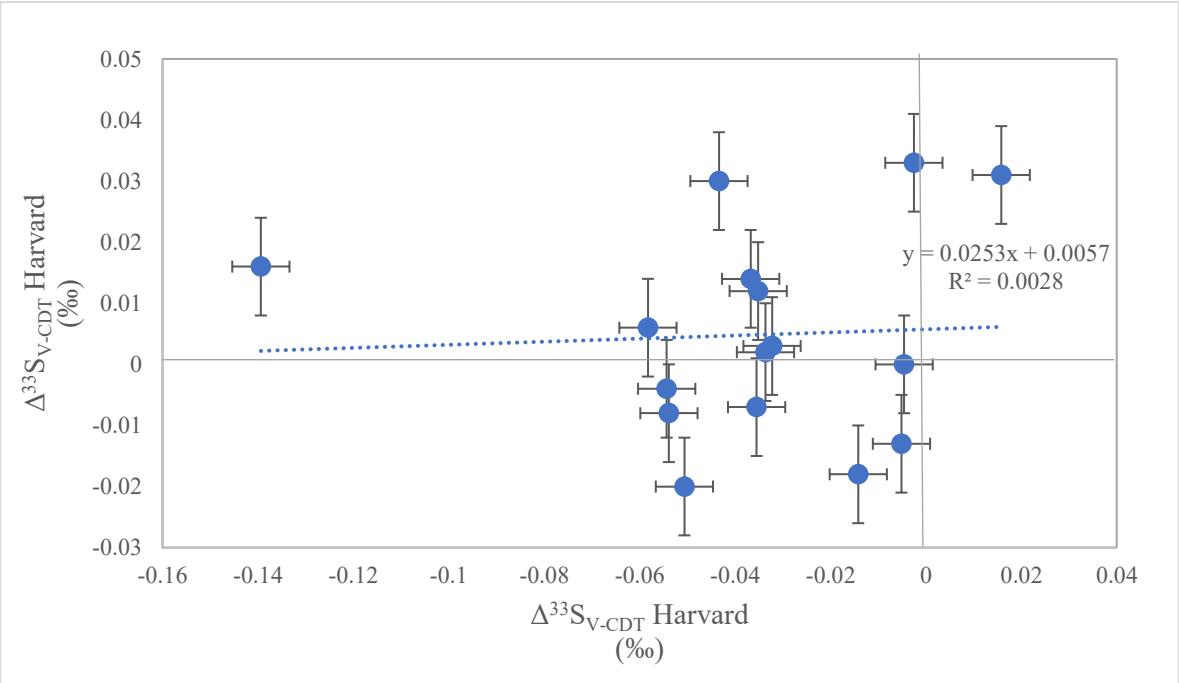


Figure B. 2 Biplot of renormalized $\Delta^{33}S$ data from UMD against corresponding values from Harvard. Error bars are 1σ.